Two-dimensional modelling of fracture in reinforced concrete structures applying the extended finite element method

zur Erlangung des akademischen Grades eines

DOKTOR-INGENIEURS /

von der KIT-Fakultät für
Bauingenieur-, Geo- und Umweltwissenschaften
des Karlsruher Instituts für Technologie (KIT)

genehmigte
DISSERTATION

von
Rodrigo Hernán Gutiérrez Aqueveque
aus Santiago, Chile

Tag der mündlichen Prüfung: 17. 01. 2020
Referent: Prof. Dr.-Ing. Lothar Stempniewski
Korreferent: Prof. Dr.-Ing. Wagner Fleming
Korreferent: Prof. Dr.-Ing. Stefan Löhnert

Abstract

Non-linear finite elements techniques have seen significant advancements regarding the modelling of the complex behaviour of reinforced concrete structures. Among them, the methods based on discrete approaches have received a great amount of attention in the last decades due to their capability to analyse for explicitly the cracking behaviour in concrete structures as accurately as possible. However, the need of conforming the mesh to the discontinuities geometry, and the corresponding computation effort, are presented as the major drawbacks of this approach. The advent of the eXtended Finite Element Method (X-FEM) in the late nineties has succeeded in overcoming these difficulties, making the remeshing procedures unnecessary. This method is able to model discontinuities within an element independent of the underlying spatial discretisation, by enriching the standard finite element approximation with discontinuous functions that represent the local behaviour of the solution. Since its appearance, X-FEM seems to be the best-suited method for the modelling of crack growth in concrete. However, despite the considerable potential of the method, there are no applications to the modelling of multiple crack growth in reinforced concrete structures. This study emerges in response to this need.

This work is concerned with the modelling of multiple crack growth in reinforced concrete structures under quasi-static conditions within the framework of the extended finite element method. Both cracks and reinforcement introduce discontinuities in the structure and, therefore, can be numerically modelled with X-FEM. Cracks are treated using a discontinuous (step) function and a non-singular near-tip function. These functions allow the crack to be located arbitrarily within a finite element. A HEAVISIDE function is introduced to model the reinforcement within an element without meshing it. The reinforcement includes not only reinforcing bars, but also externally bonded reinforcement and fibres. A cohesive crack model is used to represent the fracture process zone. Crack initiation and growth are evaluated by means of stress-based criteria. The concrete is described in compression by

an isotropic damage model. The transfer of bond forces along the concrete-reinforcement interface is accomplished by bond laws, which consider both bond-slip and dowel action. Representative tests reported in the literature on reinforced concrete structures are analysed. The numerical results are in very good agreement with the available data and, therefore, confirm the accuracy of the proposed approach. Moreover, a sensitivity analysis shows that the predicted responses are not affected by the finite element mesh.

The proposed numerical model proves to be useful, accurate and versatile when modelling reinforced concrete structures.

Zusammenfassung

Nichtlineare Finite-Elemente-Verfahren haben bei der Modellierung des komplexen Verhaltens von Stahlbetonstrukturen bedeutende Fortschritte erlebt. Unter anderem haben die auf diskreten Ansätzen basierenden Verfahren in den letzten Jahrzehnten aufgrund ihrer Fähigkeit, das Rissverhalten in Betonbauwerken explizit und so genau wie möglich zu analysieren, große Beachtung gefunden. Als wesentliche Nachteile dieses Ansatzes werden jedoch die Notwendigkeit der Anpassung des Netzes an die Diskontinuitätsgeometrie und der entsprechende Rechenaufwand dargestellt. Mit der Einführung der *extended finite element method* (X-FEM) in den späten neunziger Jahren ist es gelungen, diese Schwierigkeiten zu überwinden und damit die Netzabhängigkeit zu beseitigen. Dieses Verfahren ist in der Lage, Diskontinuitäten innerhalb eines Elements unabhängig von der zugrunde liegenden räumlichen Diskretisierung zu modellieren. Hierbei wird die Standard-Finite-Elemente-Approximation mit diskontinuierlichen Funktionen erweitert, die das lokale Verhalten der Lösung darstellen. Seit ihrer Entwicklung scheint X-FEM die am besten geeignete Methode zur Modellierung des Risswachstums im Beton zu sein. Trotz des erheblichen Potenzials der Methode gibt es keine Anwendungen bei der Modellierung des mehrfachen Risswachstums in Stahlbetonbauwerken. Hierdurch ergab sich die Notwendigkeit dieser Untersuchung.

Diese Arbeit beschäftigt sich mit der Modellierung des mehrfachen Risswachstums in Stahlbetonbauwerken unter quasi-statischen Bedingungen im Rahmen der *extended finite element method*. Sowohl Risse als auch Bewehrungen führen zu Diskontinuitäten in der Struktur und können daher mit X-FEM numerisch modelliert werden. Risse werden mit einer diskontinuierlichen Stufenfunktion und einer nicht-singulären Rissspitzenfunktion behandelt. Diese Funktionen ermöglichen, dass der Riss beliebig innerhalb eines finiten Elements abgebildet werden kann. Eine HEAVISIDE-Funktion wird eingeführt, um die Bewehrung innerhalb eines Elements zu modellieren, ohne das Finite Elemente Netz anzupassen. Die Bewehrung umfasst nicht nur Bewehrungsstäbe, sondern auch extern geklebte Bewehrungen und Fasern.

Zur Darstellung der Bruchprozesszone wird ein kohäsives Rissmodell verwendet. Rissentstehung und -wachstum werden mittels spannungsbasierter Kriterien bewertet. Der Beton wird unter Druck durch ein isotropes Schädigungsmodell beschrieben. Die Übertragung der Verbundkräfte erfolgt entlang der Kontaktfläche Beton-Bewehrung durch Verbundgesetze, die sowohl das Verbund-Schlupf-Verhalten als auch die Dübelwirkung berücksichtigen. Es werden repräsentative Versuche an Stahlbetonbauteilen analysiert. Die numerischen Ergebnisse stimmen sehr gut mit den verfügbaren Daten überein und bestätigen daher die Genauigkeit des vorgeschlagenen Ansatzes. Darüber hinaus zeigt eine Sensitivitätsanalyse, dass das vorhergesagte Verhalten durch das Finite-Elemente-Netz nicht beeinflusst wird.

Das vorgeschlagene numerische Modell erweist sich als nützlich, genau und vielseitig bei der Modellierung von Stahlbetonkonstruktionen.

Contents

List of Figures

List of Tables

1. Introduction

1.1. Motivation

The numerical modelling of reinforced concrete structures presents still today a major challenge for engineers across the globe due to their very complex non-linear behaviour both at strength limit states and service loads. For this reason, daily structural design is still generally based on determining internal forces and moments by means of an elastic model, in which the reinforced concrete structure is assumed to be uncracked, homogenous, isotropic and linearly elastic. For some design and analysis problems, however, these assumptions may not be sufficient and may lead to errors in the predicted response of the structure. Furthermore, they make it impossible to analyse cracked concrete structures to obtain reliable forecasts of security and durability. The development of more refined numerical methods, such as non-linear finite element techniques, has permitted to account for the materials non-linearities, which has allowed to generate more realistic numerical models to address the aforementioned problems.

The main obstacle to finite element analyses is the difficulty in characterising the material behaviour of the constituent parts, i.e. concrete, the reinforcing steel and the bond between them.

The mechanical behaviour of concrete is complicated and still remains the subject of intensive research activities. Concrete under tension behaves different than under compression. Compressive failure is mainly characterised by crushing while tensile failure, by cracking. These represent the main causes for the non-linearity of the material.

In this regard, one of the most challenging issues for engineers and researchers has been the modelling of concrete cracking. To this end, a large number of material models based on different theories have been developed over the last

decades. These have been incorporated into finite element approaches suitable for the representation of cracks. The proposed approaches range from discrete representations to various types of smeared crack concepts. The former is characterised by accounting for explicitly the displacement discontinuities introduced by the cracks into the numerical model. In the latter, the cracked material is treated as a continuum and the cracks are described in terms of strain-stress relationships.

Smeared crack approaches have been widely accepted as one of the most effective means to numerically simulate crack growth in concrete structures in order to predict global structural response. However, this approach does not permit an accurate description of the cracking behaviour and, due to the continuum assumption, it is not capable of predicting individual crack patterns and widths. On the other hand, discrete crack approaches make it possible to accurately analyse cracking in concrete structures and to obtain detailed information concerning cracking properties.

The aforementioned approaches have been also used to model reinforcing bars. In a discrete representation, each layer of reinforcement is modelled explicitly as separate elements connected to the concrete bulk through special elements known as interface elements, which allow for an explicit consideration of bond-slip, dowel action and other interaction mechanisms. In the smeared formulation, the influence of the bars is assumed to be uniformly distributed over a concrete element by introducing an average strain-stress relationship. Smeared representations characterise the interface behaviour implicitly by modifying the constitutive relations for concrete and/or the reinforcing steel.

The actual detailing arrangement of the reinforcement, as well as an adequate representation of the bond behaviour and dowel action, are necessary for realistic analyses of reinforced concrete structures. Unlike smeared approaches, the discrete representation is the only way of accounting for these considerations.

In conclusion, discrete methods are more suitable to capture the cracking failure, and the mechanical behaviour of the reinforcement and the interface. Drawbacks of these approaches are the great computation effort required for the discretisation of the structure in order to conform the mesh to the discontinuities geometry. These disadvantages are even greater when modelling crack propagation, where remeshing is required at each growth stage.

Over the last two decades, several approaches have been proposed to solve the aforementioned problems. Among them, the eXtended Finite Element Method (X-FEM). Within this method, the standard finite element approximation is locally enriched with functions that allow for a representation of discontinuities within an element without the need of redefining the underlying finite element mesh. The method enjoys all advantages of discrete models but without the dependency of the mesh, which was a characteristic attributed to smeared approaches, among others. Since its appearance, X-FEM seems to be the best-suited method for the modelling of crack growth in concrete.

Even though significant research has been conducted in this field, this involves usually the analysis of a single cohesive crack or a few non-interacting cracks. Few studies have addressed the issue of the multiple crack growth, being mostly limited to the analysis of brittle materials. Further, even fewer studies focus on the simulation of crack growth in reinforced concrete. Then, the application of X-FEM needs to be extended so it may handle multiple crack growth in reinforced concrete structures.

Furthermore, an appropriate choice of enrichment functions may allow the reinforcement to be also represented in a discrete form and independent of the finite element mesh. Thus, the potential of X-FEM can be fully exploited, allowing for an accurate analysis of RC structures.

These reasons motivate the current study, which focuses then on the application of X-FEM to the modelling of multiple cracks and reinforcement, in order to develop a proper numerical model for the analysis of the behaviour of reinforced concrete structures in an efficient and mesh independent way.

1.2. Aim and scope of the work

The aim of this thesis is to develop a two-dimensional finite element model for the modelling of fracture in reinforced concrete structures under quasi-static conditions that is easily implemented in a finite element program. Since the tensile failure of concrete is characterised by the formation and growth of cracks, the extended finite element method is used as a framework for the numerical model. The advantages of this method are numerous and were mentioned earlier in this chapter. Furthermore, this work extends the current

applications of X-FEM to the discrete modelling of reinforcing bars, including transverse reinforcement, as well as of externally bonded reinforcement and fibres. The main characteristics of the constituent materials behaviour are represented with sufficient accuracy by means of suitable material models. Towards this goal the following tasks were undertaken:

- Development of a general approach based on X-FEM for the modelling of multiple cohesive cracks. The cracks are represented explicitly by means of a near-tip enrichment and a discontinuous (step) enrichment. These enrichments are sufficient to allow the crack to be located arbitrarily within a finite element. Only coalesce (junction) of cracks is considered as interaction mechanism between cracks. The crack junction is treated using a step-junction enrichment. Then, considering these enrichments, the cracks growth simulation can be run from early cracking towards complete failure in a mesh independent way.
- Extension of the applications of X-FEM to the modelling of reinforcing bars, including transverse reinforcement, as well as of bonded reinforcement and fibres. These are described individually by means of a HEAVISIDE function that is discontinuous along the reinforcements, thus allowing them to be arbitrarily orientated and positioned within an element without meshing them. This approach treats the cracked concrete matrix as a background on which discrete reinforcements are superimposed.
- Application of suitable material models for the constituent parts. a) A cohesive crack model is used to represent the fracture process zone. Stress-based criteria are used to predict tensile failure. b) An isotropic damage model is used to describe the behaviour of concrete in compression. Damage models exhibiting softening behaviour and stiffness degradation often lead to convergence difficulties. Unfortunately, these difficulties could not be overcome in the development of the finite element program. Therefore, a parabola-line curve is assumed for the stress-strain relationship. The compressive stress is then assumed to remain constant once the compressive strength is exceeded and, consequently, no softening behaviour is considered. In this way, the convergence difficulties are avoided.

A common technique to overcome some of these convergence difficulties is the use of a viscoplastic regularization of the constitutive equations, which causes the consistent tangent stiffness of the softening material to become positive for sufficiently small time increments. Non-local formulations

c) The behaviour of the reinforcing steel can be modelled using an idealised one-dimensional model, since only its axial response is significant. In this regard, a one-dimensional elasto-plastic constitutive law with isotropic linear hardening is used to model the non-linear behaviour of the reinforcing steel. d) The transfer of forces along the concrete-reinforcement interface is accomplished by a constitutive law, which considers bond-slip failure and dowel action. For the bonded reinforcement and the fibres, suitable bond laws are also presented. Moreover, a penalty formulation is used to mediate the interaction between the longitudinal and transverse reinforcement once these come into contact, and to account for the horizontal legs of the transverse bars anchoring the vertical legs around the main bars. The continuous degradation of the materials due to cyclic loading is not considered in any material model.

- Description of the numerical aspect necessary for a proper implementation of the proposed model.

The discretisation of the approximate fields is performed at an element level in a matrix representation using the VOIGT notation. It should be emphasised that the finite element model is formulated so that any constitutive law could be employed.

The robustness and performance of the proposed numerical model is demonstrated in the work by means of representative examples. For this purpose, the proposed finite element model was integrated in the finite element program developed in MATLAB by Dr.-Ing. WAGNER FLEMING as part of his doctoral thesis [50]. The further development of the program allowed me to have an overview of the aspects regarding the computational implementation.

1.3. Outline of the Dissertation

A brief outline of the rest of the dissertation is summarised as follows. The state of the art is reviewed in Chapter 2. The governing equations regarding a cracked reinforced concrete body and the corresponding weak formulation are introduced in detail in Chapter 3. The governing equations are complemented by: a cohesive crack model for the modelling of cohesive crack growth, a damage model to account for the concrete behaviour under compression, and a bond model characterising the bond-slip behaviour and dowel action along the interface between the concrete bulk and its embedded reinforcement. Chapter 4 presents the extended finite element method for the spatial discretisation. Different enrichment schemes for the representation of cracks and reinforcements are discussed. The numerical implementation of the bond model is likewise described. Since non-linear material laws are used, the discrete equilibrium equation is linearised in order to solve it through an incremental iterative procedure. Furthermore, important aspects of the numerical implementation are included. The proposed formulation is validated against many test results reported in the literature in Chapter 5. Additionally, a sensitivity analysis is also performed. In Chapter 6 the findings in the preceding chapters are summarised, and final conclusions and outlook to future work are discussed.

2. State of the art

A brief review regarding the numerical modelling of reinforced concrete structures is presented, focusing on the developments and applications of discrete approaches and, especially, of the extended finite element method.

Concrete is a heterogeneous material that consists of fine and coarse aggregates bonded together with a cement paste. Due to the limited bonding strength and to the presence of various pre-existing micro-cracks and flaws, concrete is inherently weak in tension. The tensile failure of concrete is accompanied by a large and variable size inelastic damage zone, i.e. a region characterised by the formation and coalescence of micro-cracks and other defects, which eventually form a propagating macro-crack. This damage zone is known as the Fracture Process Zone (FPZ). Within this zone, the material gradually loses its capacity to transfer loads at increasing deformation, thus exhibiting a softening behaviour.

In principle, due to the presence of the fracture process zone, the applications of the linear elastic fracture mechanics to the modelling of concrete structures lead to inconsistent and unreliable results. This difficulty was first recognised by HILLERBORG et al. [57], who presented a pioneer work in which a fictitious crack model based on the cohesive crack concept [8, 40] was introduced to represent the FPZ. Thereafter, adapting to HILLERBORG et al., BAŽANT et al. [9] developed a crack band model in which the FPZ is modelled in a smeared manner [102]. Since then, the modelling of fracture in concrete has been generally based on these two approaches.

The former model is essentially a discrete approach, i.e. cracks are explicitly modelled by introducing a discontinuity in the continuum and, therefore, are treated as a well-defined geometric entity. This approach is physically intuitive, but requires tracking of each individual crack. A brief overview of discrete models will be discussed later in this section.

In a smeared crack approach, the influence of cracks is smeared over the continuum by modifying the constitutive relations. This can be imagined

as a set of infinitely many parallel cracks with an infinitesimal width continuously distributed (smeared) over the elements. This approach was used for the first time by RASHID [102], who treated fracture by modifying the element behaviour from isotropic to orthotropic, in which the element stiffness orthogonal to the crack was considered equal to zero when cracking occurred. Gradually, extensive research showed that this classical smeared-cracking concept leads to numerical difficulties such as strain localisation and mesh size dependency. To overcome this, BAŽANT et al. proposed the existence of prescribed bands with a certain constant width, which is treated as a material property and can also be identified with the fracture process zone, over which the strain softening is assumed to be uniformly smeared. The bands assure that the energy dissipation remains constant, thus avoiding spurious mesh sensitivity. The model is referred to by the authors as crack band model, and was proposed in general terms in [10] and in detail for gradual strain softening in [9]. The crack band approach has been the model most widely used in practice for analysing the distributed cracking and fracture of concrete and concrete-like materials. Some overview of this model can be found in [11, 32, 97].

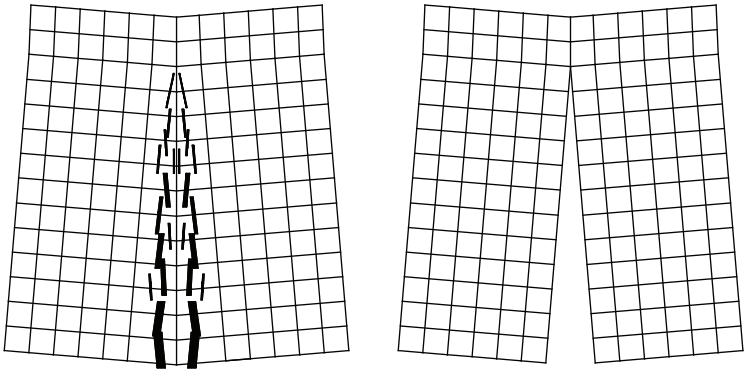

Figure 2.1.: Smeared (left) and discrete (right) approaches for crack modelling.

2.1. Cohesive crack model

The cohesive crack approach was first introduced by DUGDALE [40] while trying to analyse the plastic yielding in notched steel sheets. He proposed the existence of a cohesive fictional zone near the crack tip. Within this cohesive zone, a stress equal to the yield strength acts across the crack. BARENBLATT [8] introduced separately the cohesive zone concept in order to simulate cracking in brittle materials, but with the difference that the stress is assumed to vary with the deformation. In both models, the crack was divided into two parts, a stress-free crack (macro-crack) and the cohesive zone ahead of the macro-crack. Inspired by these pioneering works, HILLERBORG et al. applied the cohesive zone approach within a finite element framework to represent the fracture process zone in concrete-like materials. Furthermore, they additionally proposed that the cohesive zone may be assumed to develop anywhere, independently of the existence of a previous macro-crack.

According to HILLERBORG et al., a crack propagates, or initiates if no crack is present, when the maximal principal stress at the crack tip reaches the tensile strength. When the crack opens, the stress is not assumed to fall to zero at once, but to decrease gradually with increasing crack opening according to a softening function (traction-separation relationship). This cohesive zone is called by the authors as micro-cracked zone, i.e. the fracture process zone. The model is described only for mode *I* (the opening mode), but it may also be applied to modes *II* and *III*. Subsequently, this approach has been modified and used by many researchers over the years, resulting in a more general model known as cohesive crack model.

The cohesive crack model can be then summarised as follows: the fracture process zone is modelled as a discrete crack known as cohesive or fictitious crack. Along the cohesive crack, cohesive tractions can still be transferred across the crack surfaces. A cohesive constitutive law, relating the cohesive tractions with the relative displacements across the crack surfaces, describes the local behaviour inside the FPZ and its evolution up to complete failure. The macro-crack is formed as soon as a critical crack opening has been reached. Outside the FPZ, the bulk material behaves linear-elastic (or elastic-plastic), being described by means of a classical constitutive law. Crack initiation and growth criteria determine the conditions in which a crack will be initiated or propagated, as well as the orientation of the newly formed segments.

Due to its computational efficiency and versatility, this model has been used to analyse the fracture process in a wide range of others material such as polymers [63, 101], ductile materials [30, 71] and bi-material interfaces [64, 89], as well as the delamination in composites and debonding [26, 29, 33, 34, 118, 119]. This method has been also extended to consider fatigue crack growth [12, 72, 128].

Its application to the extended finite element method will be discussed later in this chapter.

2.2. Discrete models

Discrete models were introduced for the first time in a finite element analysis by NGO et al. [90] in order to analyse RC structures. Originally, cracks were modelled by means of the separation between element edges and, therefore, their propagation was limited to inter-element boundaries, implying a lack of physical fidelity of the possible crack path and a high computational cost. These hindrances were reduced, if not eliminated, with the development of automatic remeshing methods, as those introduced by INGRAFFEA et al. [60], to accommodate crack propagation. Nevertheless, remeshing procedures present a high numerical complexity and have the disadvantage that they are not that easily implemented in a finite element program.

An alternative approach to modelling discrete cracking, already mentioned in [108], is to use interface elements. Within this approach, the discontinuous behaviour at any interface is modelled using connecting elements (interface elements), which are placed between bulk elements and mediate the interaction between them. These elements can be divided into continuous interface elements (line, plane or shell type) and lumped interface elements. The former elements smooth the behaviour along an interpolated field, whereas the latter evaluate the tractions and displacements at isolated node-sets[1]. To allow for a variety of possible crack growth paths, interfacial elements equipped with a fracture-based constitutive law are inserted at the outset along potential fracture paths [92, 126]. Interface elements have been also used for the modelling of rock joints, aggregate interlock, bond between

[1] To a certain extent, they exert a similar behaviour as simple springs.

concrete and reinforcement, delamination in layered composite structures, among others.

The advent of meshless methods, such as the element-free GALERKIN method [15], made the remeshing procedures in the simulation of crack growth unnecessary. In these methods, the discretisation of the entire domain is based only on one set of nodes, independent of the finite element mesh. However, a large computational demand, associated with the generation of representative shape functions and with additional quadratures, is required. Moreover, they also present difficulties to satisfy the DIRICHLET boundary conditions.

2.3. Extended finite element method

In the late nineties, BELYTSCHKO et al. [14] presented a finite element method, based on the partition of unity concept studied in [81], for elastic crack growth with a minimal remeshing. In that work, in order to account for the presence of the crack, the finite element approximation is enriched with functions based on the asymptotic features of the displacement field. The enrichment is accomplished with the addition of extra degrees of freedom. This technique alleviates the need for conforming the mesh to the crack geometry. For long or severely curved cracks, however, the mapping technique proposed by BELYTSCHKO et al. is not readily applicable and, therefore, remeshing away from the crack tip is still necessary. In [85], the additional incorporation of a discontinuous jump enrichment away from the tip allows the crack to be completely independent of the underlying mesh, thus remeshing is not necessary in crack growth problems. Thereafter, DOLBOW et al. used the new methodology to solve problems within the framework of the two-dimensional linear elastic mechanics [38] and the MINDLIN-REISSNER plate theory [39], and problems involving crack growth with frictional contact [37]. In his doctoral thesis [36], DOLBOW described this new methodology and its applications, and named it: the eXtended Finite Element Method (X-FEM). The representation of a crack through X-FEM is schematically illustrated in Figure 2.2. Since then, the applications and developments of X-FEM have experienced significant advancements in studying the behaviour of a wide range of engineering and physical problems.

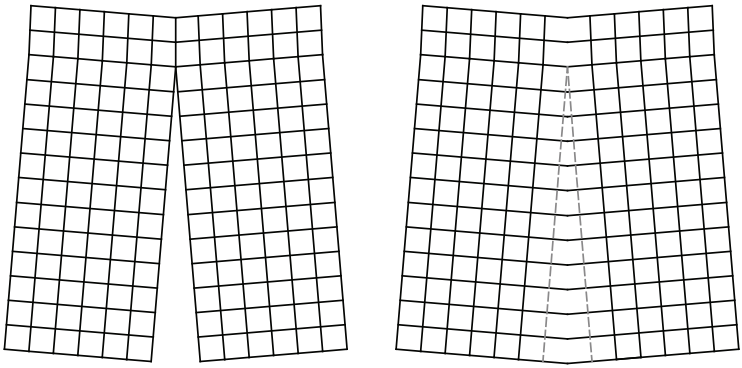

Figure 2.2.: Discrete (non-meshless) approach (left) and X-FEM (right) for crack modelling.

SUKUMAR et al. extended the applications of X-FEM to the modelling of a three-dimensional crack in [117] using a geometric explicit description for a plane crack surface, while DAUX et al. studied in [31] cracks with multiple branches, multiple holes and cracks emanating from holes, by introducing the branched (or junction) enrichment to model a branched crack. The use of level set techniques to represent the crack location was applied for the first time by STOLARSKA et al. [113] to the modelling of crack growth, and by SUKUMAR et al. [114] to the modelling of holes and inclusions. Within this approach, only nodal data are required to describe the crack geometry. Level set functions were introduced in [53, 84] to describe the growth of non-planar three-dimensional cracks. The multiple crack growth in brittle materials was analysed in [24], where a simpler method for treating crack junction was developed.

The accuracy, convergence and stability of the method are the aim of the works presented by BECHET et al. [13], LABORDE et al. [67] and CHAHINE et al. [27], who proposed some improvements to X-FEM in order to obtain an optimal accuracy in fracture mechanics problems. Furthermore, FRIES [51] proposed a corrected (or modified) X-FEM approximation for blending elements in order to improve the overall convergence rate. This is achieved by modifying the enrichment functions and the enrichment strategy of all nodes belonging to blending elements. LÖHNERT et al. [76] extended the corrected X-FEM to three-dimensional crack modelling. They also addressed several computational issues regarding 3D modelling, in particular quadra-

ture rules for elements with discontinuities. A simple, robust and efficient stabilization technique is presented in [75] for badly conditioned equation systems within the framework of the extended finite element method. In [77], this technique is extended to nonlinear and dynamic fracture mechanics problems.

X-FEM has been also studied by FLEMING in his doctoral thesis [50], who applied the method for the simulation of quasi-static and dynamic crack propagation in brittle materials. In that work, different crack propagation criteria, time integration schemes and enrichment strategies are analysed and compared with available data to prove the robustness of X-FEM.

The first applications of X-FEM for the modelling of cohesive crack growth were introduced in [84]. Here, non-singular near-tip functions are used to model the displacement field around the crack tip. Crack growth is governed by requiring the Stress Intensity Factor (SIF) K_I at the crack tip to vanish. This criterion is referred to as the zero SIF condition [98]. Moreover, the crack is assumed to propagate in the direction of the maximum tangential stress. It must be mentioned, however, that the use of displacements jumps in a finite element framework to model cohesive cracks was already considered in [122]. In that work, WELLS et al. treated the crack using only a discontinuous function (HEAVISIDE function) and, consequently, the crack tip must be always located at element edges. The principal stress criterion is used to describe crack growth. WELLS et al. proposed a non-local evaluation of the stress state at the tip, since this approach leads to a more reliable prediction of the crack path. The crack is extended perpendicular to the maximum non-local principal stress direction. In [130], all cracked elements are also enriched with a discontinuous function (sign function), but the development of a new crack-tip element allows the crack to propagate to any location inside an element. The crack-tip element proposed by ZI et al. is further improved by ASFERG et al. [4]. The zero SIF condition is reformulated in terms of the stresses at the tip: the component of the stress field in the normal direction to the crack at the tip is considered to be equal to the tensile strength of the material. This condition is referred to by the authors as the stress condition. A cubic displacement interpolation function is used in [80] to enhance the approximate fields in order to represent the crack and, particularly, the typical cusp-like shape of the process zone at the crack tip. Similarly, stress-based criteria are used to describe crack growth.

Further studies have been performed on X-FEM and its application to cohesive crack models over the years. In [105, 106], an innovative method for the simulation of multiple cohesive crack growth is described. The crack is not regarded as a single entity that propagates continuously, but is represented by a collection of overlapping cohesive segments with a finite length. The method allows for complex crack patterns, including the simulation of crack nucleation at multiple locations followed by growth and coalescence. In [83], a global energy-based method for the determination of the crack propagation length as well as for the crack propagation direction is proposed. XU et al. [127] used a rigid cohesive zone model to study effects of fracture criteria for mixed-mode cracks under plane strain conditions. ZAMANI et al. performed higher-order terms of the crack tip asymptotic fields as enriching functions [129]. BENVENUTI et al. proposed a modified X-FEM framework [19, 21], based on the study conducted by PATZÁK [94], to account for the finite width of the process zone. Within this approach, the crack is replaced by a narrow band of finite thickness in which the strain is highly localised but remains continuous. The displacement field is regularised by adding a regularised HEAVISIDE function by means of an internal length parameter. Instead of a cohesive constitutive law, the cohesive zone is characterised by a stress-strain law using a damage model. This method can then simulate both the formation of a process zone and its subsequent collapse into a macro-crack. JAŚKOWIEC et al. [61] presented a consistent algorithm for cohesive crack growth modelling, where a new two-dimensional formulation for the cohesive law is introduced, which can be used for both 2D and 3D cases. In [43], a method is proposed that can accurately describe brittle failure in the presence of cohesive forces in three-dimensional crack modelling. While in [25], a three-dimensional numerical model for the simulation of cohesive cracks in cementitious materials, such as concrete, in a hygro-mechanical framework is presented. Cohesive models have been also implemented into an X-FEM framework to simulate dynamic crack propagation [16, 131]. PEZESHKI et al. presented in [96] a combined continuous-discontinuous approach to model crack propagation under dynamic loading. In the continuum part of the model, gradient enhanced damage accounts for mesh independent material degradation and softening, and the loss of stiffness of the structure due to micro-cracking.

Furthermore, X-FEM has been used to simulate interface material failure including fibre-matrix debonding [55], composite delamination [120, 121] and bi-material interface cracks [116]. Particularly interesting is the work per-

formed by RADTKE et al. [100]. They proposed an extended finite element method that can represent discrete fibres in fibre-reinforced composites without remeshing them. The discontinuity present due to tangential debonding at the fibre-matrix interface is modelled with a HEAVISIDE enrichment. According to RADTKE et al., the thickness of the fibres are assumed to be negligible and, therefore, these are considered as 1D objects on a concrete matrix background. Likewise, a discontinuous (step) enrichment is used in [54] as an alternative to cohesive elements to represent the interface. Moreover, BENVENUTI [20] employed the regularised X-FEM technique presented in [19] to simulate delamination in FRP-reinforced concrete.

One of the first applications of X-FEM to the modelling of RC structures can be found in the doctoral thesis of HETTICH [56]. HETTICH employed X-FEM for the numerical simulation of multiple crack growth in an RC beam. He used the HEAVISIDE function for the enrichment, thus cracks are only allowed to propagate to element edges. The influence of the reinforcing bars on the structure is smeared over the elements by means of suitable constitutive relationships. HETTICH assumed a perfect bond between both the reinforcement and the surrounding concrete and, therefore, no slip is considered. Non-local stress-based criteria as those provided by WELLS [122] are used to predict tensile failure. On the other hand, in [59], an approach based on ED-FEM (embedded discontinuity finite element method) for the local representation of concrete cracking and on X-FEM for the modelling of the bond-slip along the reinforcement is used to model fracture in RC structures. LIAO et al. [73] proposed a model based on X-FEM for the modelling of RC beams in fire conditions. X-FEM is incorporated into plain concrete elements in order to model concrete cracking, while reinforcing bar elements and bond-link elements are used to represent the reinforcing bars and the interface, respectively. ORLANDO et al. [91] used the regularised X-FEM approach [19] to analyse a pull-out test on a steel bar and a bending test on a strengthened RC beam. Both the bars and the FRP sheets are explicitly discretised, while the interfaces are represented by means of the regularised X-FEM.

The modelling of crack growth with frictional contact within the framework of the extended finite element method was first addressed in [37] by means of the LATIN method [68]. LIU et al. presented in [74] a contact algorithm for frictional crack propagation based on a penalty formulation. An extension to 3D contact problems was proposed by GENIAUT et al. [52] and MÜLLER-

HOEPPE et al. [87] in terms of the Lagrange multiplier technique and a penalty formulation, respectively.

A more detailed review of the state of the art and further information about X-FEM can be found in [17, 86, 98, 115].

Due to its robustness and popularity, X-FEM has been used for a wide branch of industrial problems. Some applications of X-FEM in fracture mechanics have been successfully incorporated into computational software such as LS-DYNA and ABAQUS. However, these applications are limited to the analysis of a single crack or a few non-interacting cracks. Furthermore, convergence difficulties may arise when modelling cohesive cracks because of the selection of the material properties. Regarding the modelling of RC structures, compatibility problems appear between the material models of the rest of the constituent parts and X-FEM.

3. Description of the problem

The chapter is arranged as follows. The first part introduces the governing equations and the weak formulation regarding a cracked concrete body. The constitutive behaviour along the crack surfaces is described by a cohesive crack model. Softening functions for both the cohesive normal traction and the shear traction are presented. The crack initiation and growth are described by means of stress-based criteria. A damage model is then introduced to represent the compressive failure of concrete, considering a parabola-line stress-strain relationship. Reinforcing bars are explicitly modelled and, therefore, its contribution to the weak form is considered independently. An elasto-plastic constitutive law with isotropic linear hardening is used as constitutive model for the reinforcing steel. Finally, the behaviour at the concrete-reinforcement interface is described by bond laws, which consider both bond-slip and dowel action.

3.1. Governing equations

Consider a concrete plate (body) of thickness h as shown in Figure 3.1. The body is crossed by N_c cracks, which are explicitly modelled. The Cartesian coordinate system $\{\boldsymbol{e}_x, \boldsymbol{e}_y, \boldsymbol{e}_z\}$ is defined in such a way that the middle surface of the undeformed body contains the Cartesian coordinates x and y, while the coordinate z is parallel to the thickness direction. The middle surface comprises an open domain $\Omega \subset R^2$ with a smooth boundary Γ. The boundary Γ is considered as the junction of the disjointed parts Γ_u, Γ_t and Γ_c, being $\hat{\boldsymbol{n}}$ its outward normal unit vector. Essential boundary conditions (DIRICHLET-type) are imposed on Γ_u, specifying the displacements in the contour, while natural conditions (NEUMANN-type) are applied on Γ_t. The cracks surfaces, represented by the internal boundary $\Gamma_c = \cup^j \Gamma_c^j$, comprise

the individual crack surfaces Γ_c^j, which are subject to the action of the cohesive tractions $\boldsymbol{t}^{j(+)}$ and $\boldsymbol{t}^{j(-)}$. The notation $[\,]^j$ reads: variable $[\,]$ associated with the crack j, being $j = 1$ to N_c.

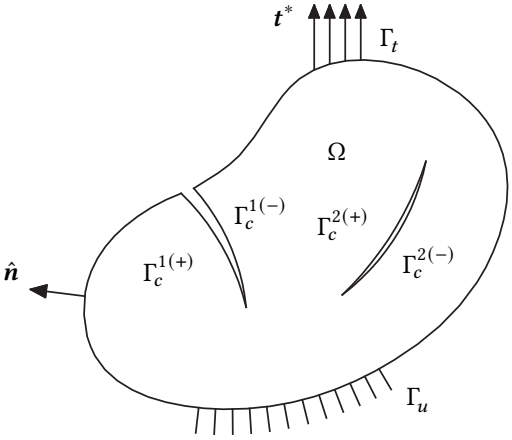

Figure 3.1.: Cracked body and boundary conditions.

The behaviour of the body is described in terms of the displacement field $\boldsymbol{u}$, the strain tensor $\boldsymbol{\epsilon}$ and the CAUCHY stress tensor $\boldsymbol{\sigma}$.

Under the assumption of small displacements, the strain tensor $\boldsymbol{\epsilon}$ can be expressed as the symmetrical part of the displacement gradient:

$$\boldsymbol{\epsilon} = \nabla^{sym}\boldsymbol{u}. \tag{3.1}$$

The constitutive relation governing the material behaviour of the body is given by the HOOKE's law[1]:

$$\boldsymbol{\sigma} = \mathbb{C} : \boldsymbol{\epsilon}, \tag{3.2}$$

where $\mathbb{C}$ is the fourth order stiffness tensor. This tensor is symmetrical and, for isotropic materials, will depend only on the modulus of elasticity E and the POISSON's ratio ν.

[1] The damage model will be discussed later in this chapter

An additional constitutive law is imposed on Γ_c^j, relating the cohesive traction $\boldsymbol{t}^{j(+)} = -\boldsymbol{t}^{j(-)} = \boldsymbol{t}^j$ to the relative displacement (or displacement jump) across the crack surfaces $\boldsymbol{\omega}^j$. The cohesive constitute law can be written as:

$$\boldsymbol{t}^j = f(\boldsymbol{\omega}^j), \tag{3.3}$$

$$\boldsymbol{\omega}^j = \boldsymbol{u}^{j(+)} - \boldsymbol{u}^{j(-)}. \tag{3.4}$$

In addition, for the case of crack growth, a crack propagation law is needed. This will be discussed in Section 3.2.

Then, the problem consists in finding a displacement field $\boldsymbol{u}$, satisfying the following governing equation in absence of body forces:

$$\nabla \cdot \boldsymbol{\sigma} = 0, \tag{3.5}$$

in the domain Ω occupied by the body; together with the boundary conditions:

$$\boldsymbol{u} = \boldsymbol{u}^* \quad \text{on } \Gamma_u, \tag{3.6}$$

$$\boldsymbol{\sigma} \cdot \hat{\boldsymbol{n}} = \boldsymbol{t}^* \quad \text{on } \Gamma_t, \tag{3.7}$$

$$\boldsymbol{\sigma} \cdot \hat{\boldsymbol{n}}^{j(+)} = -\boldsymbol{\sigma} \cdot \hat{\boldsymbol{n}}^{j(-)} = \boldsymbol{t}^{j(+)} = -\boldsymbol{t}^{j(-)} = \boldsymbol{t}^j \quad \text{on } \Gamma_c^j. \tag{3.8}$$

Herein, $\boldsymbol{u}^*$ and $\boldsymbol{t}^*$ are the prescribed displacements and tractions imposed over the contours, respectively.

Equations 3.1-3.8 define the strong form of the boundary value problem, which requires that the equilibrium be satisfied at each point. This strong requirement can be relaxed by demanding that the equilibrium be satisfied in a weaker, integral sense.

3.1.1. Weak form

The weak formulation, unlike the strong formulation, defines the boundary value problem through an integral form. In this way, a strong continuity of the displacement field is not required. This allows to easily find, through

numerical methods, approximate solutions, even when an exact solution for the strong form is not easily to obtain.

To formulate the weak form of the reference problem presented in the previous section, it is necessary to define, on one hand, a space of admissible displacements:

$$\mathcal{U} = \left\{ \boldsymbol{u} \in \mathcal{V} \text{ and discontinuous on } \Gamma_c \mid \boldsymbol{u} = \boldsymbol{u}^* \text{ on } \Gamma_u \right\}; \tag{3.9}$$

and, on the other hand, a space of test functions:

$$\mathcal{U}_0 = \left\{ \delta\boldsymbol{u} \in \mathcal{V} \text{ and discontinuous on } \Gamma_c \mid \delta\boldsymbol{u} = 0 \text{ on } \Gamma_u \right\}. \tag{3.10}$$

The space $\mathcal{V}$ is related to the regularity of the solution. Then, the weak form is to find $\boldsymbol{u} \in \mathcal{U}$ such that:

$$\begin{aligned} &\int_\Omega h\delta\boldsymbol{\epsilon} : \boldsymbol{\sigma}\, dA - \int_{\Gamma_t} h\delta\boldsymbol{u} \cdot \boldsymbol{t}^*\, ds \\ &- \sum_{j=1}^{n_c} \left(\int_{\Gamma_c^{j(+)}} h\delta\boldsymbol{u}^{j(+)} \cdot \boldsymbol{t}^{j(+)}\, ds + \int_{\Gamma_c^{j(-)}} h\delta\boldsymbol{u}^{j(-)} \cdot \boldsymbol{t}^{j(-)}\, ds \right) = 0. \end{aligned} \tag{3.11}$$

Using the relations 3.4 and 3.8, the equation given above can be expressed as:

$$\int_\Omega h\delta\boldsymbol{\epsilon} : \boldsymbol{\sigma}\, dA - \int_{\Gamma_t} h\delta\boldsymbol{u} \cdot \boldsymbol{t}^*\, ds + \sum_{j=1}^{n_c} \int_{\Gamma_c^j} h\delta\boldsymbol{\omega}^j \cdot \boldsymbol{t}^j\, ds = 0. \tag{3.12}$$

Calling δW^{int} the virtual work of the internal forces:

$$\delta W^{int} = \int_\Omega h\delta\boldsymbol{\epsilon} : \boldsymbol{\sigma}\, dA, \tag{3.13}$$

δW^{ext} the virtual work of the external forces:

$$\delta W^{ext} = \int_{\Gamma_t} h\delta\boldsymbol{u} \cdot \boldsymbol{t}^*\, ds, \tag{3.14}$$

and δW^{coh} the virtual work of the cohesive forces:

$$\delta W^{coh} = \sum_{j=1}^{n_c} \int_{\Gamma_c^j} h \delta \boldsymbol{\omega}^j \cdot \boldsymbol{t}^j \, ds, \tag{3.15}$$

the weak form can be written in terms of the virtual works as:

$$\delta W^{int} + \delta W^{coh} = \delta W^{ext}. \tag{3.16}$$

In the deduction of the weak form, no assumption regarding the material behaviour has been made and, therefore, this formulation is valid for both linear and non-linear constitutive models.

3.2. Cohesive crack model

In cohesive crack models, the Fracture Process Zone (FPZ) is modelled as a fictitious[2] widthless crack ahead of the macro-crack, with cohesive closure tractions acting across its surfaces. The non-linear behaviour inside the FPZ is described by a constitutive law, relating the cohesive tractions to the displacement jump across the crack surfaces. This law defines the gradual loss of cohesion along the crack at increasing deformation, because of the presence of micro-cracks, micro-voids and similar defects.

The model distinguishes between three different zones: a remote undamaged zone, where the fracture has not yet started; the fracture process zone, formed as soon as a critical strength has been reached; and a completely damaged zone (macro-crack).

The cohesive crack model is formulated in a local coordinate system at a point $\boldsymbol{x}$ associated to the crack, orientated in such a way that the local axis $\hat{\boldsymbol{e}}_1$ is tangent to the crack surface, while the local axis $\hat{\boldsymbol{e}}_2$, normal (see Figure 3.2). The sense of $\hat{\boldsymbol{e}}_3$ is chosen such that $\hat{\boldsymbol{e}}_1 \times \hat{\boldsymbol{e}}_2 = \hat{\boldsymbol{e}}_3$. The cohesive traction $\boldsymbol{t}$ can be decomposed in the local coordinate system into the normal component

[2] The model is also known as the fictitious crack model.

t_n, known as normal traction, and into the shear (tangential) component t_s, known as shear traction, as:

$$\boldsymbol{t} = t_n \hat{\boldsymbol{n}} + t_s \hat{\boldsymbol{t}}. \tag{3.17}$$

Likewise, the relative displacement $\boldsymbol{\omega}$ can be decomposed into the normal component ω_n, known as crack opening, and into the shear (tangential) component ω_s, known as crack sliding, as:

$$\boldsymbol{\omega} = \omega_n \hat{\boldsymbol{n}} + \omega_s \hat{\boldsymbol{t}}. \tag{3.18}$$

These transformations can be simplified as follows:

$$\boldsymbol{\omega} = \boldsymbol{R}\boldsymbol{\Omega}, \tag{3.19}$$

$$\boldsymbol{t} = \boldsymbol{R}\boldsymbol{\mathcal{T}}, \tag{3.20}$$

where $\boldsymbol{R}$ is the transformation matrix from the local into the global coordinate system:

$$\boldsymbol{R} = \begin{bmatrix} \hat{\boldsymbol{n}} & \hat{\boldsymbol{t}} \end{bmatrix}, \tag{3.21}$$

and $\boldsymbol{\Omega}$ and $\boldsymbol{\mathcal{T}}$ are the local relative displacement and the local cohesive traction, respectively:

$$\boldsymbol{\Omega} = \begin{bmatrix} \omega_n & \omega_s \end{bmatrix}^T, \tag{3.22}$$

$$\boldsymbol{\mathcal{T}} = \begin{bmatrix} t_n & t_s \end{bmatrix}^T. \tag{3.23}$$

Figure 3.3 illustrates the cohesive model proposed by HILLERBORG et al. [57]. The model is described only for mode *I*, however, it can also be applied to model other types of fracture, such as the shear fracture of the mode *II* or mode *III*. As can be seen, the cohesive traction t_n decreases continuously at increasing crack opening ω_n, from a maximum at the fictitious crack tip (mathematical tip) to zero at the macro-crack tip (physical tip), where the separation reaches the critical value ω_c, beyond which the fictitious crack becomes a traction-free open crack. The model is therefore independent of the width of the fracture process zone. Outside the FPZ, the material behaves linear-elastic or elastic-plastic.

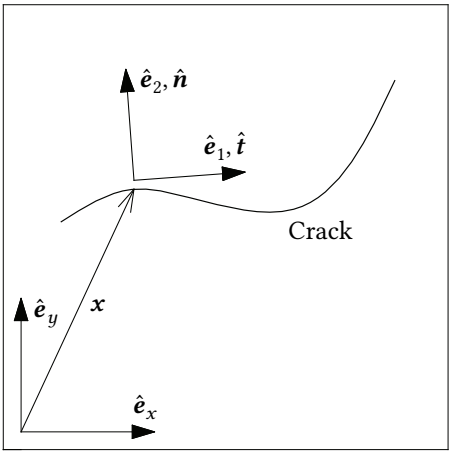

Figure 3.2.: Local coordinate system.

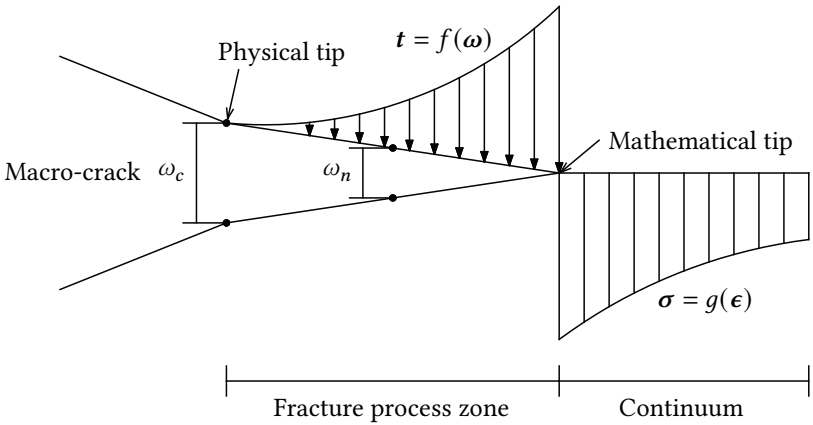

Figure 3.3.: Cohesive crack model.

The normal traction across the crack faces is related to the crack opening through softening functions, known as traction-separation functions, i.e. $t_n = f(\omega_n)$, which can be considered as an intrinsic property of the material and, as such, should be obtained experimentally. In general, the traction-separation function can be defined using only two parameters: the tensile strength f_t

and the specific fracture energy G_f. The specific fracture energy corresponds to the energy required to create a new crack surface per unit of area and, therefore, can be identified with the area enclosed under the softening function.

There are different kinds of softening functions available in the literature. Some of the most commonly used laws are: linear laws [57], bilinear laws [47, 95, 123], exponential laws [65], non-linear laws [104], among others. These laws are compared in Figure 3.4.

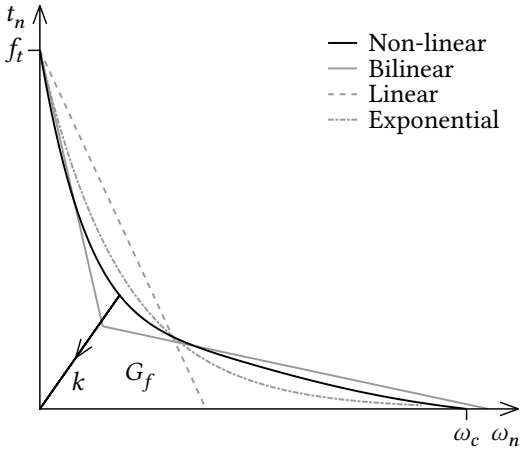

Figure 3.4.: Traction-separation functions.

In this work, the non-linear softening function proposed by REINHARDT et al. [104] is used:

$$t_n = \begin{cases} f_t \left\{ \left[1 + \left(\dfrac{c_1 \omega_n}{\omega_c} \right)^3 \right] \exp\left(\dfrac{-c_2 \omega_n}{\omega_c} \right) - \dfrac{\omega_n}{\omega_c} \left(1 + c_1^3 \right) \exp\left(-c_2 \right) \right\} & \text{for} \quad 0 \leq \omega \leq \omega_c, \\ 0 & \text{for} \quad \omega > \omega_c, \end{cases} \tag{3.24}$$

where c_1 and c_2 are material constants. For normal concrete, these parameters are considered as $c_1 = 3$ and $c_2 = 6.93$.

Using these values, the critical opening ω_c can be calculated from:

$$\omega_c = \frac{5.136 G_f}{f_t}. \tag{3.25}$$

Aggregate interlocking at crack surfaces leads to the development of shear tractions. In this work, the shear model proposed in [122] is adopted. WELLS et al. treated the shear stiffness as a function of both the crack opening ω_n and the crack sliding ω_s. They presented the following expression for the calculation of the shear traction t_s:

$$t_s = d_0 \exp\left(h_s \omega_n\right) \omega_s, \tag{3.26}$$

where d_0 is the initial shear stiffness (when $\omega_n = 0$). The constant h_s controls the decrease in the stiffness:

$$h_s = \ln\left(\frac{d_1}{d_0}\right), \tag{3.27}$$

being d_1 the shear stiffness when $\omega_n = 1$.

3.2.1. Cyclic loading

Since damage is considered as an irreversible process, the loading history of the material needs to be taken into account in loading/unloading cycles[3]. Therefore, it is convenient to introduce a history parameter:

$$\kappa(t) = \max_{T \leq t} \omega_n(T), \tag{3.28}$$

characterising the maximum crack opening reached in the previous history of the material. Then, local loading conditions are given by $\omega_n \geq \kappa$, in which the loading curve defined by the traction-separation law is used. When $\omega_n < \kappa$, local unloading or reloading take place. The unloading/reloading path follows a linear relationship given by:

$$t_n = t_{n\ max} + k(\omega_n - \kappa), \tag{3.29}$$

[3] As well, even under monotonic loading conditions, local unloading can occur.

where $t_{n\ max}$ is the normal traction associated to $\omega_n = \kappa$, and k, the secant stiffness.

If the crack opening becomes negative during unloading, a penalty stiffness ϵ_N will be used to avoid penetration of the crack faces, i.e. $t_n = \epsilon_N \omega_n$. The penalty parameter $\epsilon_N > 0$ can be interpreted as a spring stiffness.

The crack shear is also made a function of the history parameter and, consequently, the shear traction takes the following form:

$$t_s = d_0 \exp\left(h_s \kappa\right) \omega_s. \tag{3.30}$$

The continuous degradation of the cohesive traction due to cyclic loading is not considered in this work.

3.2.2. Crack initiation and growth

Within the framework of a cohesive crack model, both crack initiation process and crack growth process can be described using stress-based criteria. In this regard, the maximum stress criterion, also known as RANKINE criterion, is used to predict tensile failure. Then, a crack is assumed to initiate its propagation when the maximum principal stress at a point exceeds the concrete tensile strength f_t. The maximum principal stress is given by:

$$\sigma_{max} = \frac{\sigma_{xx} + \sigma_{yy}}{2} + \sqrt{\left(\frac{\sigma_{xx} - \sigma_{yy}}{2}\right)^2 + \sigma_{xy}^2}. \tag{3.31}$$

The newly formed crack will be propagated in the direction perpendicular to the direction of the maximum principal stress.

The orientation of the principal planes can be determined by means of the MOHR circle and can also be found from the following expression:

$$\theta_I = \frac{1}{2} \arctan \frac{2\sigma_{xy}}{\sigma_{xx} - \sigma_{yy}}. \tag{3.32}$$

This equation defines two values for θ_I which are 90° apart, i.e. θ_{I_1} and $\theta_{I_2} = \theta_{I_1} + 90^\circ$. The direction of the maximum principal stress can be then calculated from:

$$\theta_{max} = \begin{cases} \theta_{I_1} & \text{if} \quad \sigma_{max} = \boldsymbol{n}_{I_1}^T \boldsymbol{\sigma} \boldsymbol{n}_{I_1}, \\ \theta_{I_2} & \text{if} \quad \sigma_{max} = \boldsymbol{n}_{I_2}^T \boldsymbol{\sigma} \boldsymbol{n}_{I_2}, \end{cases} \tag{3.33}$$

where $\boldsymbol{n}_{I_1} = \left[\cos\theta_{I_1} \sin\theta_{I_1}\right]^T$ and $\boldsymbol{n}_{I_2} = \left[\cos\theta_{I_2} \sin\theta_{I_2}\right]^T$.

Finally, the propagation angle θ_p is equal to $\theta_{max} + 90^\circ$.

For existing cracks, the stress criterion presented in [130] is adopted. According to this criterion, a crack propagates when the stress projection in the normal direction $\hat{\boldsymbol{n}}$ at the crack tip reaches the tensile strength, i.e.:

$$\sigma_n = \hat{\boldsymbol{n}}^T \boldsymbol{\sigma} \hat{\boldsymbol{n}} = f_t. \tag{3.34}$$

Since the tip of the discontinuity lies on a point where the stresses are not known exactly, a local evaluation of the stress state at the tip is not suitable. To overcome this, it is common to take the averaged stress or the so-called non-local stress as fracture criterion. The non-local formulation suggested by WELLS et al. [122] is adopted. The non-local stress is calculated as a weighted average of the stresses within an influence radius R around the crack tip:

$$\tilde{\boldsymbol{\sigma}} = \left(\int_{\Omega_R} w(r)\, d\Omega \right)^{-1} \int_{\Omega_R} \boldsymbol{\sigma}(\boldsymbol{x}) w(r)\, d\Omega, \tag{3.35}$$

where w is a GAUSSian weight function. In this work, the function suggested in [82] is used:

$$w(r) = \frac{1}{l\sqrt{2\pi}} \exp\left(\frac{-r^2}{4l^2}\right). \tag{3.36}$$

Here, r is the distance of a point $\boldsymbol{p}(\boldsymbol{x})$ to the crack tip, and l determines the decline of the weight function w with respect to r.

Taking this into account, Equation 3.34 can be rewritten in terms of the non-local stress as:

$$\tilde{\sigma}_n = \hat{\boldsymbol{n}}^T \tilde{\boldsymbol{\sigma}} \hat{\boldsymbol{n}} = f_t. \tag{3.37}$$

The direction of crack growth is also determined using the RANKINE criterion, i.e. the crack propagates in the direction perpendicular to the maximum non-local principal stress direction.

3.3. Continuum damage model

An isotropic damage model is used to describe the behaviour of concrete in compression. The major advantage of a damage approach is that it offers the possibility to model fractured zones where damage is not necessarily localised, i.e. there are no dominant cracks, thus being suitable for the modelling of compressive failure.

The constitutive law 3.2 is then replaced by:

$$\boldsymbol{\sigma} = (1 - D)\,\mathbb{C} : \boldsymbol{\epsilon}, \tag{3.38}$$

where D is a damage variable, which represents the degree of mechanical degradation of the material. The damage variable takes the value $D = 0$, for an intact material, and, as the degradation increases, reaches the limit value $D = 1$, corresponding to a completely damaged state.

Defining the effective stress tensor as:

$$\bar{\boldsymbol{\sigma}} = \mathbb{C} : \boldsymbol{\epsilon}, \tag{3.39}$$

Equation 3.38 can be alternatively written as:

$$\boldsymbol{\sigma} = (1 - D)\bar{\boldsymbol{\sigma}}. \tag{3.40}$$

Note that the effective stress tensor is governed by the HOOKE's law.

Damage evolution is usually expressed in terms of the loading function h, which specifies the elastic domain and the states at which damage grows. This function has the following form:

$$h(\boldsymbol{\epsilon}, \kappa) = \tilde{\epsilon}(\boldsymbol{\epsilon}) - \kappa, \tag{3.41}$$

where $\tilde{\epsilon}$ is the equivalent strain, i.e. a scalar measure of the strain level. The history parameter κ, as in the case of the cohesive crack model, corresponds to the largest value of the equivalent strain ever reached in the history of the material up to its current state. Formally, this can be defined as:

$$\kappa(t) = \max_{T \leq t} \tilde{\epsilon}(T). \tag{3.42}$$

Loading is then given by $h \geq 0$, while unloading or reloading, by $h < 0$. The unloading/reloading behaviour can be modelled using the secant stiffness $E_s = (1 - D)E$. Damage is initiated when the equivalent strain reaches an initial threshold $\tilde{\epsilon}_0$.

The damage model is completed by a material function $D = D(\kappa, \tilde{\epsilon})$, giving the dependence of the damage variable on the loading history.

In this work, the stress-strain curve shown in Figure 3.5 is adopted for the modelling of the compressive behaviour, which corresponds to a modified version of the stress-strain relation for uniaxial compression presented in [47]. The compressive stress σ_c is assumed to remain constant once the compressive strength f_c is exceeded and, therefore, no softening behaviour is considered[4].

In this regard, the minimum principal strain is chosen to define the equivalent strain:

$$\tilde{\epsilon} = \frac{\epsilon_{xx} + \epsilon_{yy}}{2} - \sqrt{\left(\frac{\epsilon_{xx} - \epsilon_{yy}}{2}\right)^2 + \epsilon_{xy}^2}. \tag{3.43}$$

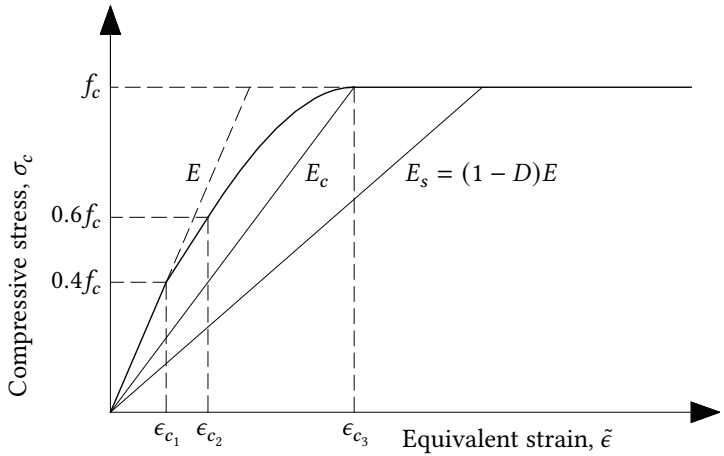

Figure 3.5.: Stress-strain relationship for concrete under compression.

[4] Thus, the convergence difficulties that appeared during the development of the finite element program are avoided.

For loading conditions, the damage variable is computed using the secant stiffness:

$$D = 1 - \frac{E_s}{E}, \tag{3.44}$$

which in turn can be calculated from:

$$E_s = \frac{\sigma_c}{\tilde{\epsilon}}. \tag{3.45}$$

The relation between σ_c and $\tilde{\epsilon}$ is described by:

$$\sigma_c = \begin{cases} E\tilde{\epsilon} & \text{if} \quad \tilde{\epsilon} \geq \epsilon_{c_1}, \\ -f_c\left[0.4 + 0.2\left(\tilde{\epsilon} - \epsilon_{c_1}\right)/\left(\epsilon_{c_2} - \epsilon_{c_1}\right)\right] & \text{if} \quad \epsilon_{c_1} > \tilde{\epsilon} \geq \epsilon_{c_2}, \\ -f_c\left(k\eta - \eta^2\right)/\left[1 + \left(k - 2\right)\eta\right] & \text{if} \quad \epsilon_{c_2} > \tilde{\epsilon} \geq \epsilon_{c_3}, \\ -f_c & \text{if} \quad \tilde{\epsilon} < \epsilon_{c_3}, \end{cases} \tag{3.46}$$

where $\eta = \tilde{\epsilon}/\epsilon_{c_3}$ and $k = E/E_c$.

The value ϵ_{c_3} is the strain at maximum compressive stress, while E_c, the secant modulus from the origin to the peak compressive stress, i.e. $E_c = f_c/\epsilon_{c_3}$. The upper limit ϵ_{c_2} corresponds to the minimum root of the quadratic equation:

$$\epsilon_{c_3}^{-2} x^2 - \left[1.2 + 0.4k\right]\epsilon_{c_3}^{-2} x + 0.6 = 0. \tag{3.47}$$

$\epsilon_{c_1} = -0.4 f_c/E$ defines the elastic domain and, consequently, can be identified with the initial threshold $\tilde{\epsilon}_0$.

3.4. Reinforcing bars

Reinforcing bars embedded in a concrete bulk can be explicitly modelled using discrete approaches. The main advantage of these approaches is the relatively accurate representation of the mechanical behaviour of the reinforcement, and the interface between the reinforcement and the surrounding concrete.

Consider then a domain Ω_r occupied by the reinforcement and the boundary $\partial\Omega_r$ representing the interface between both materials. The internal virtual

work associated with the reinforcement muss be incorporated to the energy balance presented in Section 3.1.1, by adding the following term to Equation 3.13:

$$\delta W^{int} = \int_{\Omega_r} \tilde{h}(\boldsymbol{x}) \delta \boldsymbol{\epsilon} : \boldsymbol{\sigma} \, dA, \tag{3.48}$$

where $\tilde{h}(\boldsymbol{x})$ corresponds to an equivalent reinforcement thickness.

The transfer of forces along the interface is modelled through bond laws, which relate the interfacial stress $\boldsymbol{\tau}$ to the relative displacement between the reinforcement and the concrete bulk across the interface $\boldsymbol{w}$. In this regard, the energy balance of the system must be expanded by adding a bond term:

$$\delta W^{int} = \delta W^{ext} - \delta W^{coh} - \delta W^{bond}, \tag{3.49}$$

where W^{bond} is the work of the bond stresses along the interface and is given by:

$$\delta W^{bond} = \int_{\partial\Omega_r} \delta \boldsymbol{w} \boldsymbol{\tau} \, dA. \tag{3.50}$$

3.4.1. Constitutive model

A classical elasto-plastic constitutive law with isotropic linear hardening is used to model the non-linear behaviour of the reinforcing steel, once the yield strength is exceeded. Since only the stress along the steel axis is significant, a yield function based on the steel axial stress is adopted:

$$f(\boldsymbol{\sigma}, \kappa) = \left\| \hat{\boldsymbol{t}}^T \boldsymbol{\sigma} \hat{\boldsymbol{t}} \right\| - \left(f_y + H\kappa \right), \tag{3.51}$$

where $\hat{\boldsymbol{t}}$ is the unit tangent vector to the reinforcing steel, while f_y, H and κ are the yield strength, plastic modulus, and hardening variable, respectively.

A detailed description of elastoplastic models and their implementation can be found in [35].

The use of kinematic hardening rules is not considered in this work. Therefore, the BAUSCHINGER effect observed in metals cannot be modelled.

3.5. Bond model

3.5.1. Bond behaviour

Reinforced concrete depends on the combined action of the concrete and its embedded reinforcement to ensure proper operation during service life. This action would not be possible without a successful transfer of bond forces along the interface between both materials. According to LEONHARDT [69], the transfer of forces is mainly provided through chemical adhesion, friction and, primarily, through bearing of the reinforcing steel ribs on the surrounding concrete. Moreover, there are many factors that influence bond behaviour such as rib geometry and spacing, bar position and orientation, concrete strength and cover, among others. Bond has a decisive influence on crack formation and, hence, affects the spacing between cracks and the cracks width. In this regard, bond plays a very important role in most aspects of reinforced concrete behaviour and determines, ultimately, the global structural response.

The force transfer along the interface is always accompanied by a relative displacement between both materials. The relative displacement tangential to the interface is commonly called slip and is denoted by s, while the relative displacement normal to the interface is called radial opening and is represented by w. The transferred forces are described normally in terms of stresses. In this respect, the interfacial stress field $\boldsymbol{\tau}$ acting along the interface can be divided into the tangential component τ, and into the normal component σ. Usually, in the literature, the tangential component τ is called bond stress, while the normal component σ, radial stress; this notation will be adopted in this work. The relationships between the global and the local components are given by the transformations:

$$\boldsymbol{w} = \boldsymbol{R}\boldsymbol{\check{W}}, \tag{3.52}$$

$$\boldsymbol{\tau} = \boldsymbol{R}\boldsymbol{T}, \tag{3.53}$$

where the transformation matrix $\boldsymbol{R}$ is defined in the same way as in Equation 3.21. In this case, $\hat{\boldsymbol{n}}$ and $\hat{\boldsymbol{t}}$ are the unit vectors of the local coordinate system associated to the interface, see Figure 4.8.

Vectors $\boldsymbol{W}$ and $\boldsymbol{T}$ are the local relative displacement field and the local interfacial stress field, respectively:

$$\boldsymbol{W} = \begin{bmatrix} w & s \end{bmatrix}^T, \tag{3.54}$$

$$\boldsymbol{T} = \begin{bmatrix} \sigma & \tau \end{bmatrix}^T. \tag{3.55}$$

The bond mechanisms are well known due to the extensive amount of experimental, analytical and numerical works that have been made during the last 50 years. A good overview can be found in [44]. Figure 3.6 shows an idealisation, drawn from these studies, of the interaction between the concrete and a bar subjected to a pull-out force.

At the beginning of loading, the main mechanism resisting the external force is the chemical adhesion. At this stage, a certain displacement occurs, even though no measurable bar slip is observed. This displacement occurs due to the localised strains near the interface as a result of highly localised stresses arising close to the edge of the ribs. For higher deformations, the chemical adhesion breaks down and the ribs of the bar induce large bearing stresses in the concrete, thus originating micro-cracks and, consequently, allowing the bar to slip. As the slip of the bar increases, ribs exert an increasing bearing action against the concrete and, if the bar is not adequately confined, splitting cracks may appear along the reinforcing bar. If enough resistance to splitting can be provided, the bond stress can reach the maximum bond strength. At increasing slip values, the bearing mechanism breaks down and the bond strength starts to decrease. The residual bond strength is mainly dependent on the frictional resistance. Under continued loading, the interface is smoothed due to wear and compaction, leading to a further decrease of the bond stress.

In the case of plain bars, smooth reinforcing bars without ribs, bond is achieved through adhesion and, partly, through stirrups and concrete shrinkage. Once the adhesive bond breaks down, the transfer of forces is provided, mainly, by friction. Therefore, the bond strength of deformed bars is significantly higher compared to plain bars.

The behaviour exposed above results in a local bond stress versus slip history such as that shown in Figure 3.6b, which can be used to develop bond stress-slip relationships for practical design and numerical analysis.

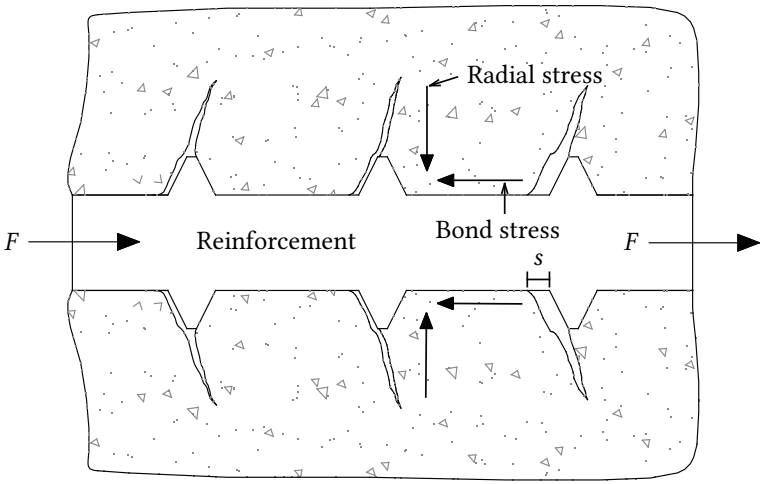

(a) Bond forces along the interface between reinforcement and concrete.

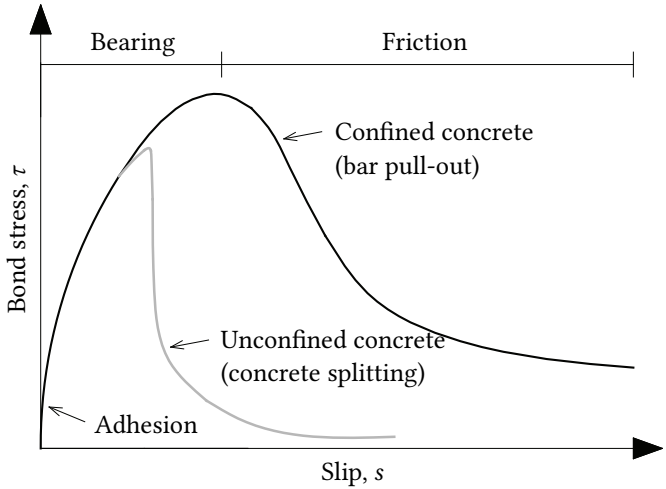

(b) Bond stress versus slip history.

Figure 3.6.: Idealised bond-slip behaviour between concrete and a deformed bar in pull-out test.

3.5.2. Bond constitutive law

Within a discrete approach, the bond behaviour, as in the case of the cohesive cracks, can be best described by means of bond constitutive laws, which define relationships between the stresses acting on the interface and the corresponding relative displacements. In this study, the bond law is assumed to be uncoupled, i.e. the bond stress τ is independent of the opening w, while the radial stress σ is independent of the slip s.

3.5.2.1. Bond-slip relationship

Several bond stress-slip relationships and corresponding bond models have been proposed in the last decades. Some of the most relevant include the models of REHM [103], KOBARG [66] and SCHOBER [111], and those proposed in design codes such as the CEB-FIP MODEL CODE 2010 [47], this last based on the work of ELIGEHAUSEN et al. [42]. A more detailed description can be found in [5].

In this work, the bond stress-slip relationship according to CEB-FIP MODEL CODE 2010 shown in Figure 3.7 is adopted:

$$\tau(s) = \begin{cases} \tau_{max} \left(\dfrac{s}{s_1}\right)^{\alpha} & \text{for} \quad 0 \leq s \leq s_1, \\ \tau_{max} & \text{for} \quad s_1 \leq s \leq s_2, \\ \tau_{max} - \left(\tau_{max} - \tau_f\right) \dfrac{(s - s_2)}{(s_3 - s_2)} & \text{for} \quad s_2 \leq s \leq s_3, \\ \tau_f & \text{for} \quad s_3 < s. \end{cases} \tag{3.56}$$

The unloading branch of the bond stress-slip relationship follows a linear relationship to/from the origin.

The bond strength may be affected by the reduction in the cross area of the reinforcing bars once yielding starts. In order to take this phenomenon into account, CEB-FIP proposes that, for reinforcement loaded beyond yield, the

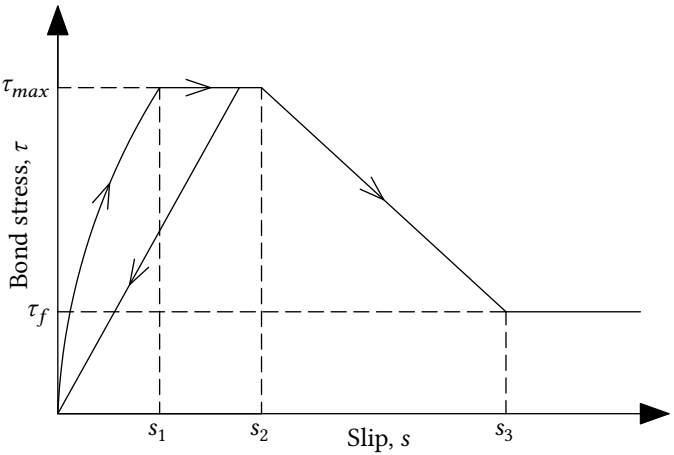

Figure 3.7.: Bond stress-slip relationship.

bond stress τ according to Equation 3.56 is to be reduced by the factor Ω_y, given by:

$$\Omega_y = \begin{cases} 1 & \text{for} \quad \epsilon_s \leq \epsilon_{sy}, \\ 1 - 0.85\left(1 - e^{-5a^b}\right) & \text{for} \quad \epsilon_{sy} \leq \epsilon_s \leq \epsilon_{su}, \end{cases} \tag{3.57}$$

where ϵ_s is the steel strain, ϵ_{sy}, the yield strain and ϵ_{su}, the ultimate tensile strain of the reinforcing steel. The coefficients a and b are given by:

$$a = \frac{\epsilon_s - \epsilon_{su}}{\epsilon_{su} - \epsilon_{sy}}, \qquad b = \left(2 - \frac{f_u}{f_y}\right)^2, \tag{3.58}$$

with f_y and f_u being the yield and ultimate tensile strength, respectively.

Additionally, the presence of a transverse crack generates a bond deterioration zone, which reduces the bond strength. The CEB-FIP therefore proposes that, for those parts which are at a distance $x \leq 2\phi$ from a transverse crack, the bond stress τ should be modified by the factor Ω_λ:

$$\Omega_\lambda = 0.5\frac{x}{\phi}. \tag{3.59}$$

This law does not consider the fracture process zone (FPZ) and, therefore, the degradation is associated only with the macro-crack. In this work, a modified law that takes into account the presence of the FPZ is proposed.

The degree of deterioration in the bond zone near the transverse crack is directly related to the current damage state of the fracture process zone, which, in cohesive crack models, is associated with the transfer load capacity of the cohesive crack, characterised by the cohesive normal traction t_n. Considering the ratio $\frac{t_n(\kappa)}{f_t}$, where κ is the maximum crack opening reached in the previous history of the crack at the concrete-reinforcement interface level, it is possible to rewrite the Equation 3.59 as follows:

$$\Omega_\lambda = 0.5\frac{x}{\phi} + \frac{t_n(\kappa)}{f_t}\left(1 - 0.5\frac{x}{\phi}\right). \tag{3.60}$$

The coefficient $t_n(\kappa)/f_t$ characterises the degree of damage of the FPZ and varies from one, for uncracked concrete, to zero, for completely cracked (macro-crack). It should be noted that for this last case ($t_n(\kappa)/f_t = 0$), the CEB-FIP proposal is recovered. Both proposals are compared in Figure 3.8.

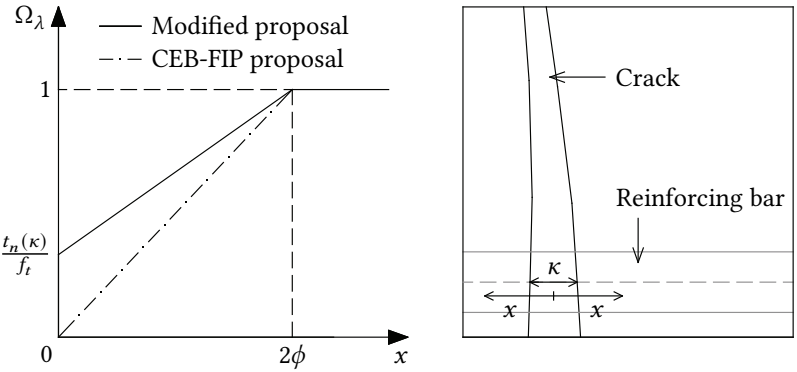

Figure 3.8.: Modified factor Ω_λ.

The modified bond stress τ is then given by:

$$\tau(s) = \Omega_y \Omega_\lambda \tau_0(s), \tag{3.61}$$

where τ_0 is the bond stress according to the Equation 3.56.

Due to the symmetry presents in the bond behaviour, the previous equation is also valid for negatives values of s. Thus, cyclic loading can be simulated.

3.5.2.2. Dowel action

When an inclined shear crack reaches the main reinforcing bars, a certain amount of shear is transferred across the crack because of the local bending and shear resistance provided by the reinforcement. This phenomenon is known as dowel action and is considered an important component of the overall shear resistance capacity of reinforced concrete structures. The dowel action is characterised by local bending and shearing of the bars and by highly localised compressive stresses in the surrounding concrete, which can be significantly higher than the uniaxial compressive strength. In this work, dowel action is characterised by suitable constitutive relationships along the concrete-reinforcement interface and, consequentially, its constitutive behaviour is defined in terms of the opening w and the radial stress σ. The empirical formulation proposed by BRENNA et al. [23] and illustrated in Figure 3.9 is adopted:

$$\sigma(w) = \tilde{\omega} k_0 w, \tag{3.62}$$

where:

$$k_0 = 599.96 f_c^{0.75}/\phi, \tag{3.63}$$

$$\tilde{\omega} = \left[1.5\left(a + \sqrt{d^2 \left(40 w\phi - b\right)^2 + c^2}\right)\right]^{-4/3}, \tag{3.64}$$

$$a = 0.59 - 0.0110 f_c, \tag{3.65}$$

$$b = 0.0075 f_c - 0.23, \tag{3.66}$$

$$c = 0.0038 f_c + 0.44, \tag{3.67}$$

$$d = 0.0025 f_c + 0.58, \tag{3.68}$$

being f_c the concrete compressive strength and ϕ, the diameter of the bar.

The presence of the stirrups has a great influence on the dowel strength and, therefore, a proper modelling of these and of their interaction with the main bars is required. This will be discussed in the next chapter.

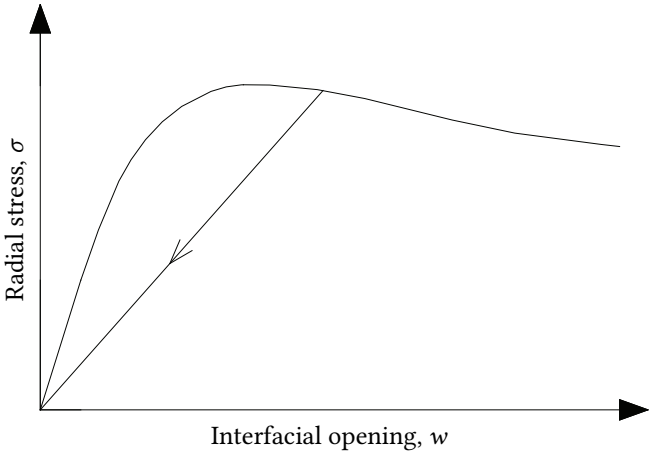

Figure 3.9.: Radial stress-opening relationship.

Equation 3.62 can also be used in the case that the opening w becomes negative. Further information is provided in Section 4.3.

4. Extended Finite Element Method

The spacial discretisation of the governing equations stated in Section 3.1.1 is carried out by means of the eXtended Finite Element Method (X-FEM). This method is able to model discontinuities within the structure independent of the finite element mesh, by enhancing the solution space of the standard finite element method with discontinuous functions using the partition of unity method. A good overview of this method is given in [17, 36, 50, 86, 98, 115].

The chapter is arranged as follows. First, a basic description of X-FEM is presented. Then, enrichment functions for the modelling of cracks are reviewed: near-tip enrichment and discontinuous (step) enrichment. These enrichments allow the modelling of the crack within an element independently of the underlying mesh. Next, a general X-FEM approach for the modelling of multiple cohesive cracks is proposed, followed by the discretisation of the weak form and its linearisation. In this regard, a junction enrichment is introduced in order to model the junction of cracks. The approximate fields are presented in a matrix representation at an element level. Further, a HEAVISIDE enrichment is proposed in order to model embedded reinforcing bars, transverse reinforcement, externally bonded reinforcement and fibres. Then, the numerical implementation of the bond model is described. For a better understanding of the proposed formulation, an example regarding a cracked body is presented in order to illustrate the enrichment strategy and the evaluation of the approximate fields. The numerical aspects that must be considered in the numerical implementation of the method are treated next. These aspects cover the numerical integration scheme regarding domain and line integrals, the appropriate node selection for enrichment, the modelling of the crack tip for kinked cracks and the numerical evaluation of the nonlocal stress. Finally, the key steps for the simulation of fracture in reinforced concrete structures within the framework of the proposed extended finite element formulation are described.

4.1. Extended finite element discretisation

The main idea behind X-FEM is to enrich the classical finite element approximations with additional information about the solution, in order to capture its local features. The enrichment takes advantage of the partition of unity property of finite element shape functions, allowing local previously-known functions to be easily incorporated into the classical approximation. The enrichment functions must be able to represent the local behaviour of the solution and, consequently, they will be different depending on the problem under consideration. The extended finite element approximation for a point $\boldsymbol{x}$ can be written in a general form as follows:

$$\boldsymbol{u}(\boldsymbol{x}) = \sum_{i \in I} \boldsymbol{u}_i N_i(\boldsymbol{x}) + \sum_{i \in I_{\mathcal{H}}} \boldsymbol{a}_i \left(\mathcal{H}(\boldsymbol{x}) - \mathcal{H}(\boldsymbol{x}_i)\right) N_i(\boldsymbol{x}), \tag{4.1}$$

$$\boldsymbol{u}(\boldsymbol{x}) = \sum_{i \in I} \boldsymbol{u}_i N_i(\boldsymbol{x}) + \sum_{j} \sum_{i \in I_{\mathcal{H}_j}} \boldsymbol{a}_i \left(\mathcal{H}_j(\boldsymbol{x}) - \mathcal{H}_j(\boldsymbol{x}_i)\right) N_i(\boldsymbol{x}), \tag{4.2}$$

where I is the set of all nodes of the system and $I_{\mathcal{H}}$, the set of nodes which are going to be enriched with the enrichment function (or functions) $\mathcal{H}(\boldsymbol{x})$. The values $\boldsymbol{u}_i$ are the standard degrees of freedom at node i, while $\boldsymbol{a}_i$, the additional degrees of freedom at node i that adjust the enrichment so that they can approximate the function $\mathcal{H}(\boldsymbol{x})$. The values $N_i(\boldsymbol{x})$ are the shape functions associated with node i. In this work, polynomial interpolation functions are used as shape functions. The first part of the right-hand side of Equation 4.1 represents the traditional approximation of the finite element method, while the second part is the enriched approximation.

Note that the shifted formulation developed by ZI et al. [130] is used, within which the enrichment functions are shifted by the factor $\mathcal{H}(\boldsymbol{x}_i)$, being $\boldsymbol{x}_i$ the coordinates of node i. This implies that the enrichment vanishes at each node i and, therefore, the standard degrees of freedom $\boldsymbol{u}_i$ can be identified directly with the displacements at the node. This formulation simplifies the implementation because only those elements that are crossed by the discontinuity need to be enriched.

4.1.1. Enrichment functions

Within the framework of the fracture mechanics, the fact that the displacement field is discontinuous along the crack and that the asymptotic behaviour of the solution near the crack tip is known, can be incorporated into the finite element approximation. The discontinuity across the crack is treated using a discontinuous function, while the asymptotic behaviour is incorporated by means of near-tip functions. Thus, allowing the crack geometry to be independent of the finite element mesh.

4.1.1.1. Near-tip enrichment

In order to consider the presence of the crack, BELYTSCHKO et al. [14] proposed to enrich the finite element approximation of the elements near the crack tip with functions that can represent the discontinuity introduced by it. The same span of functions developed in [49] for the enrichment of the element-free GALERKIN method was used, which correspond to the leading terms of the asymptotic displacement field at the crack tip:

$$F_i(\boldsymbol{x}) = F_i(r(\boldsymbol{x}), \theta(\boldsymbol{x})) = \left\{ \sqrt{r} \sin \frac{\theta}{2}, \sqrt{r} \cos \frac{\theta}{2}, \sqrt{r} \sin \frac{\theta}{2} \sin \theta, \sqrt{r} \cos \frac{\theta}{2} \sin \theta \right\}, \tag{4.3}$$

where $r(\boldsymbol{x})$ and $\theta(\boldsymbol{x})$ are the local polar coordinates with pole at the crack tip and polar axis tangent to the crack as shown in Figure 4.1.

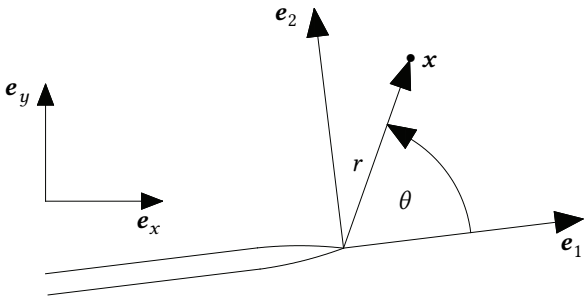

Figure 4.1.: Local polar coordinates with pole at the crack tip.

The functions are schematically illustrated in Figure 4.2. Note that the first term is discontinuous along the crack, allowing the crack tip to be modelled inside the element.

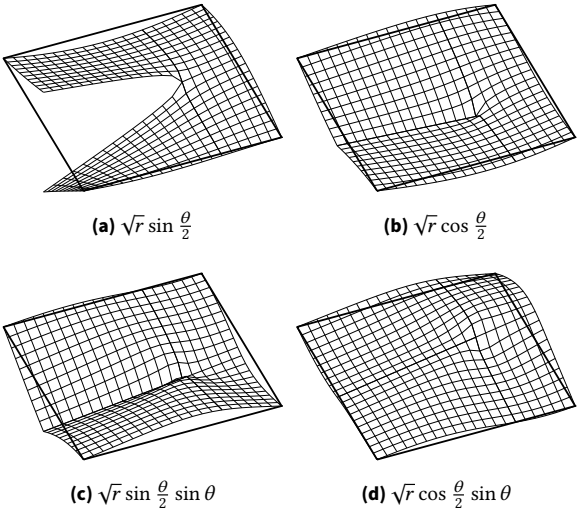

(a) $\sqrt{r}\sin\frac{\theta}{2}$ **(b)** $\sqrt{r}\cos\frac{\theta}{2}$

(c) $\sqrt{r}\sin\frac{\theta}{2}\sin\theta$ **(d)** $\sqrt{r}\cos\frac{\theta}{2}\sin\theta$

Figure 4.2.: Singular near-tip functions.

This approach allowed the crack to be partially independent of the mesh, since remeshing was still needed away from the crack tip.

Although the method was originally conceived to model cracks within the framework of the linear elastic fracture mechanics, an extension to non-linear materials is possible. Since the character of the near-tip field is represented by the enrichment, a non-linear behaviour can be modelled by simply modifying the near-tip functions exposed above.

For cohesive crack models, the singularity vanishes at the crack tip and the stress field no longer exhibits an asymptotic behaviour. Therefore, near-tip functions without a singularity are required. In [84], the following non-singular function was considered:

$$F(\boldsymbol{x}) = F(r(\boldsymbol{x}), \theta(\boldsymbol{x})) = rsin\frac{\theta}{2}. \tag{4.4}$$

By using a linear approach in the axial coordinate, the singularity is avoided in the near-tip stress field. Similar branch functions have been used in [41], where the square roots of the functions 4.3 where removed. Alternative near-tip functions were also proposed in [36, 38].

Figure 4.3 shows schematically the non-singular function defined in 4.4.

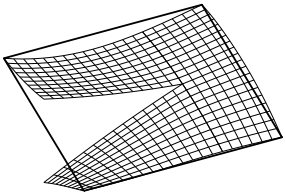

Figure 4.3.: Non-singular near-tip function.

4.1.1.2. Discontinuous enrichment

The enrichment presented by BELYTSCHKO et al. is insufficient when it comes to model long or curved cracks. This motivated MOËS [85] to propose an improvement in the enrichment technique by including a discontinuous function in the finite element approximation for those nodes away from the crack tip whose support is cut by the crack. The discontinuity is treated then using the step function $S(\boldsymbol{x})$, which takes the value 1 on one side of the crack and 0 on the other:

$$S(\boldsymbol{x}) = \begin{cases} +1 & \text{if} \quad \boldsymbol{x} \in \Omega^{+}, \\ -1 & \text{if} \quad \boldsymbol{x} \in \Omega^{-}. \end{cases} \tag{4.5}$$

Figure 4.4 schematically illustrates the discontinuity introduced by the step function in a finite element.

It must be noted that any discontinuous function along the crack can be used as a discontinuous enrichment function. Moreover, it is worth mentioning that the entire crack can be successfully modelled using only discontinuous functions, with the crack tip being at the element edges, as in [28, 56, 107, 122, 125]. However, for crack growth simulations, this has the disadvantage that cracks must be necessarily propagated from the border of an element to another, reducing in many cases the smoothness of the approximation.

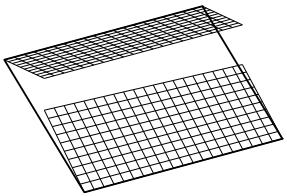

Figure 4.4.: Step function.

4.1.2. Enriched displacement approximation

The domain Ω is partitioned (or discretised) into N_e non-overlapping finite elements Ω^e, so that $\Omega = \cup_{e=1}^{N_e} \Omega^e$. In this work, standard isoparametric elements are considered. All N_n nodes of the system are collected into the set I. Thereafter, strong discontinuities (cracks) Γ_c^j are introduced. The geometry and location of the N_c cracks, as well as the positions of their tip, are fixed once they are initiated in an element. An accurate description of the crack positions in the domain is needed in order to enrich the approximation space properly. In [14, 31, 85, 117], cracks have been parametrised explicitly by a set of connected straight-lines. A second possibility is the use of level set methods [93]. Within this approach, the crack is defined implicitly as the zero level set of the signed distance function. The level-set method has been proved to be an ideal complement to X-FEM, since it was applied for the first time in [113]. In this work, the former approach is used, i.e. the crack is represented by the union of straight-line segments as shown in Figure 4.5. As the crack grows, new straight segments are added.

The nodes whose support contains the crack tip of the j-th crack are enriched with the near-tip function $F^j(\boldsymbol{x})$, thus forming the set of nodes I_F^j. The nodes whose support is cut by the crack j into two disjoint pieces and do not belong to I_F^j are enriched with the step function $S^j(\boldsymbol{x})$, thus forming the set of nodes I_S^j. Formally, these sets can be defined as:

$$I_F^j = \left\{ i \in I \ : \ \boldsymbol{x}_t^j \in \varpi^i \right\}, \tag{4.6}$$

$$I_S^j = \left\{ i \in I \ : \ e^i \cap \Gamma_d^j \neq \ \wedge \boldsymbol{x}_t^j \notin \varpi^i \right\}, \tag{4.7}$$

where $\boldsymbol{x}_t^j$ denotes the location of the crack tip of the j-th crack and ϖ^i, the support of the node i. Figure 4.5 illustrates the enrichment strategy.

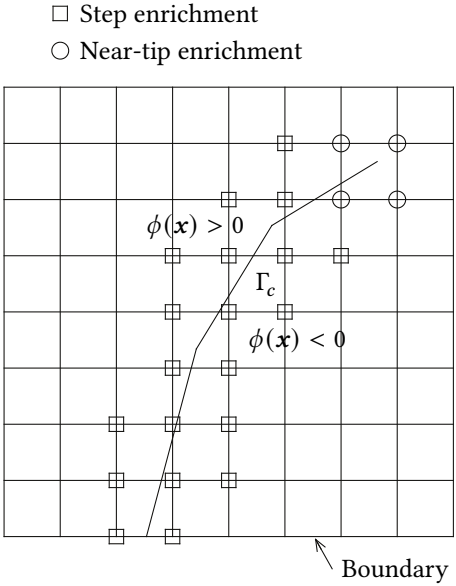

Figure 4.5.: Enrichment strategy.

As can be seen, the enrichment for each crack is local, it does not extend beyond the elements that enclose the crack.

Then, the X-FEM approximation of the displacement field for multiple crack growth leads to:

$$\boldsymbol{u}(\boldsymbol{x}) = \sum_{i \in I} N_i(\boldsymbol{x}) \boldsymbol{u}_i + \sum_{j=1}^{N_c} \sum_{i \in I_S^j} N_i(\boldsymbol{x}) \tilde{S}_i^j(\boldsymbol{x}) \boldsymbol{b}_i^j + \sum_{j=1}^{N_c} \sum_{i \in I_F^j} N_i(\boldsymbol{x}) \tilde{F}_i^j(\boldsymbol{x}) \boldsymbol{c}_i^j, \quad (4.8)$$

where $\boldsymbol{b}_i^j$ are the additional degrees of freedom at node i associated with the step function, while $\boldsymbol{c}_i^j$, the additional degrees of freedom at node i associated

with the near-tip function. The modified enrichment functions $\tilde{S}_i^j(\boldsymbol{x})$ and $\tilde{F}_i^j(\boldsymbol{x})$ are given by:

$$\tilde{S}_i^j(\boldsymbol{x}) = S(\phi^j(\boldsymbol{x})) - S(\phi^j(\boldsymbol{x}_i)), \tag{4.9}$$

$$\tilde{F}_i^j(\boldsymbol{x}) = F^j(\boldsymbol{x}) - F^j(\boldsymbol{x}_i), \tag{4.10}$$

being $\phi^j(\boldsymbol{x})$ the signed distance function related to the crack surface Γ_c^j. The non-singular function defined in Equation 4.4 is used as near-tip function.

Considering the approximation of the displacement field, the strain field can be discretised as follows:

$$\begin{aligned}\boldsymbol{\epsilon}(\boldsymbol{x}) = &\sum_{i\in I}\left[\boldsymbol{u}_i \otimes \nabla N_i(\boldsymbol{x})\right]^{sym} + \sum_{j=1}^{N_c}\sum_{i\in I_S^j}\left[\boldsymbol{b}_i^j \otimes \nabla\left(N_i(\boldsymbol{x})\tilde{S}_i^j(\boldsymbol{x})\right)\right]^{sym} \\ &+ \sum_{j=1}^{N_c}\sum_{i\in I_F^j}\left[\boldsymbol{c}_i^j \otimes \nabla\left(N_i(\boldsymbol{x})\tilde{F}_i^{j,k}(\boldsymbol{x})\right)\right]^{sym}.\end{aligned} \tag{4.11}$$

Using the definition given in Equation 3.4 and the displacement field approximation 4.8, the relative displacement field across the crack j can be written as:

$$\boldsymbol{\omega}^j(\boldsymbol{x}) = 2\sum_{i\in I_S^j} N_i(\boldsymbol{x})\boldsymbol{b}_i^j + 2\sum_{i\in I_F^{j,k}} N_i(\boldsymbol{x})r^j(\boldsymbol{x})\boldsymbol{c}_i^j, \quad \boldsymbol{x}\in\Gamma_c^j. \tag{4.12}$$

4.1.2.1. Matrix notation

Due to the compatibility with the finite element formulation, matrix notation[1] is more convenient than tensor notation in the numerical implementation of the finite element method. This notation allows for a matrix representation of the HOOKE's law, within which the stress and strain tensors are written as vectors and the stiffness tensor, as a matrix. Therefore, the discretisation exposed above will be reformulated in a matrix form for a point $\boldsymbol{x}$ within a finite element e. For this purpose, it is necessary to define, firstly,

[1] Also known as vector notation or VOIGT notation.

the set of nodes belonging to the element e, denoted by I_e, and, secondly, the set of cracks related to the element e, i.e. the cracks that intersect the support of the nodes of the element e, denoted by $\mathcal{N}_c^e$. From now on, this notation will be used to expose the developed finite element formulation.

Then, the approximation 4.8 can be expressed within a finite element in matrix form as:

$$\boldsymbol{u}(\boldsymbol{x}) = \boldsymbol{G}(\boldsymbol{x})\boldsymbol{q}, \quad \boldsymbol{x} \in \Omega_e, \tag{4.13}$$

where $\boldsymbol{G}(\boldsymbol{x})$ is the generalised shape functions matrix and is defined as:

$$\boldsymbol{G} = \left[\boldsymbol{N} \cdots \boldsymbol{G}_S^j \cdots \boldsymbol{G}_F^j \cdots\right], \quad \forall j \in \mathcal{N}_c^e. \tag{4.14}$$

The matrix $\boldsymbol{N}(\boldsymbol{x})$ is the standard shape functions matrix and groups the shape functions corresponding to all nodes of the element e:

$$\boldsymbol{N} = \left[\begin{bmatrix} N_i & 0 \\ 0 & N_i \end{bmatrix} \cdots\right], \quad \forall i \in I_e. \tag{4.15}$$

The matrices $\boldsymbol{G}_S^j(\boldsymbol{x})$ and $\boldsymbol{G}_F^j(\boldsymbol{x})$ contain the enriched shape functions matrices associated with the crack j of those nodes of the element that are enriched with the step and near-tip function, respectively. These can be written as:

$$\boldsymbol{G}_S^j = \left[\tilde{S}_i^j \begin{bmatrix} N_i & 0 \\ 0 & N_i \end{bmatrix} \cdots\right], \quad \forall i \in I_S^j \cap I_e, \tag{4.16}$$

$$\boldsymbol{G}_F^j = \left[\tilde{F}_i^j \begin{bmatrix} N_i & 0 \\ 0 & N_i \end{bmatrix} \cdots\right], \quad \forall i \in I_F^j \cap I_e. \tag{4.17}$$

Note that the presence of $\boldsymbol{G}_S^j$ and $\boldsymbol{G}_F^j$ depends on the enrichment associated to the nodes of the element under consideration.

The generalised nodal displacements vector $\boldsymbol{q}$ groups all degrees of freedom of the element and is defined as:

$$\boldsymbol{q} = \left[\bar{\boldsymbol{u}}^T \cdots \boldsymbol{b}^{jT} \cdots \boldsymbol{c}^{jT} \cdots\right]^T, \quad \forall j \in \mathcal{N}_c^e, \tag{4.18}$$

where $\bar{\boldsymbol{u}}$ is a vector that groups the standard degrees of freedom, while $\boldsymbol{b}^j$ and $\boldsymbol{c}^j$ are vectors that group the additional degrees of freedom associated with the crack j for the step and the near-tip enrichment, respectively:

$$\bar{\boldsymbol{u}} = \left[\boldsymbol{u}_i^T \cdots\right]^T, \quad \forall i \in I_e, \tag{4.19}$$

$$\boldsymbol{b}^j = \left[\boldsymbol{b}_i^{jT} \cdots\right]^T, \quad \forall i \in I_S^j \cap I_e, \tag{4.20}$$

$$\boldsymbol{c}^j = \left[\boldsymbol{c}_i^{jT} \cdots\right]^T, \quad \forall i \in I_F^j \cap I_e. \tag{4.21}$$

The relative displacement field reads:

$$\boldsymbol{\omega}^j(\boldsymbol{x}) = \boldsymbol{\mathcal{N}}^j(\boldsymbol{x})\boldsymbol{a}^j, \quad \boldsymbol{x} \in \Gamma_c^j, \tag{4.22}$$

with:

$$\boldsymbol{\mathcal{N}}^j = \left[\cdots \boldsymbol{\mathcal{N}}_S^j \cdots \boldsymbol{\mathcal{N}}_F^j \cdots\right]. \tag{4.23}$$

Matrices $\boldsymbol{\mathcal{N}}_S^j(\boldsymbol{x})$ and $\boldsymbol{\mathcal{N}}_F^j(\boldsymbol{x})$ are defined as follows:

$$\boldsymbol{\mathcal{N}}_S^j = \left[2\begin{bmatrix} N_i & 0 \\ 0 & N_i \end{bmatrix} \cdots\right], \quad \forall i \in I_S^j \cap I_e, \tag{4.24}$$

$$\boldsymbol{\mathcal{N}}_F^j = \left[2r^j\begin{bmatrix} N_i & 0 \\ 0 & N_i \end{bmatrix} \cdots\right], \quad \forall i \in I_F^j \cap I_e. \tag{4.25}$$

The vector $\boldsymbol{a}^j$ groups the additional degrees of freedom of the element associated with the crack j:

$$\boldsymbol{a}^j = \left[\cdots \boldsymbol{b}^{jT} \cdots \boldsymbol{c}^{jT} \cdots\right]^T. \tag{4.26}$$

Defining the compatibility matrix:

$$\boldsymbol{B} = \left[\boldsymbol{B}_N \cdots \boldsymbol{B}_S^j \cdots \boldsymbol{B}_F^j \cdots\right], \quad \forall j \in \mathcal{N}_c^e, \tag{4.27}$$

the strain field $\boldsymbol{\epsilon}(\boldsymbol{x})$ can also be represented in matrix notation within an element:

$$\boldsymbol{\epsilon}(\boldsymbol{x}) = \boldsymbol{B}(\boldsymbol{x})\boldsymbol{q}, \quad \boldsymbol{x} \in \Omega_e. \tag{4.28}$$

The matrices $\boldsymbol{B}_N(\boldsymbol{x})$, $\boldsymbol{B}_S^j(\boldsymbol{x})$ and $\boldsymbol{B}_F^j(\boldsymbol{x})$ contain the derivatives of the shape functions matrices and are given by:

$$\boldsymbol{B}_N = \begin{bmatrix} \begin{bmatrix} \frac{\partial N_i}{\partial x} & 0 \\ 0 & \frac{\partial N_i}{\partial y} \\ \frac{\partial N_i}{\partial y} & \frac{\partial N_i}{\partial x} \end{bmatrix} \cdots \end{bmatrix}, \quad \forall i \in I_e, \tag{4.29}$$

$$\boldsymbol{B}_S^j = \begin{bmatrix} \tilde{S}_i^j \begin{bmatrix} \frac{\partial N_i}{\partial x} & 0 \\ 0 & \frac{\partial N_i}{\partial y} \\ \frac{\partial N_i}{\partial y} & \frac{\partial N_i}{\partial x} \end{bmatrix} \cdots \end{bmatrix}, \quad \forall i \in I_S^j \cap I_e, \tag{4.30}$$

$$\boldsymbol{B}_F^j = \begin{bmatrix} \begin{bmatrix} \partial_x(\tilde{F}_i^j N_i) & 0 \\ 0 & \partial_y(\tilde{F}_i^j N_i) \\ \partial_y(\tilde{F}_i^j N_i) & \partial_x(\tilde{F}_i^j N_i) \end{bmatrix} \cdots \end{bmatrix}, \quad \forall i \in I_F^j \cap I_e. \tag{4.31}$$

The functions $\partial_x(\tilde{F}_i^j(\boldsymbol{x})N_i(\boldsymbol{x}))$ and $\partial_y(\tilde{F}_i^j(\boldsymbol{x})N_i(\boldsymbol{x}))$ are defined as follows:

$$\partial_x(\tilde{F}_i^j N_i) = \frac{\partial F_i^j}{\partial x} N_i + \tilde{F}_i^j \frac{\partial N_i}{\partial x} \tag{4.32}$$

$$\partial_y(\tilde{F}_i^j N_i) = \frac{\partial F_i^j}{\partial y} N_i + \tilde{F}_i^j \frac{\partial N_i}{\partial y}. \tag{4.33}$$

Finally, the matrix form of the damaged constitutive law 3.38 is:

$$\boldsymbol{\sigma}(\boldsymbol{x}) = (1 - D(\tilde{\epsilon}))\boldsymbol{C}\boldsymbol{\epsilon}(\boldsymbol{x}), \tag{4.34}$$

where $\boldsymbol{C}$ is the matrix representation of the fourth order stiffness tensor $\mathbb{C}$.

Likewise, the effective stress field can be represented as:

$$\bar{\boldsymbol{\sigma}}(\boldsymbol{x}) = \boldsymbol{C}\boldsymbol{\epsilon}(\boldsymbol{x}). \tag{4.35}$$

Furthermore, the equivalent strain defined in Equation 3.43 is expressed in terms of the matrix form of the strain tensor as:

$$\tilde{\epsilon} = \frac{\epsilon_x + \epsilon_y}{2} - \sqrt{\left(\frac{\epsilon_x - \epsilon_y}{2}\right)^2 + \left(\frac{\gamma_{xy}}{2}\right)^2}. \tag{4.36}$$

The virtual displacement field $\delta\boldsymbol{u}(\boldsymbol{x})$, the virtual relative displacement field $\delta\boldsymbol{\omega}(\boldsymbol{x})$, and the virtual strain field $\delta\boldsymbol{\epsilon}(\boldsymbol{x})$ are approximated in a similar fashion.

4.1.3. Discrete equilibrium equation

Replacing the X-FEM approximations 4.13, 4.22, 4.28 and 4.34 in the expressions of the virtual works given in Equations 3.13-3.15, yields:

$$\delta W^{int} = \delta\boldsymbol{Q} \prod_{e=1}^{N_e} \left(\int_{\Omega_e} h\boldsymbol{B}^T \boldsymbol{\sigma}\, dA \right), \tag{4.37}$$

$$\delta W^{ext} = \delta\boldsymbol{Q} \prod_{e=1}^{N_e} \left(\int_{\Gamma_{t,e}} h\boldsymbol{N}^T \boldsymbol{t}^*\, dl \right), \tag{4.38}$$

$$\delta W^{coh} = \delta\boldsymbol{Q} \sum_{j=1}^{N_c} \prod_{e=1}^{N_e} \left(\int_{\Gamma_{c,e}^j} h\boldsymbol{N}^{j\,T} \boldsymbol{t}^j\, dl \right), \tag{4.39}$$

where $\prod_{e=1}^{N_e}$ represents the standard assembly operators over all the N_e finite elemets. Vector $\boldsymbol{Q}$ groups all degrees of freedom of the system.

In order to facilitate the numerical implementation of the finite element model, it is convenient to rewrite the virtual work of the internal forces 4.37 in terms of the effective stress field, thus obtaining:

$$\delta W^{int} = \delta\boldsymbol{Q} \prod_{e=1}^{N_e} \left(\int_{\Omega_e} h\boldsymbol{B}^T \boldsymbol{C}\boldsymbol{B}\, dA \right) \boldsymbol{Q} - \delta\boldsymbol{Q} \prod_{e=1}^{N_e} \left(\int_{\Omega_e} h\boldsymbol{B}^T D\bar{\boldsymbol{\sigma}}\, dA \right). \tag{4.40}$$

In this way, the non-linear terms of the constitutive model are isolated and can be more easily processed.

As the virtual displacements $\delta \boldsymbol{Q}$ are arbitrary, Equation 3.16 is reduced finally to the discrete equilibrium equation:

$$\boldsymbol{K}\boldsymbol{Q} + \boldsymbol{F}^{D} + \boldsymbol{F}^{coh} = \boldsymbol{F}^{ext}, \tag{4.41}$$

where $\boldsymbol{K}$ is the stiffness matrix, $\boldsymbol{F}^{coh}$, the cohesive force vector and $\boldsymbol{F}^{ext}$, the external force vector. These are defined as:

$$\boldsymbol{K} = \prod_{e=1}^{N_e} \left(\int_{\Omega_e} h \boldsymbol{B}^T \boldsymbol{C} \boldsymbol{B} \, dA \right), \tag{4.42}$$

$$\boldsymbol{F}^{coh} = \sum_{j=1}^{N_c} \prod_{e=1}^{N_e} \left(\int_{\Gamma_{c,e}^{j}} h \boldsymbol{N}^{j\,T} \boldsymbol{t}^{j} \, dl \right), \tag{4.43}$$

$$\boldsymbol{F}^{ext} = \prod_{e=1}^{N_e} \left(\int_{\Gamma_{t,e}} h \boldsymbol{N}^T \boldsymbol{t}^{*} \, dl \right). \tag{4.44}$$

The vector $\boldsymbol{F}^{D}$, associated with the second part of the right-hand of Equation 4.40 (the non-linear part), is denoted as damage force vector and is defined as follows:

$$\boldsymbol{F}^{D} = \prod_{e=1}^{N_e} \left(\int_{\Omega_e} -h \boldsymbol{B}^T D \bar{\boldsymbol{\sigma}} \, dA \right). \tag{4.45}$$

Since the cohesive tractions are defined in the local coordinate system (Equations 3.24 and 3.30), it is convenient to express the cohesive force vector as follows:

$$\boldsymbol{F}^{coh} = \sum_{j=1}^{N_c} \prod_{e=1}^{N_e} \left(\int_{\Gamma_{c,e}^{j}} h \boldsymbol{N}^{j\,T} \boldsymbol{R}^{j} \boldsymbol{\mathcal{T}}^{j}(\boldsymbol{\Omega}^{j}) \, dl \right). \tag{4.46}$$

Furthermore, for the evaluation of the local cohesive tractions t_n and t_s, the local relative displacement vector is needed:

$$\boldsymbol{\Omega} = \boldsymbol{R}^T \boldsymbol{\omega}. \tag{4.47}$$

Reinforcing bars will be treated later in this chapter.

4.1.3.1. Linearisation

Due to the dependence of the damage and cohesive force vector on the generalised nodal displacements, the discretisation performed above leads to a non-linear problem. Therefore, the equilibrium equation of the system must be solved through an incremental iterative procedure. The aim is to find a $\boldsymbol{Q}$ that minimises the residual (or out-of-balance force) vector:

$$\boldsymbol{Re}(\boldsymbol{Q}) = \boldsymbol{K}\boldsymbol{Q} + \boldsymbol{F}^{D}(\boldsymbol{Q}) + \boldsymbol{F}^{coh}(\boldsymbol{Q}) - \boldsymbol{F}^{ext}. \tag{4.48}$$

The external forces are considered to be independent of the displacements.

In this work, the zeros of the residual vector $\boldsymbol{Re}(\boldsymbol{Q})$ are determined by means of the NEWTON-RAPHSON iteration scheme. This method requires a linear expansion of the residual vector in the form:

$$L\boldsymbol{Re}(\boldsymbol{Q}_{n+1}) := \boldsymbol{Re}(\boldsymbol{Q}_n) + \left.\frac{\partial \boldsymbol{Re}(\boldsymbol{Q})}{\partial \boldsymbol{Q}}\right|_{\boldsymbol{Q}_n} \Delta\boldsymbol{Q}_{n+1} = 0, \tag{4.49}$$

with $\Delta\boldsymbol{Q}_{n+1} = \boldsymbol{Q}_{n+1} - \boldsymbol{Q}_n$;

thus obtaining the following incremental discrete equilibrium equation:

$$\boldsymbol{\mathcal{K}}_n \Delta\boldsymbol{Q}_{n+1} = -\boldsymbol{Re}(\boldsymbol{Q}_n). \tag{4.50}$$

Subscript n refers to the current equilibrium iteration. The global stiffness matrix $\boldsymbol{\mathcal{K}}$ is given by:

$$\boldsymbol{\mathcal{K}} = \boldsymbol{K} + \boldsymbol{K}^{D} + \boldsymbol{K}^{coh}. \tag{4.51}$$

Herein, $\boldsymbol{K}^{coh}$ represents the tangent matrix associated with the cohesive force vector:

$$\boldsymbol{K}^{coh} = \frac{\partial \boldsymbol{F}^{coh}}{\partial \boldsymbol{Q}} = \sum_{j=1}^{N_c} \prod_{e=1}^{N_e} \left(\int_{\Gamma_{c,e}^{j}} h \boldsymbol{\mathcal{N}}^{j\,T} \boldsymbol{R}^{j} \frac{\partial \boldsymbol{\mathcal{T}}^{j}}{\partial \boldsymbol{\Omega}^{j}} \boldsymbol{R}^{j\,T} \boldsymbol{\mathcal{N}}^{j}\, dl \right), \tag{4.52}$$

where $\partial\boldsymbol{\mathcal{T}}/\partial\boldsymbol{\Omega}$ is the tangent stiffness matrix of the traction law:

$$\frac{\partial \boldsymbol{\mathcal{T}}}{\partial \boldsymbol{\Omega}} = \begin{bmatrix} \frac{\partial t_n}{\partial \omega_n} & \frac{\partial t_n}{\partial \omega_s} \\ \frac{\partial t_s}{\partial \omega_n} & \frac{\partial t_s}{\partial \omega_s} \end{bmatrix}. \tag{4.53}$$

$\boldsymbol{K}^D$ corresponds to the tangent matrix associated to the damage force vector and is determined from:

$$\boldsymbol{K}^D = \prod_{e=1}^{N_e} \left(\int_{\Omega_e} -h\boldsymbol{B}^T \boldsymbol{C}^{ed} \boldsymbol{B}\, dA \right). \tag{4.54}$$

Introducing the symbols D' for the derivative $dD/d\tilde{\epsilon}$ of the damage variable, and $\boldsymbol{\eta}$ for the vector $\partial\tilde{\epsilon}/\partial\boldsymbol{\epsilon}$ obtained by differentiation of the expression for the equivalent strain with respect to the strain field, the elasto-damage stiffness matrix $\boldsymbol{C}^{ed}$ can be computed from:

$$\boldsymbol{C}^{ed} = D\boldsymbol{C} + D'\bar{\boldsymbol{\sigma}} \otimes \boldsymbol{\eta}. \tag{4.55}$$

Considering the damage model stated in Section 3.3, the derivative D' takes the following form for loading conditions ($f \geq 0$):

$$D' = \frac{dD}{d\tilde{\epsilon}} = \frac{dD}{dE_s}\frac{dE_s}{d\tilde{\epsilon}} = \frac{dD}{dE_s}\left(\frac{d\sigma_c}{d\tilde{\epsilon}}\frac{1}{\tilde{\epsilon}} - \frac{\sigma_c}{\tilde{\epsilon}^2}\right) = -\frac{1}{E}\left(\frac{d\sigma_c}{d\tilde{\epsilon}}\frac{1}{\tilde{\epsilon}} - \frac{\sigma_c}{\tilde{\epsilon}^2}\right), \tag{4.56}$$

and is equal to 0 for unloading/reloading ($f < 0$).

The derivative $d\sigma_c/d\tilde{\epsilon}$ is given by:

$$\frac{d\sigma_c}{d\tilde{\epsilon}} = \begin{cases} -f_c\left[0.2/\left(\epsilon_{c_2} - \epsilon_{c_1}\right)\right] & \text{if} \quad \epsilon_{c_1} > \tilde{\epsilon} \geq \epsilon_{c_2}, \\ -f_c\left[1-\eta\right]\left[k + \left(k-2\right)\eta\right]/\left[1 + \left(k-2\right)\eta\right]^2 & \text{if} \quad \epsilon_{c_2} > \tilde{\epsilon} \geq \epsilon_{c_3}, \\ 0 & \text{if} \quad \tilde{\epsilon} < \epsilon_{c_3}. \end{cases} \tag{4.57}$$

The generalised nodal displacements $\boldsymbol{Q}$ are then updated in each iteration step:

$$\boldsymbol{Q}_{n+1} = \boldsymbol{Q}_n + \Delta\boldsymbol{Q}_{n+1}. \tag{4.58}$$

Using the updated displacements $\boldsymbol{Q}_{n+1}$, the residual vector $\boldsymbol{Re}(\boldsymbol{Q}_{n+1})$ is calculated again to check whether the convergence criterion is fulfilled. If not, additional iterations are performed until the final solution converges. The convergence criterion reads:

$$\frac{\left\|\boldsymbol{Re}(\boldsymbol{Q}_{n+1})\right\|}{\left\|\boldsymbol{F}_n^{ext}\right\|} \leq \beta, \tag{4.59}$$

where β is the convergence tolerance. The norms are Euclidean.

For the iterative process, initial values for the displacements ($\boldsymbol{Q}_0$) are required. A natural choice is the use of the displacement field obtained in the last loading step (on the first last step, $\boldsymbol{Q}_0 = \boldsymbol{0}$). However, for crack growth simulations, the enrichment changes as the crack propagates and, therefore, the degrees of freedom are no longer matched with each other. To overcome this, the mapping procedure (Mapping Scheme) presented in [50] is used. Within this approach, the displacements from the last loading step, which are associated with the old enrichment, are mapped into the new enrichment configuration. The mapping is achieved by minimising the error given by:

$$e = \int_{\Omega} \left(\boldsymbol{Q}_n^{old} - \boldsymbol{Q}_n^{new} \right) \cdot \left(\boldsymbol{Q}_n^{old} - \boldsymbol{Q}_n^{new} \right) dA. \tag{4.60}$$

being $\boldsymbol{Q}_n^{old}$ and $\boldsymbol{Q}_n^{new}$ the displacements associated with the old and new enrichment, respectively.

The previous equation leads to:

$$\boldsymbol{A}_n^{new} \boldsymbol{Q}_n^{new} = \boldsymbol{A}_n^{old} \boldsymbol{Q}_n^{old}, \tag{4.61}$$

where:

$$\boldsymbol{A}_n^{new} = \prod_{e=1}^{N_e} \left(\int_{\Omega_e} \left(\boldsymbol{G}^{new} \right)^T \boldsymbol{G}^{new} \, dA \right), \tag{4.62}$$

$$\boldsymbol{A}_n^{old} = \prod_{e=1}^{N_e} \left(\int_{\Omega_e} \left(\boldsymbol{G}^{new} \right)^T \boldsymbol{G}^{old} \, dA \right). \tag{4.63}$$

The matrices $\boldsymbol{G}^{old}$ and $\boldsymbol{G}^{new}$ are the generalised shape functions matrices for the old and new enrichment configuration, respectively.

4.1.4. Junction of cracks

In multiple crack propagation, interaction between cracks may take place. In this regard, if a crack during its propagation overlaps with an existing crack, its propagation is simply arrested at the intersection point and both cracks

coalesce. This type of interaction was already studied by DAUX et al. [31] and BUDYN et al. [24] within the framework of X-FEM for brittle materials. In those works, the near-tip enrichment of the approaching crack (called secondary crack) is annihilated and replaced by the so-called junction enrichment, thus modelling the join inside the element; while the enrichment of the existing crack (called main crack) remains unchanged. The nodes whose support contains the junction point $\boldsymbol{x}_J$ are enriched in this way, forming the set of nodes I_J:

$$I_J = \left\{ i \in I \ : \ \boldsymbol{x}_J \in \varpi^i \right\}. \tag{4.64}$$

Figure 4.6 shows the enrichment strategy.

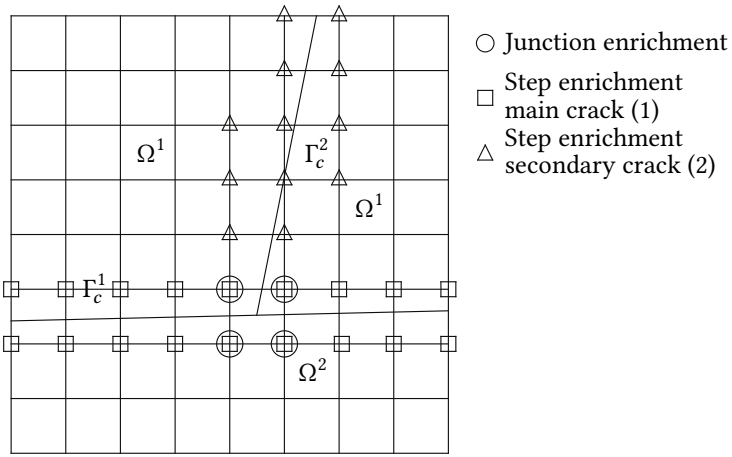

Figure 4.6.: Enrichment strategy for junction of cracks.

The crack junction is treated using the step enrichment developed by BUDYN et al. [24], which is defined as follows:

$$etal.\tilde{J}^{1-2}(\boldsymbol{x}) = \begin{cases} \tilde{S}^1(\boldsymbol{x}) & \text{if} \quad \boldsymbol{x} \in \Omega^2, \\ \tilde{S}^2(\boldsymbol{x}) & \text{if} \quad \boldsymbol{x} \in \Omega^1, \end{cases} \tag{4.65}$$

where $\tilde{S}^1(\boldsymbol{x})$ and $\tilde{S}^2(\boldsymbol{x})$ are the modified step functions associated with the main crack and the secondary crack, respectively. Ω^1 represents the side

of the main crack containing the secondary crack, while Ω^2 is simply the opposite side. Figure 4.7 schematically shows the function $\tilde{J}^{1-2}(\boldsymbol{x})$ inside an element.

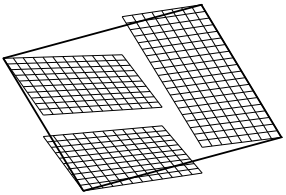

Figure 4.7.: Junction function.

Then, the displacement field approximation is given by:

$$\boldsymbol{u}(\boldsymbol{x}) = \sum_{i\in I} N_i(\boldsymbol{x})\boldsymbol{u}_i + \sum_{i\in I_S^1} N_i(\boldsymbol{x})\tilde{S}_i^1(\boldsymbol{x})\boldsymbol{b}_i^1 + \sum_{i\in I_S^2} N_i(\boldsymbol{x})\tilde{S}_i^2(\boldsymbol{x})\boldsymbol{b}_i^2 + \sum_{i\in I_J} N_i(\boldsymbol{x})\tilde{J}_i^{1-2}(\boldsymbol{x})\boldsymbol{d}_i, \tag{4.66}$$

where $\boldsymbol{d}_i$ are the additional degrees of freedom at node i associated with the junction enrichment.

For the calculation of the relative displacement field along the main crack, the orientation of the secondary crack with respect to the main crack needs to be considered. Then, defining $\hat{\boldsymbol{t}}_1$ as the unit tangent vector to the main crack and $\hat{\boldsymbol{t}}_2$ as the unit tangent vector to the secondary crack, both taken in the direction of propagation, the relative displacement field for the main crack can be written as:

$$\boldsymbol{\omega}^1(\boldsymbol{x}) = 2\sum_{i\in I_S^1} N_i(\boldsymbol{x})\boldsymbol{b}_i^1 + \sum_{i\in I_J} N_i(\boldsymbol{x})^- j_i^{1-2}(\boldsymbol{x})\boldsymbol{d}_i, \quad \boldsymbol{x}\in\Gamma_c^1, \tag{4.67}$$

when $\hat{\boldsymbol{t}}_1 \times \hat{\boldsymbol{t}}_2 < 0$; and as:

$$\boldsymbol{\omega}^1(\boldsymbol{x}) = 2\sum_{i\in I_S^1} N_i(\boldsymbol{x})\boldsymbol{b}_i^1 + \sum_{i\in I_J} N_i(\boldsymbol{x})^+ j_i^{1-2}(\boldsymbol{x})\boldsymbol{d}_i, \quad \boldsymbol{x}\in\Gamma_c^1, \tag{4.68}$$

when $\hat{\boldsymbol{t}}_1 \times \hat{\boldsymbol{t}}_2 > 0$.

The functions ${}^{-}j_i^{1-2}(\boldsymbol{x})$ and ${}^{+}j_i^{1-2}(\boldsymbol{x})$ are defined as follows:

$$ {}^{-}j_i^{1-2} = S^2(\boldsymbol{x}) - S^2(\boldsymbol{x}_i) + 1 + S^1(\boldsymbol{x}_i), \tag{4.69} $$

$$ {}^{+}j_i^{1-2} = 1 - S^1(\boldsymbol{x}_i) - S^2(\boldsymbol{x}) + S^2(\boldsymbol{x}_i). \tag{4.70} $$

For the secondary crack, the relative displacement field is given by:

$$ \boldsymbol{\omega}^2(\boldsymbol{x}) = 2 \sum_{i \in I_S^2} N_i(\boldsymbol{x}) \boldsymbol{b}_i^2 + 2 \sum_{i \in I_J} N_i(\boldsymbol{x}) \boldsymbol{d}_i, \quad \boldsymbol{x} \in \Gamma_c^2. \tag{4.71} $$

For the matrix representation of the discretised fields, the same expressions presented in the previous section are used. In this case, the generalised shape functions matrix $\boldsymbol{G}(\boldsymbol{x})$ and the generalised nodal displacements vector $\boldsymbol{q}(\boldsymbol{x})$, both involved in the definition of the matrix form of the displacement field 4.13, take the following form within an enriched finite element:

$$ \boldsymbol{G} = \left[\boldsymbol{N} \cdots \boldsymbol{G}_S^j \cdots \boldsymbol{G}_J \cdots \right], \tag{4.72} $$

$$ \boldsymbol{q} = \left[\bar{\boldsymbol{u}}^T \cdots \boldsymbol{b}^{jT} \cdots \boldsymbol{d}^T \cdots \right]^T, \quad j = 1, 2, \tag{4.73} $$

with:

$$ \boldsymbol{G}_J = \left[\tilde{J}_i^{1-2} \begin{bmatrix} N_i & 0 \\ 0 & N_i \end{bmatrix} \cdots \right], \tag{4.74} $$

$$ \boldsymbol{d} = \left[\boldsymbol{d}_i^T \cdots \right]^T, \quad \forall i \in I_J \cap I_e. \tag{4.75} $$

Likewise, the matrices involved in the Equation 4.22 can be computed from:

$$ \boldsymbol{\mathcal{N}}^j = \left[\cdots \boldsymbol{\mathcal{N}}_S^j \cdots \boldsymbol{\mathcal{N}}_J^j \cdots \right], \tag{4.76} $$

$$ \boldsymbol{a}^j = \left[\cdots \boldsymbol{b}^{jT} \cdots \boldsymbol{d}^T \cdots \right]^T. \tag{4.77} $$

where:

$$\boldsymbol{\mathcal{N}}_J^1 = \left[\mp j_i^{1-2} \begin{bmatrix} N_i & 0 \\ 0 & N_i \end{bmatrix} \cdots \right], \tag{4.78}$$

$$\boldsymbol{\mathcal{N}}_J^2 = \left[2 \begin{bmatrix} N_i & 0 \\ 0 & N_i \end{bmatrix} \cdots \right], \quad \forall i \in I_J \cap I_e. \tag{4.79}$$

Finally, the compatibility matrix $\boldsymbol{B}$ assumes the following expression in the definition 4.28:

$$\boldsymbol{B} = \left[\boldsymbol{B}_N \cdots \boldsymbol{B}_S^j \cdots \boldsymbol{B}_J \cdots \right], \quad j = 1, 2, \tag{4.80}$$

being:

$$\boldsymbol{B}_J = \left[\tilde{J}_i^{1-2} \begin{bmatrix} \frac{\partial N_i}{\partial x} & 0 \\ 0 & \frac{\partial N_i}{\partial y} \\ \frac{\partial N_i}{\partial y} & \frac{\partial N_i}{\partial x} \end{bmatrix} \cdots \right], \quad \forall i \in I_J \cap I_e. \tag{4.81}$$

The methodology exposed above can be easily extended to model multiple junction of cracks. Consider, for this purpose, the crack m (secondary crack) that coalesces with the existing crack j (main crack) during its propagation at the point $\boldsymbol{x}_J^{j-m}$ (junction point). Each annihilated near-tip enrichment is then replaced by the junction enrichment $\tilde{J}^{j-m}(\boldsymbol{x})$ (defined in Equation 4.65). Both cracks define an ordered pair $(j-m)$, which characterises the junction. The first entry corresponds to the main crack, while the second one, to the secondary crack.

The nodes of the element containing the junction point $\boldsymbol{x}_J^{j-m}$ are enriched with the function $\tilde{J}^{j-m}(\boldsymbol{x})$, thus forming the set of nodes I_J^{j-m}, where the additional degrees of freedoms at node i are denoted by $\boldsymbol{d}_i^{j-m}$. The ordered pairs $(j-m)$ related to the element e, i.e. the pairs whose corresponding junction points are located inside the nodal support of the element e, are

collected in the set $\mathcal{N}_J^e$. Taking this into consideration, the definitions 4.14, 4.27 and 4.18 adopt the following extended form within a finite element:

$$\boldsymbol{G} = \left[\boldsymbol{N} \cdots \boldsymbol{G}_S^j \cdots \boldsymbol{G}_F^j \cdots \boldsymbol{G}_J^{j-m} \cdots \right], \tag{4.82}$$

$$\boldsymbol{B} = \left[\boldsymbol{B}_N \cdots \boldsymbol{B}_S^j \cdots \boldsymbol{B}_F^j \cdots \boldsymbol{B}_J^{j-m} \cdots \right], \tag{4.83}$$

$$\boldsymbol{q} = \left[\tilde{\boldsymbol{u}}^T \cdots \boldsymbol{b}^{jT} \cdots \boldsymbol{c}^{jT} \cdots \boldsymbol{d}^{j-mT} \cdots \right]^T, \tag{4.84}$$

$\forall j, m \mid j \neq m \in \mathcal{N}_c^e \wedge \forall (j-m) \in \mathcal{N}_J^e$, where:

$$\boldsymbol{G}_J^{j-m} = \left[\tilde{j}_i^{j-m} \begin{bmatrix} N_i & 0 \\ 0 & N_i \end{bmatrix} \cdots \right], \tag{4.85}$$

$$\boldsymbol{B}_J^{j-m} = \left[\tilde{j}_i^{j-m} \begin{bmatrix} \frac{\partial N_i}{\partial x} & 0 \\ 0 & \frac{\partial N_i}{\partial y} \\ \frac{\partial N_i}{\partial y} & \frac{\partial N_i}{\partial x} \end{bmatrix} \cdots \right], \tag{4.86}$$

$$\boldsymbol{d}^{j-m} = \left[\boldsymbol{d}_i^{j-mT} \cdots \right]^T, \quad \forall i \in I_J^{j-m} \cap I_e. \tag{4.87}$$

Similarly to that presented in Equation 4.76, the relative displacement field along the crack j reads:

$$\boldsymbol{\mathcal{N}}^j = \left[\cdots \boldsymbol{\mathcal{N}}_S^j \cdots \boldsymbol{\mathcal{N}}_F^j \cdots \boldsymbol{\mathcal{N}}_J^{j-m} \cdots \boldsymbol{\mathcal{N}}_J^{m-j} \cdots \right], \tag{4.88}$$

$$\boldsymbol{a}^j = \left[\cdots \boldsymbol{b}^{jT} \cdots \boldsymbol{c}^{jT} \cdots \boldsymbol{d}^{j-mT} \cdots \boldsymbol{d}^{m-jT} \cdots \right]^T, \tag{4.89}$$

$\forall m \neq j \in \mathcal{N}_c^e \wedge \forall (j-m) \in \mathcal{N}_J^e$, being:

$$\boldsymbol{\mathcal{N}}_J^{j-m} = \left[\mp j_i^{j-m} \begin{bmatrix} N_i & 0 \\ 0 & N_i \end{bmatrix} \cdots \right], \tag{4.90}$$

$$\boldsymbol{\mathcal{N}}_J^{m-j} = \left[2 \begin{bmatrix} N_i & 0 \\ 0 & N_i \end{bmatrix} \cdots \right], \quad \forall i \in I_J \cap I_e. \tag{4.91}$$

The discretisation exposed above replaces the discretisation performed in the previous section.

4.2. Reinforcing bars

Generally, for the modelling of reinforced concrete structures, reinforcing bars are discretised into finite elements (truss, beam, plate, shell or solid elements), whereas interface elements[2] are used to represent the interface, thus modelling the bond behaviour. This methodology has been successfully used over the years since it was presented for the first time by NGO [90]. Smeared models and embedded methods have been also developed for this purpose, see [58].

In this work, a different approach based on the work of RADTKE et al. [100] is presented.

In that study, RADTKE et al. proposed an enrichment that can handle discrete thin fibres in a continuum matrix without explicitly meshing them. The same approach is used then to model embedded reinforcing bars. This discrete approach is consistent with the representation of concrete as a homogeneous continuum and individual reinforcing bars as axial members.

The bond behaviour of the interface is not perfect, allowing a relative displacement between the reinforcement and the surrounding concrete along the reinforcement direction. RADTKE et al. considered that this is equivalent to describe the effect of a tunnelling crack in the matrix (concrete) around the reinforcement or a fully debonded interface and, therefore, an enrichment that is discontinuous at the interface can characterise this behaviour.

RADTKE et al. proposed the following HEAVISIDE enrichment function:

$$H(\boldsymbol{x}) = \begin{cases} 1 & \text{if} \quad \boldsymbol{x} \in \Omega_r, \\ 0 & \text{if} \quad \boldsymbol{x} \in \Omega, \end{cases} \tag{4.92}$$

where Ω_r represents the reinforcement domain, which is also defined by the union of straight-line segments.

The nodes whose support contains the reinforcement are enriched with the function $H(\boldsymbol{x})$, thus forming the set of nodes I_H. Figure 4.8 illustrates the enrichment strategy.

[2] Also known as bond elements.

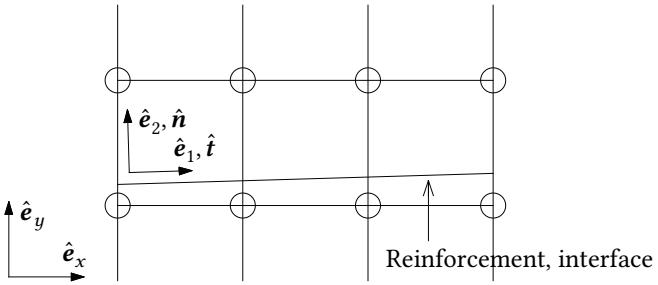

Figure 4.8.: Enrichment strategy for reinforcing bars.

The displacement field in the reinforcement domain is then approximated by:

$$\boldsymbol{u}(\boldsymbol{x}) = \sum_{i \in I} N_i(\boldsymbol{x}) \boldsymbol{u}_i + \sum_{i \in I_H} N_i(\boldsymbol{x}) H(\boldsymbol{x}) \boldsymbol{f}_i, \quad \boldsymbol{x} \in \Omega_r, \tag{4.93}$$

where $\boldsymbol{f}_i$ are the additional degrees of freedom at node i associated with the HEAVISIDE enrichment.

Considering that the function $H(\boldsymbol{x})$ takes the value 1 along the reinforcement, the equation above can be rewritten as:

$$\boldsymbol{u}(\boldsymbol{x}) = \sum_{i \in I} N_i(\boldsymbol{x}) \boldsymbol{u}_i + \sum_{i \in I_H} N_i(\boldsymbol{x}) \boldsymbol{f}_i, \quad \boldsymbol{x} \in \Omega_r. \tag{4.94}$$

For multiple layers of reinforcing bars it is assumed, as in RADTKE et al., that each layer is treated separately and, consequently, there is no interaction between them. Only fibre-matrix interaction is considered. This is an acceptable scenario, since the bars do not come into contact with each other[3].

Therefore, the same approach exposed above is used for each additional layer. Consider then N_r reinforcing bars layers. Each of them comprises a domain Ω_r^k, where k stands for the k-th layer, being $k = 1$ to N_r. The nodes of the elements containing the reinforcement layer k form the set of nodes I_H^k and

[3] The interaction between the longitudinal and transverse reinforcement is treated in Section 4.4

have associated the additional degrees of freedom $\boldsymbol{f}_i^k$. Then, the displacement field of the k-th layer can be expressed in matrix notation within a finite element as follows:

$$\boldsymbol{u}^k(\boldsymbol{x}) = \boldsymbol{G}_r(\boldsymbol{x})\boldsymbol{q}_r^k, \quad \boldsymbol{x} \in \Omega_r^k, \tag{4.95}$$

with the shape functions matrix $\boldsymbol{G}_r(\boldsymbol{x})$ defined as:

$$\boldsymbol{G}_r = \Big[\boldsymbol{N}\ \boldsymbol{N}\Big], \tag{4.96}$$

and the nodal displacements vector $\boldsymbol{q}_r^k$, as:

$$\boldsymbol{q}_r^k = \Big[\bar{\boldsymbol{u}}^T\ \boldsymbol{f}^{kT}\Big]^T. \tag{4.97}$$

The standard shape functions matrix $\boldsymbol{N}(\boldsymbol{x})$ is defined in the same way as in Equation 4.15. The vectors $\bar{\boldsymbol{u}}$ and $\boldsymbol{f}^k$ group the standard and extra degrees of freedom (associated with the layer k) of the element, respectively. The latter can be written as:

$$\boldsymbol{f}^k = \Big[\boldsymbol{f}_i^{kT} \cdots\Big]^T, \quad \forall i \in I_e. \tag{4.98}$$

The internal virtual work associated with the reinforcement defined in Equation 3.48 takes the following form:

$$\delta W^{int} = \delta \boldsymbol{Q} \sum_{k=1}^{N_r} \prod_{e=1}^{N_e} \left(\int_{\Omega_r^k} \boldsymbol{B}_r^T \boldsymbol{\sigma}^k \, dA \right). \tag{4.99}$$

In this case, the compatibility matrix $\boldsymbol{B}_r(\boldsymbol{x})$ is defined as:

$$\boldsymbol{B}_r = \Big[\boldsymbol{B}_N\ \boldsymbol{B}_N\Big]. \tag{4.100}$$

RADTKE et al. considered also that the reinforcement domain reduces to a line because of its negligible diameter or thickness compared with its length and, especially, compared with the size of the matrix domain. Under these

assumptions, the domain integral exposed above is replaced by a line integral along the reinforcement:

$$\delta W^{int} = \delta \boldsymbol{Q} \sum_{k=1}^{N_r} \prod_{e=1}^{N_e} \left(\int_{\Gamma_{r,e}^k} A^k \boldsymbol{B}_r^T \boldsymbol{\sigma}^k \, dl \right). \tag{4.101}$$

A represents the total cross area of the reinforcement layer, i.e. $A = n_\phi \pi \phi^2 / 4$, where ϕ corresponds to the diameter of the bar and n_ϕ is the number of reinforcement rods.

The internal force vector $\boldsymbol{F}^R$ associated with the reinforcing bars reads then:

$$\boldsymbol{F}^R = \sum_{k=1}^{N_r} \prod_{e=1}^{N_e} \left(\int_{\Gamma_{r,e}^k} A^k \boldsymbol{B}_r^T \boldsymbol{\sigma}^k \, dl \right), \tag{4.102}$$

which must be added to the left-hand side of the discrete equilibrium equation 4.41.

The elasto-plastic tangent matrix is given by:

$$\boldsymbol{K}^R = \sum_{k=1}^{N_r} \prod_{e=1}^{N_e} \left(\int_{\Gamma_{r,e}^k} A^k \boldsymbol{B}_r^T \boldsymbol{C}^{ed,k} \boldsymbol{B}_r \, dl \right), \tag{4.103}$$

where $\boldsymbol{C}^{ed,k}$ is the elasto-plastic constitutive matrix.

Since the HEAVISIDE function is null in the concrete domain, the enrichment 4.92 does not introduce any additional term associated with the concrete bulk. Hence, the discretisation performed in the previous section remains unchanged.

This approach treats then the cracked concrete bulk as a background on which discrete bars are superimposed as shown Figure 4.9, being the transfer of bond forces their only interaction mechanisms.

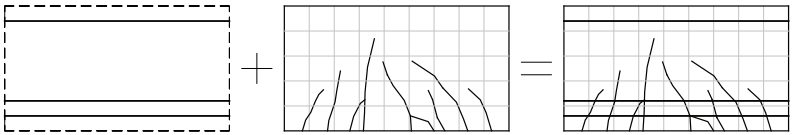

Figure 4.9.: Discrete bars superimposed on a background mesh.

4.2.1. Constitutive model

The yield function 3.51 can be expressed in terms of the matrix form (VOIGT notation) of the stress tensor as:

$$f(\boldsymbol{\sigma}(\boldsymbol{x}), \kappa) = \left\| \boldsymbol{R}_{\sigma} \boldsymbol{\sigma}(\boldsymbol{x}) \right\| - \left(f_y + H\kappa \right). \tag{4.104}$$

The transformation vector $\boldsymbol{R}_{\sigma}$ is given by:

$$\boldsymbol{R}_{\sigma} = \begin{bmatrix} \hat{t}_x^2 & \hat{t}_y^2 & 2\hat{t}_x\hat{t}_y \end{bmatrix} \tag{4.105}$$

being $\hat{t}_x$ and $\hat{t}_y$ the Cartesian components of the unit tangent vector to the reinforcing steel, see Figure 4.8.

Considering the previous yield function, the elasto-plastic constitutive matrix takes the following form:

$$\boldsymbol{C}^{ed,k} = \boldsymbol{C}^k - \frac{\boldsymbol{C}^k \left(\dfrac{\partial f}{\partial \boldsymbol{\sigma}} \right) \left(\dfrac{\partial f}{\partial \boldsymbol{\sigma}} \right)^T \boldsymbol{C}^k}{\left(\dfrac{\partial f}{\partial \boldsymbol{\sigma}} \right)^T \boldsymbol{C}^k \left(\dfrac{\partial f}{\partial \boldsymbol{\sigma}} \right) + H} \tag{4.106}$$

4.3. Bond model

Consider the Figure 4.10 which shows an idealisation of the bond interaction between the reinforcement and the surrounding concrete. Let us focus our attention on the points $\boldsymbol{p}^+(\boldsymbol{x}^+)$ and $\boldsymbol{p}^-(\boldsymbol{x}^-)$. The point $\boldsymbol{p}^+$ belongs to the reinforcement domain, while the point $\boldsymbol{p}^-$, to the concrete domain. The displacement jump can be determined as the difference between the displacements

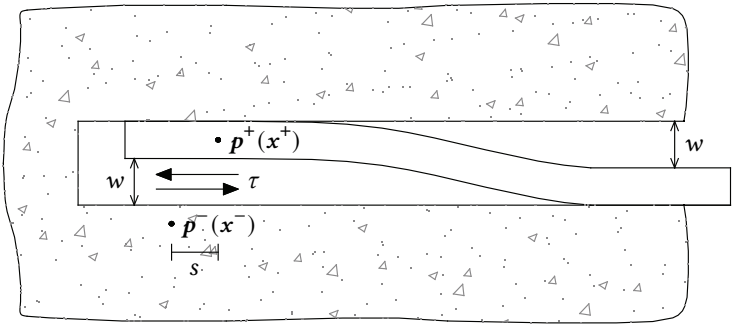

Figure 4.10.: Idealised bond interaction.

of these two points. Consider for simplicity and without loss of generality the uncracked state, then using the displacement field approximation for the reinforcing bars given by the Equation 4.95 and under small displacement assumptions, the displacement jump across the interface can be written in matrix notation as:

$$\boldsymbol{w}^k(\boldsymbol{x}) = \boldsymbol{u}^{k\,+}(\boldsymbol{x}) - \boldsymbol{u}^-(\boldsymbol{x}) = \boldsymbol{N}(\boldsymbol{x})\boldsymbol{f}^k, \quad \boldsymbol{x} \in \Gamma_r^k. \tag{4.107}$$

Replacing the discretisation given above in the definition of the work of the bond stresses 3.50, an expression for the bond force vector $\boldsymbol{F}^{bond}$ is obtained:

$$\boldsymbol{F}^{bond} = \sum_{k=1}^{N_r} \prod_{e=1}^{N_e} \left(\int_{\Gamma_{r,e}^k} \boldsymbol{N}^T \boldsymbol{R}^k \boldsymbol{A}^k \boldsymbol{T}^k (\boldsymbol{W}^k)\, dl \right), \tag{4.108}$$

with:

$$\boldsymbol{A} = \begin{bmatrix} A_n & 0 \\ 0 & A_t \end{bmatrix}, \tag{4.109}$$

being A_n and A_t the contact areas associated with the radial stress σ and the bond stress τ, respectively. Considering the presented bond laws, the contact area A_t is assumed to be equal to the sum of the perimeters of each bar, i.e. $n_\phi \pi \phi$; while the contact area A_n is the projection of the contact surface between the bar and the concrete in the out-of-plane direction, i.e. $n_\phi \phi$.

The presented bond model introduces a certain arbitrariness in the choice of the point $\boldsymbol{p}^{-}(\boldsymbol{x})$ and, therefore, of the tangential and normal unit vectors. As a result, the constitutive relations are symmetrical with respect to negatives values of s and w, i.e. $\tau(s) = -\tau_0(-s)$ and $\sigma(w) = -\sigma_0(-w)$, in which τ_0 and σ_0 are the bond laws according to the Equations 3.56 and 3.62, respectively.

The tangent matrix associated to the bond force vector can be computed from:

$$\boldsymbol{K}^{bond} = \sum_{k=1}^{N_r} \prod_{e=1}^{N_e} \left(\int_{\Gamma_{r,e}} \boldsymbol{N}^T \boldsymbol{R}^k \boldsymbol{A}^k \frac{\partial \boldsymbol{T}^k(\boldsymbol{\mathcal{W}}^k)}{\partial \boldsymbol{\mathcal{W}}^k} \boldsymbol{R}^{k\,T} \boldsymbol{N}\, dl \right). \tag{4.110}$$

Herein, $\partial \boldsymbol{T} / \partial \boldsymbol{\mathcal{W}}$ represents the tangent stiffness matrix of the bond law and is given by:

$$\frac{\partial \boldsymbol{T}}{\partial \boldsymbol{\mathcal{W}}} = \begin{bmatrix} \frac{\partial \sigma}{\partial w} & \frac{\partial \sigma}{\partial s} \\ \frac{\partial \tau}{\partial w} & \frac{\partial \tau}{\partial s} \end{bmatrix}. \tag{4.111}$$

The relative displacement in the local coordinate system can be obtained from the transformation:

$$\boldsymbol{\mathcal{W}} = \boldsymbol{R}^T \boldsymbol{w}. \tag{4.112}$$

Finally, the following discrete equilibrium equation is achieved:

$$\boldsymbol{K}\boldsymbol{Q} + \boldsymbol{F}^R + \boldsymbol{F}^D + \boldsymbol{F}^{coh} + \boldsymbol{F}^{bond} = \boldsymbol{F}^{ext}, \tag{4.113}$$

as well as the linearised system:

$$\boldsymbol{\mathcal{K}}_n \Delta \boldsymbol{Q}_{n+1} = -\boldsymbol{Re}(\boldsymbol{Q}_n), \tag{4.114}$$

$$\boldsymbol{Re}(\boldsymbol{Q}) = \boldsymbol{K}\boldsymbol{Q} + \boldsymbol{F}^R(\boldsymbol{Q}) + \boldsymbol{F}^D(\boldsymbol{Q}) + \boldsymbol{F}^{coh}(\boldsymbol{Q}) + \boldsymbol{F}^{bond}(\boldsymbol{Q}) - \boldsymbol{F}^{ext}, \tag{4.115}$$

$$\boldsymbol{\mathcal{K}} = \boldsymbol{K} + \boldsymbol{K}^R + \boldsymbol{K}^D + \boldsymbol{K}^{coh} + \boldsymbol{K}^{bond}. \tag{4.116}$$

4.3.0.1. Interaction between reinforcement and transverse cracks

Reinforcing bars are embedded in concrete mainly to provide tensile strength to the structure once cracking occurs, thus preventing excessive cracking and premature failure. Bond mechanisms are responsible for the redistribution of forces from the surrounding concrete to the bars. In this regard, a proper consideration of the influence of the cracked concrete bulk on the bond model is therefore required. For a cracked state, the interfacial relative displacement takes the following form:

$$\boldsymbol{w}^k(\boldsymbol{x}) = \boldsymbol{u}^{k\,+}(\boldsymbol{x}) - \boldsymbol{u}^{-}(\boldsymbol{x}) = \boldsymbol{\mathcal{N}}_r(\boldsymbol{x})\boldsymbol{a}_r^k, \quad \boldsymbol{x} \in \Gamma_r^k, \tag{4.117}$$

where the approximation 4.13, which defines the displacement of the cracked concrete bulk, is used.

Matrices $\boldsymbol{\mathcal{N}}_r(\boldsymbol{x})$ and $\boldsymbol{a}_r^k$ are given by:

$$\boldsymbol{\mathcal{N}}_r = \left[\boldsymbol{N} \cdots - \boldsymbol{G}_S^j \cdots - \boldsymbol{G}_F^j \cdots - \boldsymbol{G}_J^{j-m} \cdots \right], \tag{4.118}$$

$$\boldsymbol{a}_r^k = \left[\boldsymbol{f}^{k\,T} \cdots \boldsymbol{b}^{j\,T} \cdots \boldsymbol{c}^{j\,T} \cdots \boldsymbol{d}^{j-m\,T} \cdots \right]^T, \tag{4.119}$$

$\forall j, m \mid j \neq m \in \mathcal{N}_c^e \wedge \forall (j-m) \in \mathcal{N}_J^e \wedge \forall k \in \mathcal{N}_r^e$.

The functions $\boldsymbol{G}_S^j(\boldsymbol{x})$, $\boldsymbol{G}_F^j(\boldsymbol{x})$ and $\boldsymbol{G}_J^{j-m}(\boldsymbol{x})$, and the values $\boldsymbol{f}^k$, $\boldsymbol{b}^j$, $\boldsymbol{c}^j$ and $\boldsymbol{d}^{j-m}$ were defined in Equations 4.16, 4.17, 4.85, 4.98, 4.20, 4.21 and 4.87, respectively.

The discretisation exposed above replaces the discretisation performed in Equation 4.107 and, therefore, the matrix $\boldsymbol{N}(\boldsymbol{x})$ is replaced by the matrix $\boldsymbol{\mathcal{N}}_r(\boldsymbol{x})$ in the line integrals 4.108 and 4.110.

The relative displacement between the crack surfaces is not influenced by the presence of the reinforcement. Hence, the approximation 4.22 remains unchanged.

4.4. Transverse reinforcement

Transverse reinforcement increases the shear capacity of the structure, and provides confinement to the core concrete and lateral restraint against buckling of the longitudinal reinforcement. Its influence on the structure is therefore significant. Hence, its consideration when modelling reinforced concrete members is important. As reinforcing bar, transverse reinforcement is also modelled using the X-FEM formulation exposed in Section 4.2. In the literature, it is often assumed that the bond between the transverse bars and the concrete is perfect, which may over-estimate the shear capacity of the structure. In this work, the transverse bars are assumed to be strongly bonded to the surrounding concrete, with the bond behaviour being that depicted in Section 3.5.

The penalty method is used to mediate the interaction between the longitudinal and transverse reinforcement once these come into contact. Consider the Figure 4.11, which shows a schematic representation of a typical distribution of reinforcing bars. Let us focus our attention now on the point $\boldsymbol{p}_C(\boldsymbol{x}_C)$, which defines a contact point between both reinforcements in the reference configuration (undeformed configuration). The coordinates $\boldsymbol{x}_C$ are known and, therefore, must be defined in advance. The points coming into contact are represented by $\boldsymbol{p}_C^l(\boldsymbol{x}_C^l)$ (on the longitudinal bar) and by $\boldsymbol{p}_C^t(\boldsymbol{x}_C^t)$ (on the transverse bar). From now on, index l and t will stand for the longitudinal and transverse bar, respectively. Initially, both points occupy the same location, i.e. $\boldsymbol{x}_C^l = \boldsymbol{x}_C^t = \boldsymbol{x}_C$. Once loading starts, the points separate from each other and, under small displacements assumption, the new coordinates read:

$$\boldsymbol{x}_C^l = \boldsymbol{x}_C + \boldsymbol{u}^l(\boldsymbol{x}_C), \tag{4.120}$$

$$\boldsymbol{x}_C^t = \boldsymbol{x}_C + \boldsymbol{u}^t(\boldsymbol{x}_C), \tag{4.121}$$

where $\boldsymbol{u}^l(\boldsymbol{x}_C)$ and $\boldsymbol{u}^t(\boldsymbol{x}_C)$ are the displacements of the points $\boldsymbol{p}_C^l$ and $\boldsymbol{p}_C^t$, respectively.

To formulate the contact problem, it is necessary to calculate the gap between both reinforcements at the points $\boldsymbol{p}_C^l$ and $\boldsymbol{p}_C^t$ in the direction tangential to

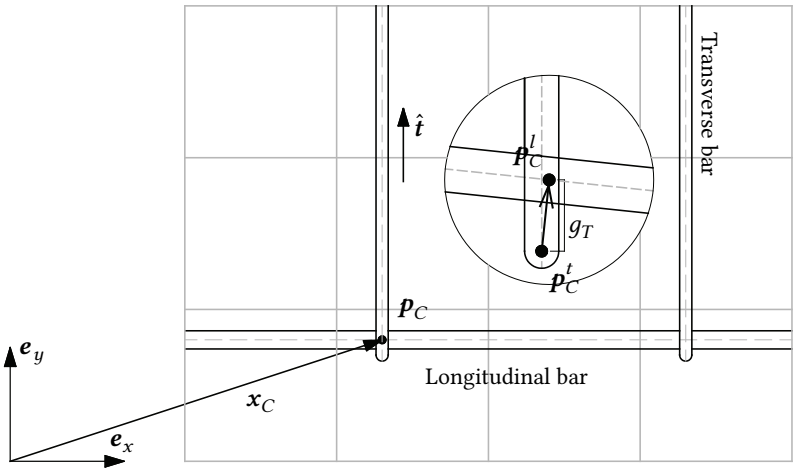

Figure 4.11.: Representation of a typical distribution of longitudinal and transverse reinforcement.

the transverse bar. Then, the Equations 4.120 and 4.121, the tangential gap can be computed as:

$$g_T(\boldsymbol{x}_C) = \left[\boldsymbol{x}_C^l - \boldsymbol{x}_C^t\right]^T \hat{\boldsymbol{t}} = \left[\boldsymbol{u}^l(\boldsymbol{x}_C) - \boldsymbol{u}^t(\boldsymbol{x}_C)\right]^T \hat{\boldsymbol{t}}, \tag{4.122}$$

where $\hat{\boldsymbol{t}}$ is the tangential unit vector to the transverse bar and is considered to go from the point $\boldsymbol{p}_C$ to the other end of the bar (see Figure 4.11).

Using the discretisation 4.95, the tangential gap takes the following form:

$$g_T(\boldsymbol{x}_C) = \left[\boldsymbol{G}_r(\boldsymbol{x}_C)\boldsymbol{q}_r^l - \boldsymbol{G}_r(\boldsymbol{x}_C)\boldsymbol{q}_r^t\right]^T \hat{\boldsymbol{t}} = \left[\boldsymbol{N}(\boldsymbol{x}_C)\boldsymbol{f}^l - \boldsymbol{N}(\boldsymbol{x}_C)\boldsymbol{f}^t\right]^T \hat{\boldsymbol{t}}. \tag{4.123}$$

Defining the matrices:

$$\boldsymbol{G}^{l-t}(\boldsymbol{x}_C) = \begin{bmatrix} \boldsymbol{N}(\boldsymbol{x}_C) \\ -\boldsymbol{N}(\boldsymbol{x}_C) \end{bmatrix}^T, \tag{4.124}$$

$$\boldsymbol{f}^{l-t} = \left[\boldsymbol{f}^{l\,T}\ \boldsymbol{f}^{t\,T}\right]^T, \tag{4.125}$$

Equation 4.123 can be simplified further:

$$g_T(\boldsymbol{x}_C) = \left[\boldsymbol{G}^{l-t}(\boldsymbol{x}_C)\boldsymbol{f}^{l-t}\right]^T \hat{\boldsymbol{t}}. \tag{4.126}$$

As soon as the bars come into contact, a contact pressure p_T is induced to avoid penetration. In order to enforce the contact constraints, a penalty formulation is chosen:

$$p_T = \begin{cases} \epsilon_N g_T & \text{if} \quad g_T < 0, \\ 0 & \text{if} \quad g_T \geq 0, \end{cases} \tag{4.127}$$

where ϵ_N is the penalty stiffness.

This procedure is then extended to all N_C contact points between the longitudinal and transverse reinforcements. For this purpose, it is necessary to specify, for each contact, the bars that are coming into contact, which define an ordered pair $(l-t)^j$, and the corresponding contact point $\boldsymbol{p}_C^j$ with coordinates $\boldsymbol{x}_C^j$, being $j = 1$ to N_C. The weak form of the contact pressure p_T is reduced finally the following nodal force vector after replacing the discretisation 4.126 for all contact points:

$$\boldsymbol{F}^C = \sum_{j=1}^{N_C} \prod_{e=e_C^j} \left(p_{T_C}^j \boldsymbol{G}^{l-t}(\boldsymbol{x}_C^j)^T \hat{\boldsymbol{t}} \right), \tag{4.128}$$

being its tangent matrix:

$$\boldsymbol{K}^C = \sum_{j=1}^{N_C} \prod_{e=e_C^j} \left(\boldsymbol{G}^{l-t}(\boldsymbol{x}_C^j)^T \hat{\boldsymbol{t}} \frac{\partial p_{T_C}^j}{\partial g_{T_C}^j} \hat{\boldsymbol{t}}^T \boldsymbol{G}^{l-t}(\boldsymbol{x}_C^j) \right), \tag{4.129}$$

where e_C^j corresponds to the element that contains the contact point $\boldsymbol{p}_C^j$.

Additionally, for a better representation of the transverse reinforcement, the horizontal legs anchoring the vertical legs around the main bars are implicitly modelled by imposing a perfect contact with the surrounding concrete at each endpoint of the vertical legs in the axial direction, thus allowing no relative displacement (slip) between both materials at these points. For each

transverse reinforcement, a penalty formulation is also used to enforce perfect contact, i.e. $\tau = \epsilon_N s(\boldsymbol{x}_S)$ at $\boldsymbol{p}_S$ and $\tau = \epsilon_N s(\boldsymbol{x}_E)$ at $\boldsymbol{p}_E$, where $\boldsymbol{p}_S$ and $\boldsymbol{p}_E$ are the endpoints of the transverse bar. Considering the discretisation 4.117, the weak form of the contact formulation adopts the following form:

$$\boldsymbol{F}^T = \sum_{j=1}^{N_T} \left[\prod_{e=e_S^j} \left(\boldsymbol{\mathcal{N}}_r^T(\boldsymbol{x}_S^j) \hat{\boldsymbol{t}} \epsilon_N \hat{\boldsymbol{t}}^T \boldsymbol{\mathcal{N}}_r(\boldsymbol{x}_S^j) \boldsymbol{a}_r^t \right) + \prod_{e=e_E^j} \left(\boldsymbol{\mathcal{N}}_r^T(\boldsymbol{x}_E^j) \hat{\boldsymbol{t}} \epsilon_N \hat{\boldsymbol{t}}^T \boldsymbol{\mathcal{N}}_r(\boldsymbol{x}_E^j) \boldsymbol{a}_r^t \right) \right], \tag{4.130}$$

with the tangent matrix given by:

$$\boldsymbol{K}^T = \sum_{j=1}^{N_T} \left[\prod_{e=e_S^j} \left(\boldsymbol{\mathcal{N}}_r^T(\boldsymbol{x}_S^j) \hat{\boldsymbol{t}} \epsilon_N \hat{\boldsymbol{t}}^T \boldsymbol{\mathcal{N}}_r(\boldsymbol{x}_S^j) \right) + \prod_{e=e_E^j} \left(\boldsymbol{\mathcal{N}}_r^T(\boldsymbol{x}_E^j) \hat{\boldsymbol{t}} \epsilon_N \hat{\boldsymbol{t}}^T \boldsymbol{\mathcal{N}}_r(\boldsymbol{x}_E^j) \right) \right]. \tag{4.131}$$

Herein, N_T denotes the number of transverse reinforcement, and e_S^j and e_E^j correspond to the element containing the points $\boldsymbol{p}_S^j$ and $\boldsymbol{p}_E^j$, respectively.

The force vectors 4.128 and 4.130 are finally added to the discrete equilibrium equation.

4.5. Bonded reinforcement

The restoring or improvement of the load carrying capacity, serviceability and durability of existing reinforced concrete structures has gained more and more attention over the last decades. This need may arise as a result of errors in the design or execution, changes in the load requirements, design code changes, seismic upgrade, lack of maintenance, as well as the inherent deterioration of the structure. Besides numerous other methods, the structural upgrade can be achieved using externally bonded reinforcement. This

technique involves bonding strengthening materials to the external concrete surface using adhesives. Steel plates and Fibre Reinforced Polymer (FRP) systems in the form of laminates, strips or sheets bonded with epoxy adhesive are the strengthening methods most commonly used.

In [46], a general description of materials and techniques related to the application of FRP as external reinforcement, as well as the design and structural behaviour of strengthened concrete members, are summarised.

The HEAVISIDE enrichment presented in Section 4.2 is also used to represent the influence of the bonded reinforcement on the concrete bulk. The straight-line segments defining the reinforcement are then placed at the edge of the elements, but inside them. In order to avoid shear locking, a gap between the edge and the reinforcement is introduced. A value of 0.01 mm seems to be sufficient to prevent the locking. The enrichment strategy is illustrated in Figure 4.12. The internal force vector $\boldsymbol{F}^R$ as well as the tangent matrix $\boldsymbol{K}^R$ are defined then in the same way as in Equations 4.102 and 4.103, respectively. The total cross area A is given by $A = t \cdot b$, where t and b are the thickness and width of the external reinforcement, respectively.

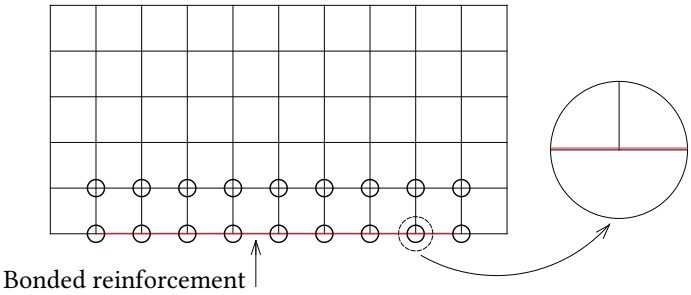

Figure 4.12.: Enrichment strategy for bonded reinforcement.

4.5.1. Constitutive behaviour

Bonded reinforcement is primarily loaded in tension and, therefore, a yield function based on the axial stress is considered for those materials exhibiting a non-linear behaviour. For brittle materials, such as fibre reinforced polymers, the constitutive behaviour is assumed to be linear-elastic up to brittle failure.

4.5.2. Bond behaviour

The transfer of forces along the interface between the concrete surface and the bonded reinforcement is provided by the adhesive, mainly through chemical adhesion and mechanical interlocking, so that full composite action may develop. The interface, which comprises not only the adhesive but also the adjacent concrete, is modelled by means of the bond model presented in Section 4.3. The bond behaviour can be described by bond stress-slip relationships, which must necessarily consider the most common failure mechanics associated with strengthened structures, namely, the delamination of the concrete cover and the debonding of the reinforcement from the concrete substrate. These relationships present generally a linear-elastic branch until a certain threshold, corresponding to the local bond strength. Once this limit is exceeded, debonding begins and the curve starts to exhibit an irreversible softening behaviour up to a full debonding stage. The bilinear relationship shown in Figure 4.13 has proved to be a useful approximation for design and numerical purposes:

$$\tau(s) = \begin{cases} \tau_{max}\dfrac{s}{s_1} & \text{for} \quad 0 \leq s \leq s_1, \\ \tau_{max} - \tau_{max}\dfrac{(s - s_1)}{(s_2 - s_1)} & \text{for} \quad s_1 \leq s \leq s_2, \\ 0 & \text{for} \quad s_2 < s. \end{cases} \tag{4.132}$$

Herein, τ_{max} denotes the maximum transferable bond stress, s_1, the associated slip and s_2, the ultimate slip. This law is calibrated based on experimental results.

Non-linear relationships for numerical investigation can be found in [88, 109].

Unloading and reloading are defined by the secant path. The radial stress σ is chosen so that normal separation and penetration is prevented. This is ensured by a penalty formulation. No coupling between the components σ and τ is assumed. The contact area A_t is equal to the width b of the bonded reinforcement.

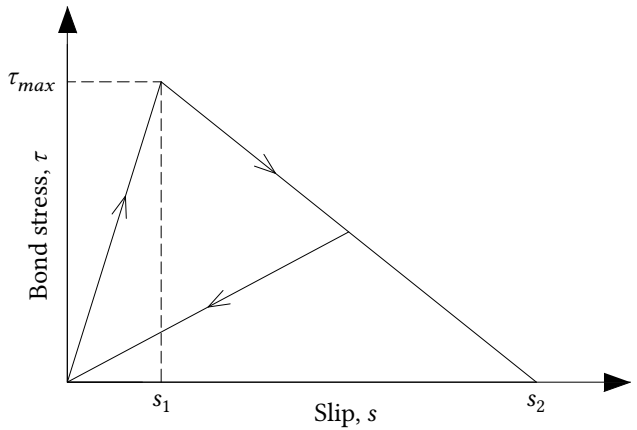

Figure 4.13.: Bond stress-slip relationship for bonded reinforcement.

4.6. Fibre reinforced concrete

Fibre Reinforced Concrete (FRC) refers to concrete reinforced with a multitude of discontinuous short thin fibres. These fibres are randomly distributed (embedded) throughout the entire volume of the matrix in relatively dilute concentrations. Fibres provide the concrete with significant post-cracking capacity and, therefore, used to replace conventional reinforcement in non-structural and structural elements such as industrial floor, road pavements, beams (as a substitute for shear reinforcement), slabs and tunnel linings. They may generally be used in any application where the following benefits are desired: protection from plastic shrinkage and cracking, improved strength, ductility and energy absorption capacity, increased service life, among others. Fibres are made of steel, glass, polymers and others natural or synthetic materials in various shapes and sizes.

A good overview about FRC and its applications can be found in [18] and [48]. FRC is included also in some design codes such as the CEB-FIP MODEL CODE 2010 [47] and the ACI Committee 544 [1]. For further information, the reader is referred to these documents.

Within the framework of the extended finite element method, RADTKE et al. [100] proposed a HEAVISIDE enrichment that can model an arbitrary number of arbitrarily orientated and positioned thin fibres within a finite

element without meshing them. The approach is schematically illustrated in Figure 4.14. This approach was already presented in Section 4.2 for the modelling of reinforcing bars. Therefore, the same expressions are applicable for the fibres. Each single fibre is treated separately and direct interaction between them is not considered.

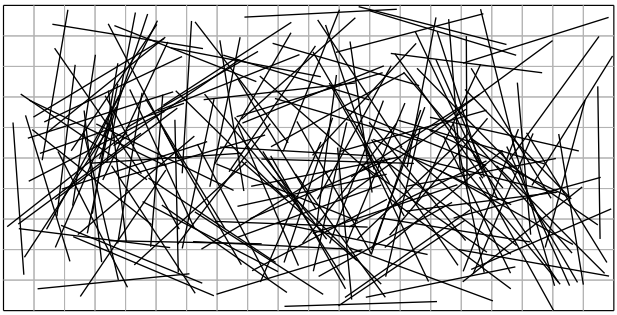

Figure 4.14.: Typical random fibres distribution.

4.6.1. Constitutive behaviour

As opposed to reinforcing bars, which are designed to be anchored in the concrete so that their yield strength can be developed, fibres are designed to pull-out of the concrete matrix prior to reaching their strength. Therefore, a linear-elastic behaviour is assumed for the fibres, although any constitutive law can be employed.

4.6.2. Bond behaviour

The mechanical behaviour of fibre reinforced concrete depends on the transfer of forces between the fibres and the concrete matrix, which is provided by physical and chemical adhesion, friction, and mechanical anchorage induced by complex fibre geometries. Bond exhibits normally a linear-elastic behaviour until a certain strength, beyond which debonding gradually begins to occur (bond degradation) with the consequent fall in the transferable bond (shear) stress until friction becomes the dominant transfer mechanism.

This behaviour may also be modelled by means of a local bond model according to a bond stress-slip law. The same approach stated in Section 4.3 is used separately for each single fibre to model the bond interaction. A suitable bond stress-slip law for design and numerical purposes was developed by BANHOLZER et al. [6] based on experimental data from pull-out tests. This law is based on a multilinear relationship, consisting of an initial elastic branch followed by a softening and a frictional branch as illustrated in Figure 4.15. This law is adopted in this work.

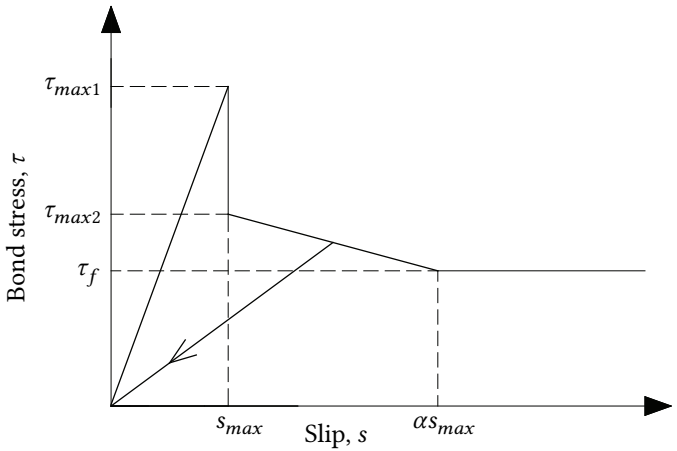

Figure 4.15.: Bond stress-slip relationship for fibres.

The bond law is defined by five parameters: τ_{max1}, denoting the maximum transferable bond (shear) stress; s_{max}, the maximum slip in the elastic branch before debonding onset; τ_{max2}, the maximum bond stress in the softening branch; the factor α, determining the maximum slip within the softening branch; and the frictional stress τ_f; according to the following expression:

$$\tau(s) = \begin{cases} \tau_{max} \dfrac{s}{s_{max}} & \text{for} \quad 0 \le s \le s_{max}, \\ \tau_{max2} - \left(\tau_{max2} - \tau_f\right) \dfrac{(s - s_{max})}{s_{max}\,(\alpha - 1)} & \text{for} \quad s_{max} \le s \le \alpha s_{max}, \\ \tau_f & \text{for} \quad \alpha s_{max} < s. \end{cases} \tag{4.133}$$

In case of unloading/reloading in the softening/frictional branch, the secant path is followed. The normal component of the bond stress, i.e the radial stress σ, is neglected. No coupling between the components is assumed.

4.7. Example

By way of example, the extended finite element approximation of a discretised body with an arbitrary configuration of cracks and reinforcing bars is described in this section. Figure 4.16 shows the finite element mesh as well as the nodal enrichment strategy. Let us focus our attention on the elements 1 and 2. Element 1 is formed by the nodes 1, 2, 3 and 4, and is crossed by the crack 4 and the reinforcing bar 1; while element 2 is composed by the nodes 4, 3, 5 and 6, and is crossed by the crack 1. Table 4.1 summarises the enrichment for the nodes belonging to these elements, where the type of enrichment as well as the corresponding cracks and reinforcing bars are stated. The matrices that define the approximate fields are given below:

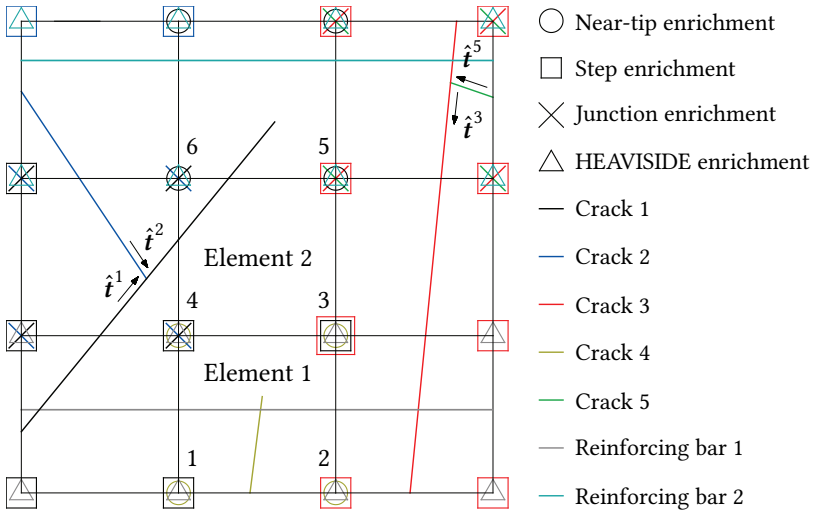

Figure 4.16.: Nodal enrichment strategy and mesh.

Element 1

Table 4.1.: Nodal enrichment strategy.

	Enrichment			
Nodes	Near-tip	Step	Junction	HEAVISIDE
1	C4	C1	–	R1
2	C4	C3	–	R1
3	C4	C1, C3	–	R1
4	C4	C1	C1-C2	R1
5	C1	C3	C3-C5	R2
6	C1	–	C1-C2	R2

Concrete bulk

$$
\begin{aligned}
\boldsymbol{G} &= \Big[\boldsymbol{N}_1 \ \boldsymbol{N}_2 \ \boldsymbol{N}_3 \ \boldsymbol{N}_4 \ \tilde{S}_1^1 \boldsymbol{N}_1 \ \tilde{S}_3^1 \boldsymbol{N}_3 \ \tilde{S}_4^1 \boldsymbol{N}_4 \ \tilde{S}_2^3 \boldsymbol{N}_2 \ \tilde{S}_3^3 \boldsymbol{N}_3 \\
&\quad \cdots \tilde{F}_1^4 \boldsymbol{N}_1 \ \tilde{F}_2^4 \boldsymbol{N}_2 \ \tilde{F}_3^4 \boldsymbol{N}_3 \ \tilde{F}_4^4 \boldsymbol{N}_4 \ \tilde{J}_4^{1-2} \boldsymbol{N}_4 \Big], \\
\boldsymbol{B} &= \Big[\partial \boldsymbol{N}_1 \ \partial \boldsymbol{N}_2 \ \partial \boldsymbol{N}_3 \ \partial \boldsymbol{N}_4 \ \tilde{S}_1^1 \partial \boldsymbol{N}_1 \ \tilde{S}_3^1 \partial \boldsymbol{N}_3 \ \tilde{S}_4^1 \partial \boldsymbol{N}_4 \ \tilde{S}_2^3 \partial \boldsymbol{N}_2 \ \tilde{S}_3^3 \partial \boldsymbol{N}_3 \\
&\quad \cdots \partial\big(\tilde{F}_1^4 \boldsymbol{N}_1\big) \ \partial\big(\tilde{F}_2^4 \boldsymbol{N}_2\big) \ \partial\big(\tilde{F}_3^4 \boldsymbol{N}_3\big) \ \partial\big(\tilde{F}_4^4 \boldsymbol{N}_4\big) \ \tilde{J}_4^{1-2} \partial \boldsymbol{N}_4 \Big], \\
\boldsymbol{q} &= \Big[\boldsymbol{u}_1^T \ \boldsymbol{u}_2^T \ \boldsymbol{u}_3^T \ \boldsymbol{u}_4^T \ \boldsymbol{b}_1^{1T} \ \boldsymbol{b}_3^{1T} \ \boldsymbol{b}_4^{1T} \ \boldsymbol{b}_2^{3T} \ \boldsymbol{b}_3^{3T} \\
&\quad \cdots \boldsymbol{c}_1^{4T} \ \boldsymbol{c}_2^{4T} \ \boldsymbol{c}_3^{4T} \ \boldsymbol{c}_4^{4T} \ \boldsymbol{d}_4^{1-2T} \Big]^T .
\end{aligned}
$$

These matrices are involved in the definitions 4.82, 4.83 and 4.84.

Cohesive crack 4

$$
\begin{aligned}
\boldsymbol{N}^4 &= \Big[2r^4 \boldsymbol{N}_1 \ 2r^4 \boldsymbol{N}_2 \ 2r^4 \boldsymbol{N}_3 \ 2r^4 \boldsymbol{N}_4 \Big], \\
\boldsymbol{a}^4 &= \Big[\boldsymbol{c}_1^{4T} \ \boldsymbol{c}_2^{4T} \ \boldsymbol{c}_3^{4T} \ \boldsymbol{c}_4^{4T} \Big]^T .
\end{aligned}
$$

These matrices are involved in the definitions 4.88 and 4.89.

Reinforcing bar 1

$$
\begin{aligned}
\boldsymbol{G}_r^1 &= \Big[\boldsymbol{N}_1\ \boldsymbol{N}_2\ \boldsymbol{N}_3\ \boldsymbol{N}_4\ \boldsymbol{N}_1\ \boldsymbol{N}_2\ \boldsymbol{N}_3\ \boldsymbol{N}_4\Big],\\
\boldsymbol{B}_r^1 &= \Big[\partial\boldsymbol{N}_1\ \partial\boldsymbol{N}_2\ \partial\boldsymbol{N}_3\ \partial\boldsymbol{N}_4\ \partial\boldsymbol{N}_1\ \partial\boldsymbol{N}_2\ \partial\boldsymbol{N}_3\ \partial\boldsymbol{N}_4\Big],\\
\boldsymbol{q}_r^1 &= \Big[\boldsymbol{u}_1^T\ \boldsymbol{u}_2^T\ \boldsymbol{u}_3^T\ \boldsymbol{u}_4^T\ \boldsymbol{f}_1^{1T}\ \boldsymbol{f}_2^{1T}\ \boldsymbol{f}_3^{1T}\ \boldsymbol{f}_4^{1T}\Big],\\
\boldsymbol{\mathcal{N}}_r &= \Big[\boldsymbol{N}_1\ \boldsymbol{N}_2\ \boldsymbol{N}_3\ \boldsymbol{N}_4\ -\tilde{S}_1^1\boldsymbol{N}_1\ -\tilde{S}_3^1\boldsymbol{N}_3\ -\tilde{S}_4^1\boldsymbol{N}_4\ -\tilde{S}_2^3\boldsymbol{N}_2\ -\tilde{S}_3^3\boldsymbol{N}_3\\
&\quad \cdots -\tilde{F}_1^4\boldsymbol{N}_1\ -\tilde{F}_2^4\boldsymbol{N}_2\ -\tilde{F}_3^4\boldsymbol{N}_3\ -\tilde{F}_4^4\boldsymbol{N}_4\ -\tilde{J}_4^{1-2}\boldsymbol{N}_4\Big],\\
\boldsymbol{a}_r^1 &= \Big[\boldsymbol{f}_1^{1T}\ \boldsymbol{f}_2^{1T}\ \boldsymbol{f}_3^{1T}\ \boldsymbol{f}_4^{1T}\ \boldsymbol{b}_1^{1T}\ \boldsymbol{b}_3^{1T}\ \boldsymbol{b}_4^{1T}\ \boldsymbol{b}_2^{3T}\ \boldsymbol{b}_3^{3T}\\
&\quad \cdots \boldsymbol{c}_1^{4T}\ \boldsymbol{c}_2^{4T}\ \boldsymbol{c}_3^{4T}\ \boldsymbol{c}_4^{4T}\ \boldsymbol{d}_4^{1-2T}\Big]^T.
\end{aligned}
$$

These matrices are involved in the definitions 4.96, 4.100, 4.97, 4.118 and 4.119.

Element 2

Concrete bulk

$$
\begin{aligned}
\boldsymbol{G} &= \Big[\boldsymbol{N}_4\ \boldsymbol{N}_3\ \boldsymbol{N}_5\ \boldsymbol{N}_6\ \tilde{S}_4^1\boldsymbol{N}_4\ \tilde{S}_3^1\boldsymbol{N}_3\ \tilde{S}_3^3\boldsymbol{N}_3\ \tilde{S}_5^3\boldsymbol{N}_5\ \tilde{F}_4^4\boldsymbol{N}_4\\
&\quad \cdots \tilde{F}_3^4\boldsymbol{N}_3\ \tilde{F}_5^1\boldsymbol{N}_5\ \tilde{F}_6^1\boldsymbol{N}_6\ \tilde{J}_4^{1-2}\boldsymbol{N}_4\ \tilde{J}_5^{3-5}\boldsymbol{N}_5\ \tilde{J}_6^{1-2}\boldsymbol{N}_6\Big],\\
\boldsymbol{B} &= \Big[\partial\boldsymbol{N}_4\ \partial\boldsymbol{N}_3\ \partial\boldsymbol{N}_5\ \partial\boldsymbol{N}_6\ \tilde{S}_4^1\partial\boldsymbol{N}_4\ \tilde{S}_3^1\partial\boldsymbol{N}_3\ \tilde{S}_3^3\partial\boldsymbol{N}_3\ \tilde{S}_5^3\partial\boldsymbol{N}_5\ \partial\big(\tilde{F}_4^4\boldsymbol{N}_4\big)\\
&\quad \cdots \partial\big(\tilde{F}_3^4\boldsymbol{N}_3\big)\ \partial\big(\tilde{F}_5^1\boldsymbol{N}_5\big)\ \partial\big(\tilde{F}_6^1\boldsymbol{N}_6\big)\ \tilde{J}_4^{1-2}\partial\boldsymbol{N}_4\ \tilde{J}_5^{3-5}\partial\boldsymbol{N}_5\ \tilde{J}_6^{1-2}\partial\boldsymbol{N}_6\Big],\\
\boldsymbol{q} &= \Big[\boldsymbol{u}_4^T\ \boldsymbol{u}_3^T\ \boldsymbol{u}_5^T\ \boldsymbol{u}_6^T\ \boldsymbol{b}_4^{1T}\ \boldsymbol{b}_3^{1T}\ \boldsymbol{c}_5^{1T}\ \boldsymbol{c}_6^{1T}\ \boldsymbol{b}_3^{3T}\ \boldsymbol{b}_5^{3T}\ \boldsymbol{c}_4^{4T}\ \boldsymbol{c}_3^{4T}\\
&\quad \cdots \boldsymbol{d}_4^{1-2T}\ \boldsymbol{d}_6^{1-2T}\ \boldsymbol{d}_5^{3-5T}\Big]^T.
\end{aligned}
$$

Cohesive crack 1

$$\boldsymbol{\mathcal{N}}^1 = \left[2\boldsymbol{N}_4 \; 2\boldsymbol{N}_3 \; 2r^1\boldsymbol{N}_5 \; 2r^1\boldsymbol{N}_6 \; {}^{-}j_4^{1-2}\boldsymbol{N}_4 \; {}^{-}j_6^{1-2}\boldsymbol{N}_6\right],$$

$$\boldsymbol{a}^1 = \left[\boldsymbol{b}_4^{1T} \; \boldsymbol{b}_3^{1T} \; \boldsymbol{c}_5^{1T} \; \boldsymbol{c}_6^{1T} \; \boldsymbol{d}_4^{1-2T} \; \boldsymbol{d}_6^{1-2T}\right]^T.$$

The matrices $\boldsymbol{N}_i$, $\partial\boldsymbol{N}_i$ and $\partial\left(\tilde{F}_i^j\boldsymbol{N}_i\right)$ are given by:

$$\boldsymbol{N}_i = \begin{bmatrix} N_i & 0 \\ 0 & N_i \end{bmatrix}$$

$$\partial\boldsymbol{N}_i = \begin{bmatrix} \frac{\partial N_i}{\partial x} & 0 \\ 0 & \frac{\partial N_i}{\partial y} \\ \frac{\partial N_i}{\partial y} & \frac{\partial N_i}{\partial x} \end{bmatrix}$$

$$\partial\left(\tilde{F}_i^j\boldsymbol{N}_i\right) = \begin{bmatrix} \partial_x(\tilde{F}_i^j N_i) & 0 \\ 0 & \partial_y(\tilde{F}_i^j N_i) \\ \partial_y(\tilde{F}_i^j N_i) & \partial_x(\tilde{F}_i^j N_i) \end{bmatrix}$$

The discretisation performed above is then used to obtain the element matrices and vectors of the system, which are summarised in the following section.

4.8. Summary

In this section, the main equations presented throughout the work regarding the discrete equilibrium equation are summarised.

Discrete equilibrium equation of the system:

$$\boldsymbol{KQ} + \boldsymbol{F}^R + \boldsymbol{F}^D + \boldsymbol{F}^{coh} + \boldsymbol{F}^{bond} + \boldsymbol{F}^C + \boldsymbol{F}^T = \boldsymbol{F}^{ext};$$

Incremental discrete equilibrium equation:

$$\boldsymbol{\mathcal{K}}_n \Delta \boldsymbol{Q}_{n+1} = -\boldsymbol{Re}(\boldsymbol{Q}_n),$$

with:

$$\boldsymbol{Re} = \boldsymbol{KQ} + \boldsymbol{F}^R + \boldsymbol{F}^D + \boldsymbol{F}^{coh} + \boldsymbol{F}^{bond} + \boldsymbol{F}^C + \boldsymbol{F}^T - \boldsymbol{F}^{ext},$$

$$\boldsymbol{\mathcal{K}} = \boldsymbol{K} + \boldsymbol{K}^R + \boldsymbol{K}^D + \boldsymbol{K}^{coh} + \boldsymbol{K}^{bond} + \boldsymbol{K}^C + \boldsymbol{K}^T.$$

The vectors and matrices of the system involved in the above equations are defined as follows:

$$\boldsymbol{K} = \prod_{e=1}^{N_e} \left(\int_{\Omega_e} h \boldsymbol{B}^T \boldsymbol{C} \boldsymbol{B} \, dA \right),$$

$$\boldsymbol{F}^R = \sum_{k=1}^{N_r} \prod_{e=1}^{N_e} \left(\int_{\Gamma_{r,e}^k} A^k \boldsymbol{B}_r^T \boldsymbol{\sigma}^k \, dl \right),$$

$$\boldsymbol{K}^R = \sum_{k=1}^{N_r} \prod_{e=1}^{N_e} \left(\int_{\Gamma_{r,e}^k} A^k \boldsymbol{B}_r^T \boldsymbol{C}^{ed,k} \boldsymbol{B}_r \, dl \right),$$

$$\boldsymbol{F}^D = \prod_{e=1}^{N_e} \left(\int_{\Omega_e} -h \boldsymbol{B}^T \boldsymbol{D} \bar{\boldsymbol{\sigma}} \, dA \right),$$

$$\boldsymbol{K}^D = \prod_{e=1}^{N_e} \left(\int_{\Omega_e} -h \boldsymbol{B}^T \boldsymbol{C}^{ed} \boldsymbol{B} \, dA \right),$$

$$\boldsymbol{F}^{coh} = \sum_{j=1}^{N_c} \prod_{e=1}^{N_e} \left(\int_{\Gamma_{c,e}^j} h \boldsymbol{\mathcal{N}}^{jT} \boldsymbol{R}^j \boldsymbol{\mathcal{T}}^j \, dl \right),$$

$$\boldsymbol{K}^{coh} = \sum_{j=1}^{N_c} \prod_{e=1}^{N_e} \left(\int_{\Gamma_{c,e}^j} h \boldsymbol{\mathcal{N}}^{jT} \boldsymbol{R}^j \frac{\partial \boldsymbol{\mathcal{T}}^j}{\partial \boldsymbol{\Omega}^j} \boldsymbol{R}^{jT} \boldsymbol{\mathcal{N}}^j \, dl \right),$$

$$\boldsymbol{F}^{bond} = \sum_{k=1}^{N_r} \prod_{e=1}^{N_e} \left(\int_{\Gamma_{r,e}^k} \boldsymbol{\mathcal{N}}_r^T \boldsymbol{R}^k \boldsymbol{A}^k \boldsymbol{T}^k \, dl \right),$$

$$\boldsymbol{K}^{bond} = \sum_{k=1}^{N_r} \prod_{e=1}^{N_e} \left(\int_{\Gamma_{r,e}^k} \boldsymbol{\mathcal{N}}_r^T \boldsymbol{R}^k \boldsymbol{A}^k \frac{\partial \boldsymbol{T}^k}{\partial \boldsymbol{\mathcal{W}}^k} \boldsymbol{R}^{k^T} \boldsymbol{\mathcal{N}}_r \, dl \right),$$

$$\boldsymbol{F}^C = \sum_{j=1}^{N_C} \prod_{e=e_C^j} \left(p_{T_C}^j \boldsymbol{G}^{l-t^T} \hat{\boldsymbol{t}} \right),$$

$$\boldsymbol{K}^C = \sum_{j=1}^{N_C} \prod_{e=e_C^j} \left(\boldsymbol{G}^{l-t^T} \hat{\boldsymbol{t}} \frac{\partial p_{T_C}^j}{\partial g_{T_C}^j} \hat{\boldsymbol{t}}^T \boldsymbol{G}^{l-t} \right),$$

$$\boldsymbol{F}^T = \sum_{j=1}^{N_T} \left[\prod_{e=e_S^j} \left(\boldsymbol{\mathcal{N}}_r^T \hat{\boldsymbol{t}} \epsilon_N \hat{\boldsymbol{t}}^T \boldsymbol{\mathcal{N}}_r \boldsymbol{a}_r^t \right) + \prod_{e=e_E^j} \left(\boldsymbol{\mathcal{N}}_r^T \hat{\boldsymbol{t}} \epsilon_N \hat{\boldsymbol{t}}^T \boldsymbol{\mathcal{N}}_r \boldsymbol{a}_r^t \right) \right],$$

$$\boldsymbol{K}^T = \sum_{j=1}^{N_T} \left[\prod_{e=e_S^j} \left(\boldsymbol{\mathcal{N}}_r^T \hat{\boldsymbol{t}} \epsilon_N \hat{\boldsymbol{t}}^T \boldsymbol{\mathcal{N}}_r \right) + \prod_{e=e_E^j} \left(\boldsymbol{\mathcal{N}}_r^T \hat{\boldsymbol{t}} \epsilon_N \hat{\boldsymbol{t}}^T \boldsymbol{\mathcal{N}}_r \right) \right],$$

$$\boldsymbol{F}^{ext} = \prod_{e=1}^{N_e} \left(\int_{\Gamma_{t,e}} h \boldsymbol{N}^T \boldsymbol{t}^* \, dl \right).$$

4.9. Numerical Aspects

This section deals with some special features that must be considered in the numerical implementation of the presented finite element model.

4.9.1. Numerical integration scheme

4.9.1.1. Domain integrals

The integration scheme of the elements intersected by a crack must consider the presence of the crack in order to ensure an adequate integration of the discontinuous functions associated with the enrichments. As the crack is allowed to be arbitrarily oriented in an element, a traditional GAUSSian quadrature, as shown in Figure 4.17 (left), could lead to poor numerical results and even to a linearly dependent system of equations. As can be seen

from the figure, the GAUSS points are poorly distributed and there are even sides of the crack that do not present any integration point.

In order to avoid this problem, MOËS et al. [85] proposed the following numerical integration: the domain of the elements intersected by a crack is divided into triangular sub-domains with their boundaries aligned with the crack geometry, thus ensuring that the sub-domains do not contain any discontinuous function; then a traditional GAUSSian quadrature is used to perform the numerical integration over each of the sub-domains, as well as over the elements that do not contain any crack. In this work, the DELAUNAY triangulation based on Qhull [7] is considered. It should be emphasised that the sub-domains are only necessary for the numerical integration and, therefore, no additional degrees of freedom are associated with them. Furthermore, special care should be taken with those elements with at least one node enriched with the near-tip function. As these functions are not polynomials, a higher order quadrature is required. The integration scheme is illustrated in Figure 4.17 (right). Note the use of a higher quadrature rule for those elements influenced by the near-tip function.

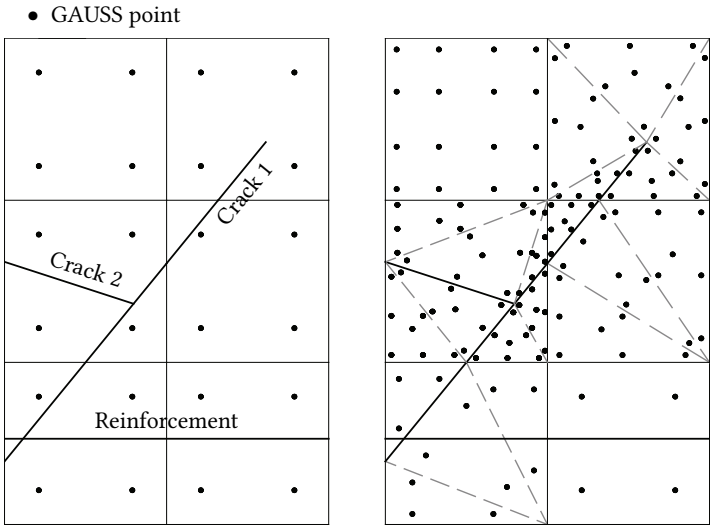

Figure 4.17.: Triangulation and GAUSS points distribution for domain integrals.

Since the reinforcement (both bars and fibres) does not affect the discretisation of the concrete bulk, its presence is not considered in the triangulation.

The formation of new sub-domains as cracks propagate implies an additional problem, namely, the redistribution of the integration points. This situation is illustrated in Figure 4.18 a) and b). The integration scheme requires that the history parameters associated with the loading history of the concrete bulk have to be stored in the integration points. When these are redistributed, the loading history must be then necessarily represented on the new points. This task is achieved by means of a mapping between both distributions. In this work, the history parameters associated with the new configuration are linearly interpolated from the values corresponding to the old one using the interpolation method presented in [3]. This method operates in two steps: first, the set of integration points related to the old configuration (black dots) is triangulated using a DELAUNAY triangulation as shown in Figure 4.18 c), then a piecewise triangular surface is generated over the plane using the respective history parameters as altitudes; secondly, this surface is used within each triangle to interpolate the new values of the history parameter at the new integration points (circles). By way of example, Figure 4.18 d) illustrates the interpolation scheme over the hatched triangle.

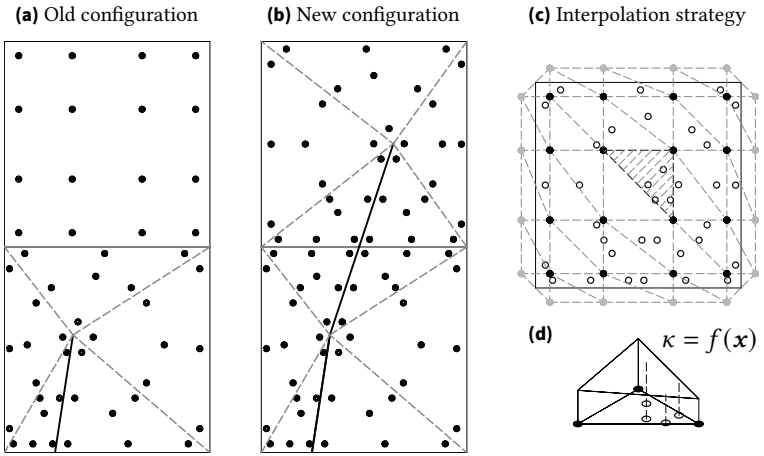

Figure 4.18.: Interpolation scheme of the history parameters associated to the concrete bulk.

4.9.1.2. Line integrals

The evaluation of the line integrals associated with the cohesive cracks and the reinforcement (interfaces included) is also achieved by means of a GAUSSian quadrature rule. In order to accurately compute the integrals, the segments that define the reinforcement/cracks must also be partitioned. The numerical integration is then performed over each one of the sub-segments so generated. The points defining the sub-segments, aside from the original vertices, are:

- intersection points between the reinforcement/cracks and the elements edges,
- intersection points between the cracks and the reinforcement,
- intersection points between the transverse and longitudinal reinforcement,
- and junction points.

A higher order quadrature (at least 4 points) is used on each sub-segment for an adequate integration of the near-tip function associated with the cracks. Figure 4.19 illustrates the integration scheme for different cases.

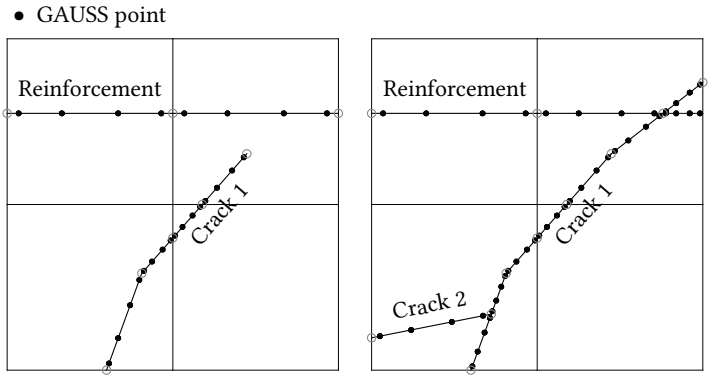

Figure 4.19.: GAUSS points distribution for line integrals.

The numerical integration based on a GAUSSian integration rule may result in spurious oscillations of the cohesive traction field. SCHELLEKENS et al.

[110] have shown, however, that a higher order quadrature, as in this case, can overcome this difficulty[4].

The redistribution of the integration points may also affect the integration scheme associated with the reinforcement/cracks. This situation is illustrated in Figure 4.19. In this case, a similar procedure as described above is applied. The integration points related to the old configuration define sub-segments over which an interpolation curve is generated, then the history parameters associated with the new configuration are interpolated from the curve as shown in Figure 4.20.

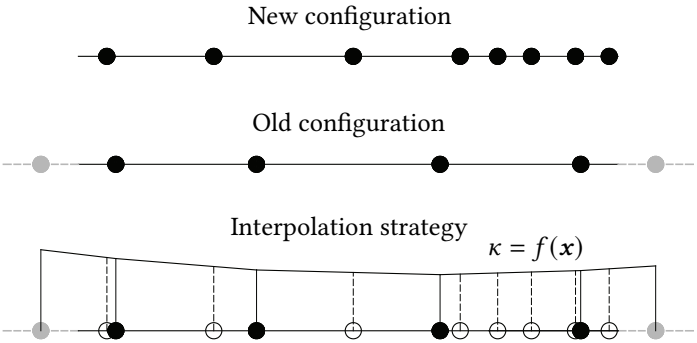

Figure 4.20.: Interpolation scheme of the history parameters associated to the cracks/reinforcement.

4.9.2. Node selection for enrichment

Consider the Figure 4.21 (a), which shows the support of a node (black dot) whose domain is cut by a crack. The node is enriched with the step function $S_i(\boldsymbol{x})$ in order to model the crack. If the area A_2 is too small compared with the area of the nodal support, the enriched shape function $S_i(\boldsymbol{x})N_i(\boldsymbol{x})$ associated with the node under consideration is practically identical in the entire domain of the support to the standard shape function $N_i(\boldsymbol{x})$ (see Figure 4.22)

[4] SCHELLEKENS et al. have also shown that the NEWTON-COTES integration scheme does not suffer from this problem when using a lower order quadrature.

and, therefore, are redundant with each other. This situation could lead to ill-conditioning of the discrete equilibrium equation. The same problem arises when the area A_1 is too small. In general, enrichments based on the step function can generate ill-conditioned systems. In this regard, the junction enrichment suffers from the same problem and must be also considered.

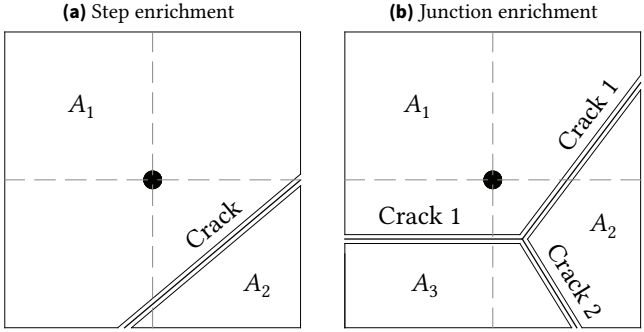

Figure 4.21.: Node selection strategy for enrichment to avoid linear dependency.

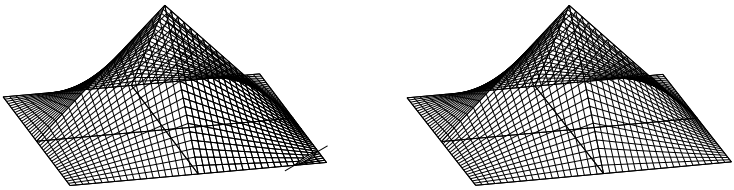

(a) Enriched shape function. **(b)** Standard shape function.

Figure 4.22.: Graphical representation of the standard shape function (a) and the enriched shape function (b) associated with a node whose support is cut by a crack.

This difficulty can be mitigated by eliminating the degrees of freedom, that cause the ill-conditioning, from the discrete system. In this respect, DOLBOW [36] proposed that the nodes having their support almost entirely on one side of the crack (cracks), must be removed from the sets of nodes I_S or I_J. Formally, this can be expressed as:

$$\text{the node under study is removed from the set } I_S \text{ if } \frac{\min(A_1, A_2)}{A_\omega} < tol,$$

or from the set I_J if $\dfrac{\min(A_1, A_2, A_3)}{A_\omega} < tol$,

where A_1, A_2 and A_3 are the areas of the sub-triangles shown in Figure 4.21, and A_ω is the total area of the support of the node. The sub-areas can be easily calculated using the triangulation presented in the previous section. DOLBOW et al. proposed a tolerance of 10^{-4}, which has shown good results.

4.9.3. Kinked cracks

A crack is represented by a series of straight-line segments, which are not necessarily aligned with each other. As the crack grows, new crack segments are added and the initially straight crack may curve, forming a kinked crack. In this case, the crack cannot be correctly modelled by the near-tip function (Equation 4.4), since this predicts a straight discontinuity along $\theta = \pm\pi$ (see Figure 4.3). Therefore, a transformation is required to align the discontinuity modelled by the near-tip function with the actual crack. The transformation presented in [50] is adopted. This transformation can be imagined as virtual rotations that align the crack segments with the segment containing the crack tip, in order to ensure the discontinuity along $\theta = \pm\pi$ in all segments represented by the near-tip function. Figure 4.23 shows a kinked crack modelled with and without the transformation. As can be observed, the transformed near-tip function, unlike the function without transformation, can capture the kinked segments accurately, thus modelling the crack properly.

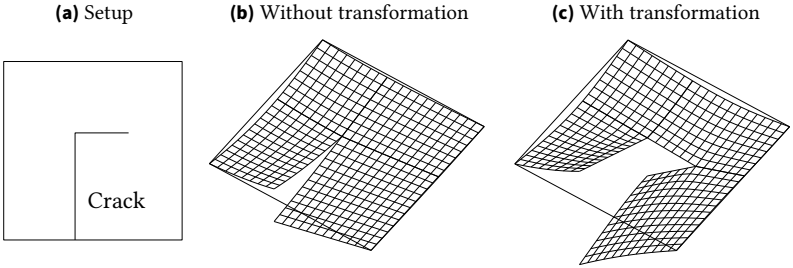

Figure 4.23.: Transformation for a kinked crack.

4.9.4. Non-local stress

In this work, the integral that defines the non-local stress (Equation 3.35) is numerically solved using the same set of GAUSS points and weights involved in the numerical integration of the domain integrals associated with the virtual works. Then, the non-local stress results from the sum of the local stresses $\boldsymbol{\sigma}_i$ at the GAUSS points $\boldsymbol{s}_i(\boldsymbol{x}_i)$, weighted with w_i and the related area A_i[5] according to:

$$\tilde{\boldsymbol{\sigma}} = \left(\sum_{N_G} w_i A_i \right)^{-1} \sum_{N_G} \boldsymbol{\sigma}_i w_i A_i, \tag{4.134}$$

where:

$$w_i = \frac{1}{l\sqrt{2\pi}} \exp\left(\frac{-r_i^2}{4l^2} \right). \tag{4.135}$$

Herein, N_G represents the set of all GAUSS points within the influence radius R around the crack tip $\boldsymbol{x}_t$ ($r_i = \|\boldsymbol{s}_i - \boldsymbol{x}_t\| < R$). Figure 4.24 illustrates the integration strategy.

In the event that a crack completely crosses the circle defined by the influence radius, the GAUSS points located beyond it should not be accounted for when evaluating the non-local stress as shown in Figure 4.25. The crack isolates the regions on both of its sides and, as a consequence, they no longer have an influence on each other. This assumption was also considered by WANG et al. [120] for the non-local formulation of the damage model.

Therefore, the GAUSS points located beyond the crack are to be removed from the set N_G. This can be formalised through the following criterion:

$$\text{the GAUSS point } \boldsymbol{s}_i \text{ is removed from the set } N_G \text{ if } S^2(\boldsymbol{x}_i) S^2(\boldsymbol{x}_t) < 0,$$

where S^2 is step function associated with the crossing crack.

In the numerical simulations, it is common to take advantage of the axes of symmetry (when applicable) and, therefore, only part of the specimens are modelled in order to reduce computational cost. Nevertheless, the part that

[5] These terms correspond to the weights associated with the numerical quadrature.

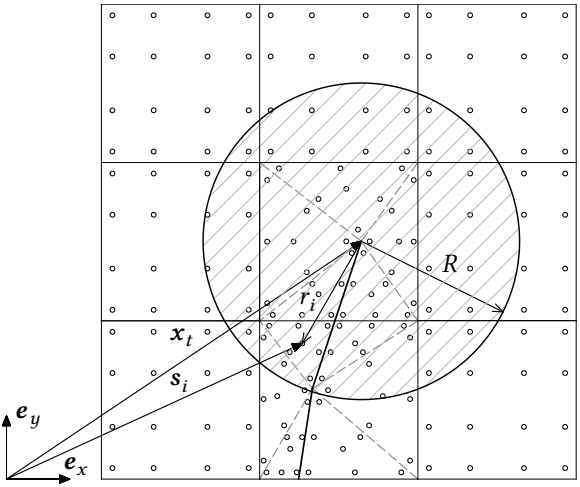

Figure 4.24.: Non-local stress integration strategy.

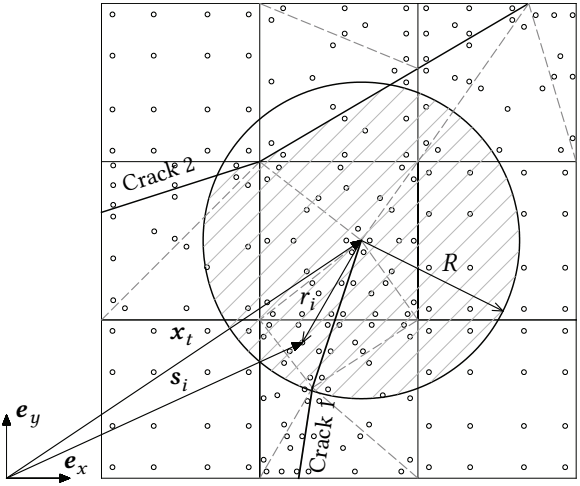

Figure 4.25.: Non-local stress integration strategy for interacting cracks.

was not modelled must be necessarily considered in the estimation of the non-local stress when the influence radius extends beyond the symmetry axis. For this purpose, fictitious GAUSS points, corresponding to the sym-

metrical counterpart of the original GAUSS points, are defined beyond the axis as shown in Figure 4.26. Then, the coordinates of the fictitious point $\bar{\mathbf{s}}_i$, related to the point $\boldsymbol{s}_i$, are given by:

$$\bar{\boldsymbol{x}}_i = \boldsymbol{x}_i + d_i \hat{\boldsymbol{n}}, \tag{4.136}$$

where $\boldsymbol{x}_i$ are the coordinates of the point $\boldsymbol{s}_i$, $\hat{\boldsymbol{n}}$ is the normal unit vector to the symmetry axis and d_i, the minimum distance between $\boldsymbol{s}_i$ and the axis. The area $\bar{A}_i$ and the stress state $\bar{\boldsymbol{\sigma}}_i$ are the same as those of the original GAUSS point, but with the component $\bar{\sigma}_{12}$ being antisymmetric, i.e:

$$\bar{A}_i = A_i, \tag{4.137}$$

$$\{\bar{\sigma}_{11}, \bar{\sigma}_{22}, \bar{\sigma}_{12}\}_i = \{\sigma_{11}, \sigma_{22}, -\sigma_{12}\}_i \,. \tag{4.138}$$

Finally, the set N_G is extended by adding the fictitious GAUSS points satisfying the criterion $\bar{r}_i < R$, and the non-local stress is normally calculated through the Equation 4.134.

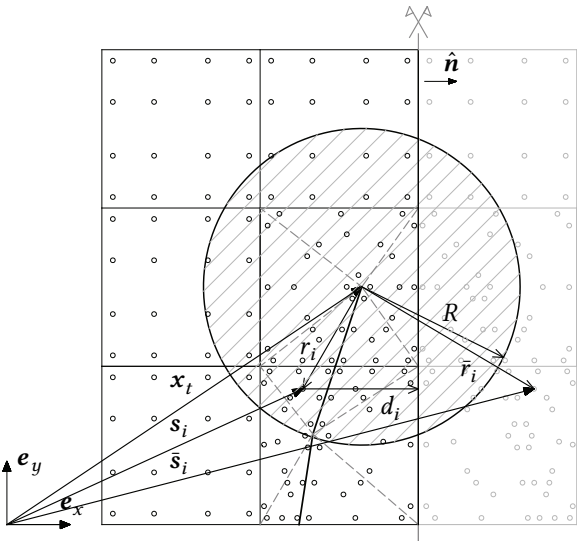

Figure 4.26.: Non-local stress integration strategy for points beyond the symmetry axis.

4.10. Simulation scheme

The key steps for the simulation of fracture in reinforced concrete structures within the framework of the proposed extended finite element formulation are described below. First, the reinforced concrete structure is discretised into finite elements, and the boundary conditions and the parameter defining the material models are specified. Reinforcement and existing cracks are then introduced inside the elements as the union of straight-line segments following the desire geometry and position. A crack will initiate its propagation at a point, at which the initiation criterion is fulfilled. In this work, these points are defined in advance. In this way, not the entire domain is inspected in search of points at which a crack might be initiated, thus reducing computational cost. This is achieved by means of a proper identification of the zones/points that are more susceptible to cracking. These points will be denoted for now on as candidate points. Knowing the reinforcement and cracks distribution, the nodal enrichment is performed as exposed in the previous sections and the topology matrix containing the information of the degrees of freedom belonging to each element is defined. This is used to assemble the global vectors and matrices. Displacements and/or forces are applied to the structure and the response is calculated. After the converged solution is obtained, the criterion for crack initiation is used in each candidate point to evaluate whether a crack initiates its propagation at the point or not. If the criterion is fulfilled, a crack is introduced in the corresponding elements as a straight-line segment of length Δl (with its origin at the candidate point) oriented in the direction of the crack propagation angle θ_p. Likewise, the crack growth criterion is individually evaluated in each crack tip. If the growth criterion is met, the crack will be propagated through the front elements by adding a new straight-line segment of length Δl along the orientation given by the angle θ_p. When a crack reaches the boundary of the structure, its propagation is arrested at the boundary. The near-tip enrichment is then annihilated and replaced by the step enrichment. Once the new crack configuration is established, the nodal enrichment is upgraded. Under the new configuration, the calculated solution does not represent an equilibrium state anymore and, therefore, the response of the current loading step is recalculated. The failure criteria are reevaluated and, if are satisfied, another new crack configuration is obtained. This procedure is repeated until no candidate point/crack fulfills the failure criteria anymore and an equilibrium state is reached. The analysis proceeds then with a new loading step

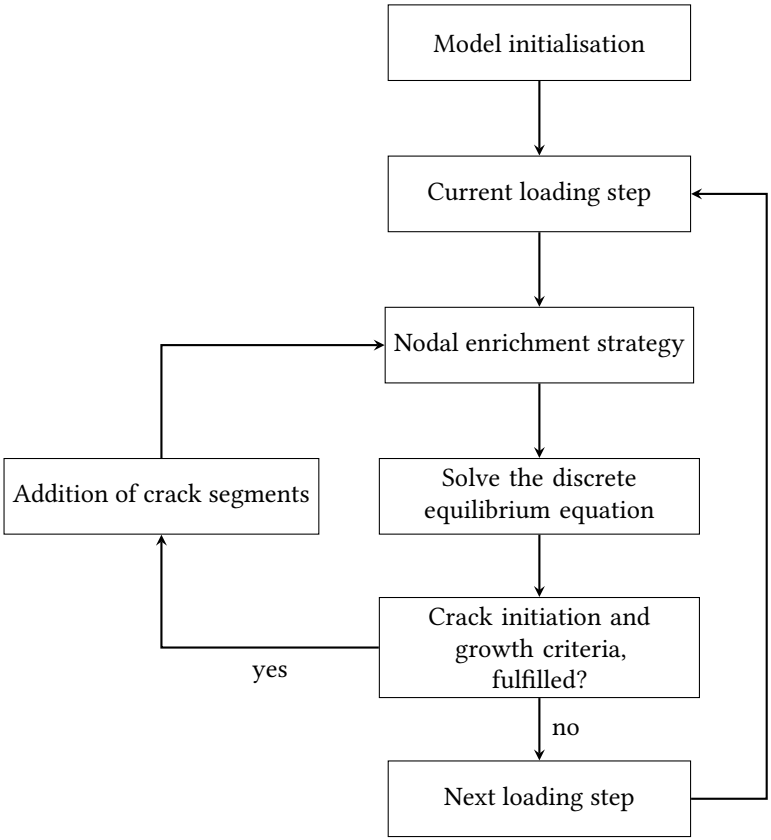

Figure 4.27.: Key steps for the simulation of fracture in RC structures within the proposed formulation.

and the scheme is repeated. A crack is allowed to grow until its coalescence with another crack or its intersection with a structure boundary. The flow chart 4.27 summarises the aforementioned scheme.

5. Numerical examples

In this chapter, the proposed finite element model is applied to simulate some representative tests reported in the literature on reinforced concrete structures. The numerical results are then validated against experimental, numerical and analytical data. The purpose is to demonstrate the effectiveness and applicability of the model, as well as its robustness and performance. The analysed tests are listed below:

- pull-out test on an embedded reinforcing bar,
- single shear pull-out test on an externally bonded sheet,
- RC tensile member,
- tensile member strengthened with steel fibres,
- RC three-point bending beams,
- RC four-point bending beam,
- RC three-point bending beam externally strengthened with CFRP-sheets,
- four-point bending beam strengthened with steel fibres,
- RC walls.

Furthermore, a sensitivity analysis is carried out in order to determinate how sensitive is the numerical model to the finite element discretisation and to the density of candidate points.

5.1. Preliminary considerations

In all numerical simulations, plane stress conditions are considered and loading is applied via prescribed displacements. The numerical integration is carried out using 7 and 3 GAUSS points for the triangular elements (subtriangles included) with and without near-tip enrichment, respectively. For quadrilateral elements, 9 and 4 points are used instead. The line integrals are evaluated using 7 points. The penalty parameter ϵ_N is set to 10^8 N/mm for all penalty formulations. The convergence tolerance β of the incremental iterative procedure is taken to be equal to 0.001.

Regarding the cohesive crack model, the softening functions defined in Equations 3.24 and 3.30 are assumed for all tests. The unloading/reloading path follows a linear relationship to/from the origin, i.e. $k = t_{n\ max}/\kappa$ in Equation 3.29. The shear stiffnesses d_0 and d_1 are considered equal to 1 N/mm and 10^{-4} N/mm, respectively. In the absence of data, the specific fracture energy G_f may be estimated according to [45] from:

$$G_f = G_{f_0} \left(f_c / f_{c_0} \right)^{0.7}, \tag{5.1}$$

where $f_{c_0} = 10$ MPa. G_{f_0} is the base value of the fracture energy, which depends on the maximum aggregate size $d_{\max}$ as given in Table 5.1.

Table 5.1.: Base value of the fracture energy G_{f_0}.

$d_{\max}$ [mm]	G_{f_0} [N/mm]
8	0.025
16	0.030
32	0.058

Likewise, the strain ϵ_{c_3} is evaluated in accordance with [47] if no data is available. The values determined in this way are marked with an asterisk (*) in the tables that summarise the material properties of the concrete.

As stated in Section 3.5, the geometry of the bars, as well as their position and orientation, influence the bond behaviour. For this reason, constitutive bond laws are defined separately for each reinforcement layer. The parameters defining the bond-slip relationship are calculated according the CEB-FIP MODEL CODE 2010 for good bond conditions. The clear distance between

ribs is estimated as follows: $c_{clear} = 0.4\phi$, if no information is available. For the stirrups (transverse bars), a pull-out failure is assumed. In all cases, $\alpha = 0.4$ as stated in the code.

For the evaluation of the tangent matrices $\boldsymbol{K}^{coh}$ and $\boldsymbol{K}^{bond}$, the tangent stiffness matrices $\partial\boldsymbol{\mathcal{T}}/\partial\boldsymbol{\Omega}$ and $\partial\boldsymbol{T}/\partial\boldsymbol{\mathcal{W}}$ are replaced by the secant stiffness matrices $\boldsymbol{\mathcal{T}}/\boldsymbol{\Omega}$ and $\boldsymbol{T}/\boldsymbol{\mathcal{W}}$, respectively, since this approach leads to a most stable convergence[1]. These are defined in terms of the secant moduli as:

$$\frac{\boldsymbol{\mathcal{T}}}{\boldsymbol{\Omega}} = \begin{bmatrix} \frac{t_n}{\omega_n} & 0 \\ \frac{t_s}{\omega_n} & \frac{t_s}{\omega_s} \end{bmatrix}, \tag{5.2}$$

$$\frac{\boldsymbol{T}}{\boldsymbol{\mathcal{W}}} = \begin{bmatrix} \frac{\sigma}{w} & 0 \\ 0 & \frac{\tau}{s} \end{bmatrix}. \tag{5.3}$$

The non-local stress is calculated using an influence radius $R = 2.25l_c$ as proposed by HETTICH [56] and a length $l = 3l_c$, where l_c is the characteristic length of the element containing the crack tip. The characteristic length is considered to be equal to the distance from the element centroid to the most distant element node.

Furthermore, each new added straight-line segment is considered to have a length Δl equal to the characteristic length of the element containing the crack tip or the candidate point under consideration.

The finite element meshes used in the simulations, as well as their corresponding candidate points (red circles), are shown in Appendix A. As can be seen, the candidate points are defined at the structure edges that are more susceptible to tensile failure due to crack formation.

[1] During the preliminary numerical simulations, the tangent matrices evaluated by means of the tangent stiffness matrices leaded to convergence difficulties. In most cases, the solution diverged. These difficulties are avoided using the secant stiffness matrices.

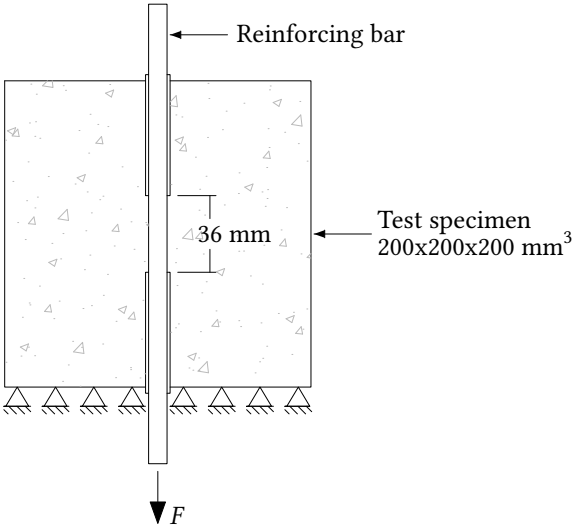

Figure 5.1.: Test setup of the pull-out test performed by LETTOW [70]. All dimensions in millimetres.

5.2. Pull-out tests

5.2.1. Embedded reinforcing bars

The first example deals with one of the pull-out tests performed by LETTOW [70]. The test specimen corresponds to a cube with 200 mm sides with an embedded steel bar of 12 mm diameter subjected to a pull-out load. The reinforcing bar is positioned at the centre of the specimen with an embedment length of $3\phi = 36$ mm. This length prevents the yielding of the bar before its pull-out. The test setup is illustrated in Figure 5.1. The mechanical properties of the reinforcing bar are $E = 200000$ MPa and $\nu = 0.3$, while for the concrete are $E = 26287$ MPa and $\nu = 0.2$.

The finite element model is built with 980 4-nodes quadrilateral elements as shown in Figure 5.2. The bar (blue line) is extended over supplementary elements, which serve as support for the modelling of the bar outside the concrete bulk and allow the application of the load to the bar. Two elements are defined in this way, namely, a load element (light grey element) and an

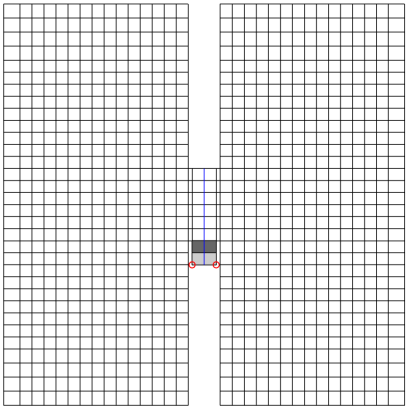

Figure 5.2.: Finite element mesh of the pull-out test (980 4-nodes quadrilateral elements).

empty element (dark grey element). The prescribed displacements are applied to the load element (on the nodes marked with red circles). The rest of the elements correspond to the concrete bulk (including those elements crossed by the crack). Perfect bond is assumed within this element, thus ensuring that both the bar and the element act monolithically. In order to guarantee that the forces are transferred to the concrete exclusively through the reinforcing bar, an element without stiffness (empty element) is placed between the load element and a concrete bulk element. The stiffness is neglected by setting the thickness h or the modulus E equal to 0. Additionally, the bond must be also negligible along the empty element. This procedure is employed in all tests in which the load is applied directly to the reinforcement. The compressive failure of concrete is not considered in this test.

The parameters that define the bond stress-slip relationship are the same used by LETTOW and are presented in Table 5.2. The normal relative displacement w is assumed to be negligible.

Table 5.2.: Parameters for the bond stress-slip relationship (pull-out test).

s_1 [mm]	s_2 [mm]	s_3 [mm]	τ_{max} [MPa]	τ_f [MPa]
0.77	1.37	7.5	11.5	4

The global response of the specimen can be also analytically obtained by solving the differential equation that governs the bond behaviour [103][2]. In Figure 5.3, the computed response, given in terms of the applied load as function of the slip (equal to the prescribed displacement), is compared with the experimental and analytical solution. The results are in good agreement. Moreover, the analytical and numerical curves are almost identical, showing that the X-FEM approach can be used as an alternative for the modelling of embedded reinforcing bars.

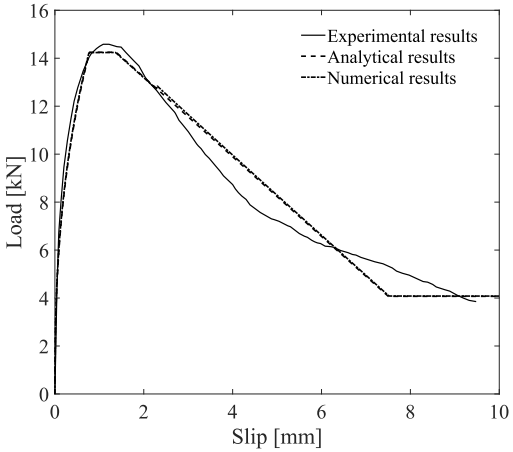

Figure 5.3.: Slip versus applied load curve (pull-out test).

5.2.2. Externally bonded reinforcement

The use of the HEAVISIDE enrichment for the modelling of bonded reinforcement is validated by means of a Single Shear Pull-Out Test (SSPOT). The test comprises a concrete block with one FRP sheet bonded on one of its sides as shown in Figure 5.4. The sheet has a width of 40 mm and a thickness of 0.05 mm. The dimensions of the specimen are chosen in such a way as to ensure the maximum bonded length. The modulus of elasticity and the POISSON's

[2] A more detailed description can be found in [**Walendy2019**, 5]

ratio of the concrete block are 26287 MPa and 0.2, respectively; while for the FRP sheet these are equal to 100000 MPa and 0.3, respectively.

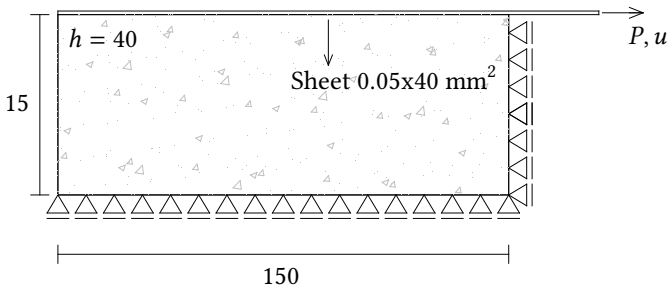

Figure 5.4.: Test setup of the single shear pull-out test. All dimensions in millimetres.

The model is built with 1002 4-nodes quadrilateral elements. The parameters defining the bond stress-slip relationship are summarised in Table 5.3. The compressive failure of concrete is not considered in this test.

Table 5.3.: Parameters for the bond stress-slip relationship (SSPOT).

s_1 [mm]	s_2 [mm]	τ_{max} [MPa]
0.5	1.0	1.0

The force transferred to the system is plotted as a function of the displacement prior to debonding of the sheet in Figure 5.5. As can be seen, the numerical results agree with the analytical results almost perfectly, both in the linear-elastic and the softening branch. As in the case of the reinforcing bar, the analytical solution can be obtained from the differential equation that governs the bond behaviour [**Walendy2019**, 5, 103].

Figures 5.6 and 5.7 show the slip and bond stress profiles along the bonded length at maximum load, where an excellent agreement between the numerical and analytical results is observed. The proposed alternative can reproduce the expected behaviour quit well.

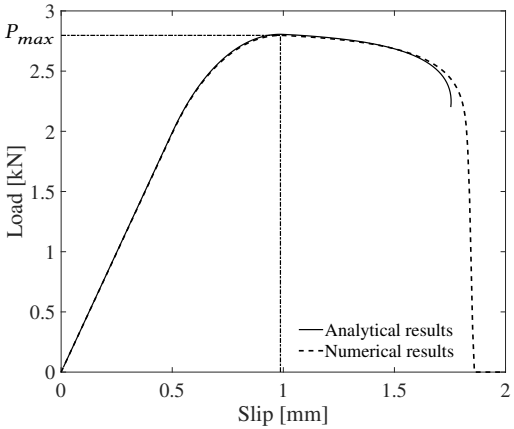

Figure 5.5.: Slip versus applied load curve (SSPOT).

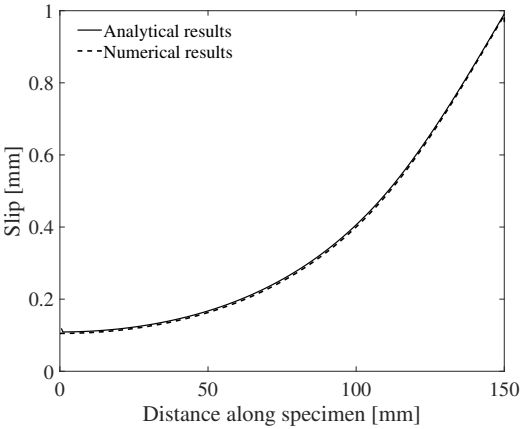

Figure 5.6.: Slip profile at maximum load (SSPOT).

5.3. Tensile members

5.3.1. RC tensile member STS12

This numerical simulation corresponds to the tensile member STS12 tested by WU et al. [124]. The specimen consists of a 100x100x1100 mm^3 concrete

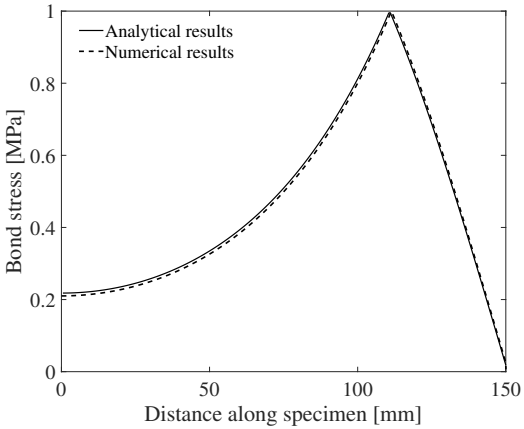

Figure 5.7.: Bond stress profile at maximum load (SSPOT).

prism reinforced with a single reinforcing bar placed at the centroid of the cross section as shown in Figure 5.8. The bar is subjected to a monotonically increasing deformation up to its yielding.

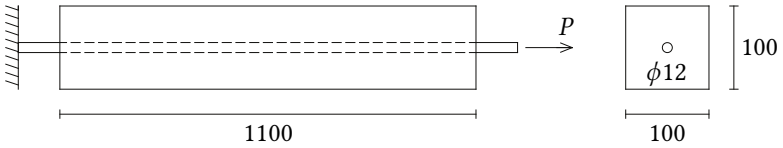

Figure 5.8.: Test setup of the RC tensile member STN12 tested by WU et al. [124]. All dimensions in millimetres.

The mechanical properties according to the authors are summarised in Tables 5.4 and 5.5 .

Table 5.4.: Mechanical properties of the concrete (STN12).

E [GPa]	ν	f_c [MPa]	f_t [MPa]	G_f [N/mm]
22.4	0.2	21.6	2.04	0.051*

The model is built with 670 4-nodes quadrilateral elements. Due to the symmetry conditions, only half of the test specimen is modelled. In order to avoid shear interlocking, the reinforcing bar is treated as an externally bonded re-

Table 5.5.: Mechanical properties of the reinforcement (STN12).

E [GPa]	ν	f_y [MPa]
200	0.3	520

inforcement with the total cross area A, and the contact areas A_n and A_t reduced by half. The parameters that define the bond stress-slip relationship are summarised in Table 5.6. The compressive failure of concrete is not considered in this test.

Table 5.6.: Parameters for the bond stress-slip relationship (STN12).

s_1 [mm]	s_2 [mm]	s_3 [mm]	τ_{max} [MPa]	τ_f [MPa]
1	2	5	11.61	4.64

A comparison of the experimental and numerical applied load vs average strain curves is shown in Figure 5.9. The measured average strain was calculated as the quotient between two points on opposite sides of the specimen divided by the distance between them (890 mm). The numerical average strain is determined in a similar fashion. A good agreement between the results is observed. The model can accurately capture the initial stiffness increment and its further degradation once cracking starts.

Every drop in the curves is related to the formation of a crack. The model predict 5 primary cracks, which is in an excellent agreement with the experimental results. The numerical model provides also excellent results in terms of both the time at which cracks onset during the loading process and the spacing between them. Figure 5.10 compares the numerical and experimental crack pattern at the time of failure.

Table 5.7 summarise the predicted and experimental average and maximum crack width at the load stages 40 kN and 50 kN. Each crack width calculated by the numerical model is obtained as the average opening along the crack.

Figure 5.11 shows the force distribution in the steel bar along the member at two different load stages (40 kN and 50 kN). The variation of steel forces along the specimen predicted by the numerical model is in good agreement with the measured variation, being this able to reproduce the expected behaviour. It can be seen in the figures that the steel force reaches its maxi-

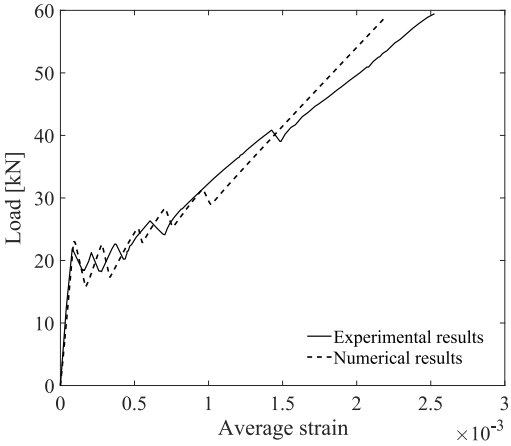

Figure 5.9.: Average strain versus applied load curve (STN12).

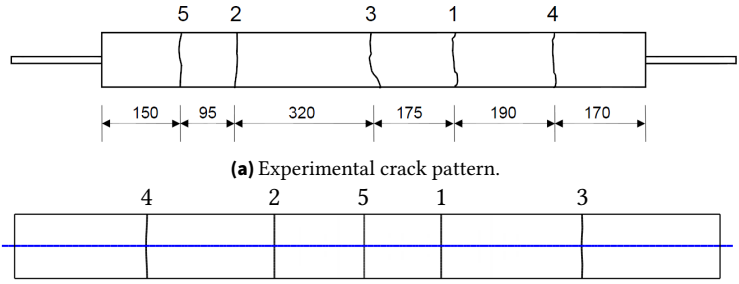

(a) Experimental crack pattern.

(b) Computed crack pattern.

Figure 5.10.: Final crack pattern (STN12).

Table 5.7.: Crack widths at different load stages (STN12).

	Average crack width [mm]		Maximun crack width [mm]	
Load stage	Experiment	Present	Experiment	Present
40 kN	0.185	0.244	0.300	0.255
50 kN	0.200	0.312	0.375	0.330

mums (equal to the current applied force) at the cracks, and its minimums at the mid-way between them, which match well with the observations.

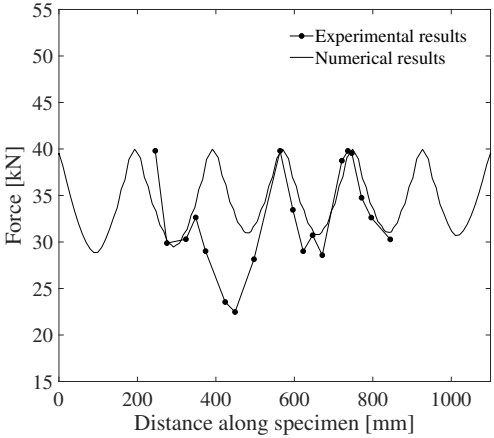

(a) $P = 40$ kN.

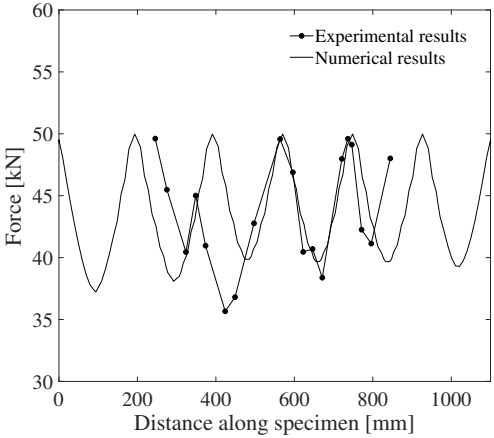

(b) $P = 50$ kN.

Figure 5.11.: Steel force profile at different stages of loading (STN12).

5.3.2. Fibre reinforced uniaxial tensile member

Bending and uniaxial tensile tests on concrete members reinforced with steel fibres were performed by SORELLI et al. [112]. Two different types of steel

fibres were tested in four different combinations. This work focuses on the analysis of the specimens strengthened with 30 kg/m^3 (corresponding to a volume fraction of 0.38%) of fibres of 0.18 mm in diameter and 12 mm long randomly distributed.

In this particular example, the uniaxial test is analysed. The test specimen corresponds to a concrete prism with a central notch reinforced with steel fibres. The geometry and the loading conditions are shown in 5.12. The thickness of the prisms is equal to 40 mm. The notch has a depth of 15 mm and a width of 4 mm. The results concerning one of the bending tests are presented later in this chapter.

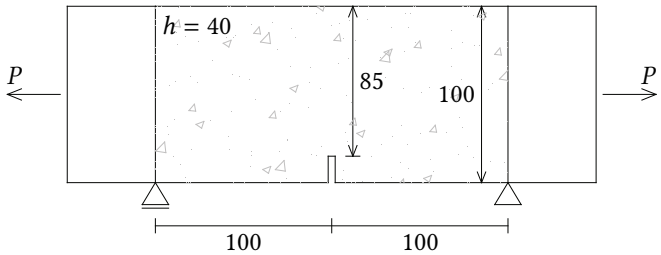

Figure 5.12.: Test setup of the uniaxial test performed by SORELLI et al. [112]. All dimensions in millimetres.

Due to the high sensitivity of the global response of the structure to the number of fibres in the cracked section, the authors have also reported the average fibre density in this area (number of fibres in the cracked section per unit area), corresponding to 3.02 fibres/cm^2. This last value is used in the analysis. The modulus of elasticity and the POISSON's ratio of the fibres are equal to 210000 MPa and 0.3, respectively. The mechanical properties of the concrete used in the numerical simulation are summarised in Table 5.8. Only the modulus of elasticity and the compressive strength were reported by SORELLI et al., the rest of the parameters were determined by means of the best fitting procedure on the test response for plain concrete conditions.

Table 5.8.: Mechanical properties of the concrete (uniaxial test).

E [GPa]	ν	$f_{c,cube}$ [MPa]	f_t [MPa]	G_f [N/mm]
25.1	0.2	28.3	2.6	0.1

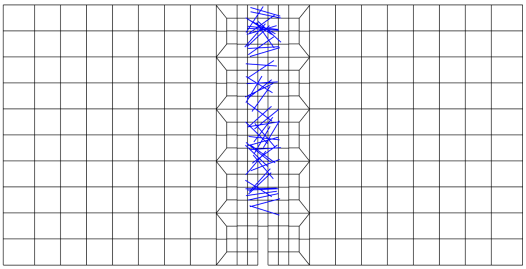

Figure 5.13.: Finite element mesh of the uniaxial test (317 4-nodes quadrilateral elements).

The finite element model is built with 317 4-nodes quadrilateral elements. The finite element mesh and the fibres orientation are shown in Figure 5.13. Considering that the crack is initiated at the notch tip and grows across the centre of the specimen, only the fibres located within this zone are modelled, since only these are going to be activated as the crack propagates. The number of fibres distributed along the cracked section, according to the fibre density given above, is about 102. Only half of them are explicitly modelled in order to reduce computational cost. The rest is included in the total cross area of each fibre by taking the amount of reinforcement rods n_ϕ equal to 2. The bond law is defined according to the parameters indicated in Table 5.9, which were also determined via a best fitting procedure. The compressive failure of concrete is not considered in this test.

Table 5.9.: Parameters for the bond stress-slip relationship (uniaxial test).

s_{max} [mm]	α	τ_{max1} [mm]	τ_{max2} [MPa]	τ_f [MPa]
0.01	20	5	3	2.25

Figure 5.14 shows the response of the prism in terms of the applied load and the Crack Tip Opening Displacement (CTOD). Likewise, Figure 5.15 illustrates the response the unstrengthened prism (plain concrete). The experimental results are depicted in the figure as the region between the solid black lines. It can be noticed that both the cohesive and bond laws provide a good fit for the experimental results.

The influence of the fibre orientation and fibre volume on the global response of the uniaxial test analysed above is compared in Figure 5.16. The measured response is also illustrated. The same test setup and material parameters are

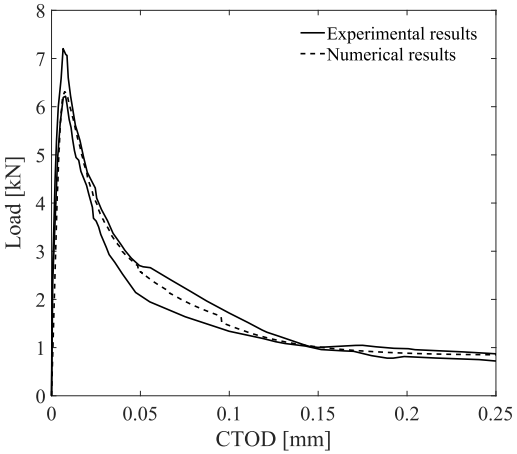

Figure 5.14.: Displacement versus applied load curve (strengthened uniaxial test).

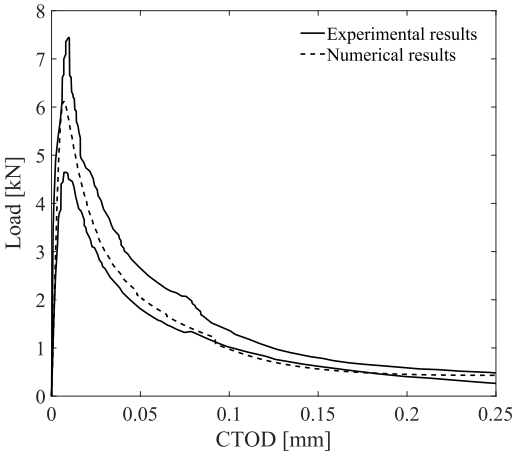

Figure 5.15.: Displacement versus applied load curve (unstrengthened uniaxial test).

then used. Five fibres configurations are considered: fibres oriented at an angle of 0°, 45° and 90° with respect to the horizontal axis, having the same fibre volume as from the original test; and fibres with the double and half of the measured fibre volume oriented according to the original distribution.

As can be seen, the specimen behaves stiffer with increasing fibre volume. On the other hand, as the fibres align with the crack, their influence on the structure is reduced to the point where, at an angle of 90°, the prism behaves as its unstrengthened counterpart (the curve of the plain concrete test is in fact overlapped with the curve related to the test with the fibres aligned with the crack). The model can reproduce quite well the expected behaviour.

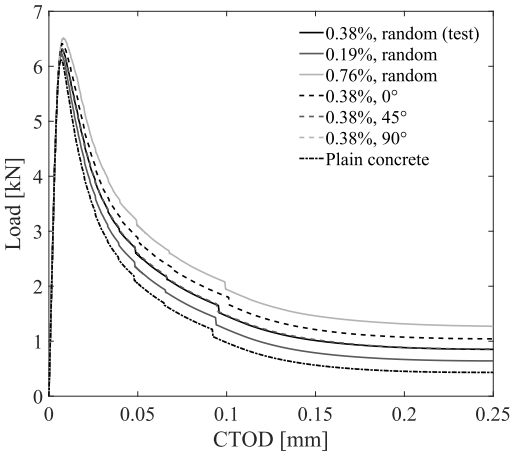

Figure 5.16.: Influence of fibre volume and orientation on the global response of the uniaxial test.

5.4. Beams

5.4.1. RC three-point bending beams T5A1 and T6A1

The tests correspond to the three-point bending beams T5A1 and T6A1 conducted by BOSCO et al. [22], which comprise simply supported beams subjected to a monotonically increasing load P at their centres. The test setup and the dimensions of the specimens are illustrated in Figure 5.17. The beams differ only in the amount of tensile reinforcement. Hence, specimen T5A1 was tested up to the failure of the lower reinforcement, while specimen T6A1, to the failure due to concrete crushing.

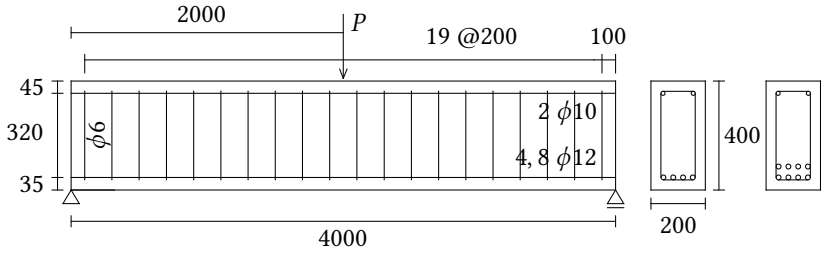

Figure 5.17.: Test setup of the RC beams T5A1 and T6A1 tested by BOSCO et al. [22]. All dimensions in millimetres.

The material properties are taken from [2, 99] and are listed in Tables 5.10 and 5.11.

Table 5.10.: Mechanical properties of the concrete (T5A1 and T6A1).

E [GPa]	ν	f_c [MPa]	f_t [MPa]	G_f [N/mm]	ϵ_{c_3} [%]
28	0.2	32	2.5	0.1	−2.3

Table 5.11.: Mechanical properties of the reinforcement (T5A1 and T6A1).

E [GPa]	ν	f_y [MPa]	f_u [MPa]	H [MPa]
200	0.3	587	672	829

The model is built with 1282 4-nodes quadrilateral elements. Due to the symmetry conditions, only half of the test specimen is modelled.

Table 5.12.: Parameters of the bond stress-slip relationship (T5A1 and T6A1).

	s_1 [mm]	s_2 [mm]	s_3 [mm]	τ_{max} [MPa]	τ_f [MPa]
ϕ12	0.43	0.43	2.4	9.39	3.76
ϕ10	1	1	2	13.18	5.28
ϕ6	1	1	2.4	16.77	6.71

In Figure 5.18, the numerical and experimental load vs mid-displacement curves are compared, where a good agreement between the results can be observed. Regarding the specimen T5A1, the predicted response agrees reasonably well with the experimental results. The numerical model predicts likewise a fracture of the lower reinforcing bar, however, at a higher load

and deflection. The computed and experimental ultimate failure loads are 112.1 kN and 100.9 kN, respectively. With respect to the specimen T6A1, the numerical model can capture very well the ascending part of the curve, but fails to estimate the onset of yielding, underestimating the beginning of the plastic range. Due to the limitations present in the damage model exposed in Section 3.3 regarding the stress-strain relationship, the numerical model is not capable of predicting compressive failure. Therefore, the model is loaded up to the displacement at which concrete crushing starts in the specimen (~ 68 mm).

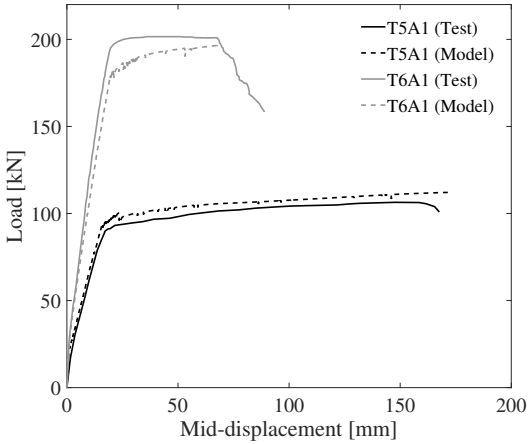

Figure 5.18.: Mid-displacement versus applied load curve (T5A1 and T6A1).

Figures 5.19 and 5.20 show the predicted and observed final crack patterns. The location and orientation of the predicted cracks are in good agreement with the experimental results. In both the tests and the numerical models, the difference in the amount of reinforcement causes different crack patterns. With a lower degree of reinforcement (T5A1), the beam response is characterised mainly by the presence of flexural cracks, whereas, with double the amount (T6A1), by the onset of inclined shear cracks. Furthermore, as can be seen in the measured pattern, some cracks abruptly change their curvature as they propagate. This behaviour can be reasonably reproduced by the model.

In Figure 5.21, the axial stress of the lower bar is shown at different load stages (displacements). As can be observed, the stress increases gradually

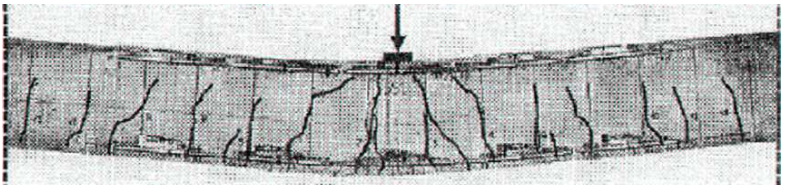

(a) Experimental crack pattern.

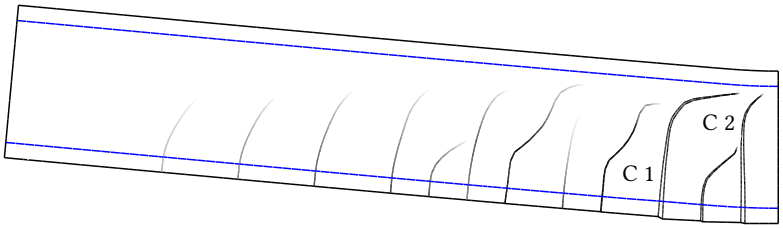

(b) Computed crack pattern.

Figure 5.19.: Final crack pattern (T5A1).

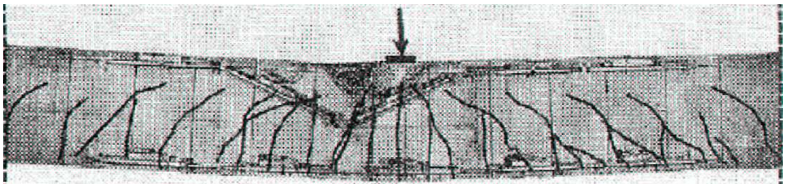

(a) Experimental crack pattern.

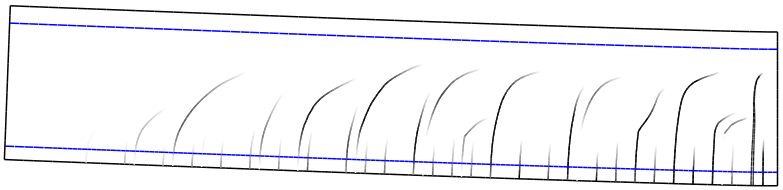

(b) Computed crack pattern.

Figure 5.20.: Final crack pattern (T6A1).

as the load increases until the yield strength is exceeded. Beyond this point, the reinforcement exhibits some degree of hardening, accompanied by large plastic strains, until tensile failure occurs. The stress peaks are reached at

the main cracks. The plastic response of the reinforcing bars can be nicely replicated by the numerical model.

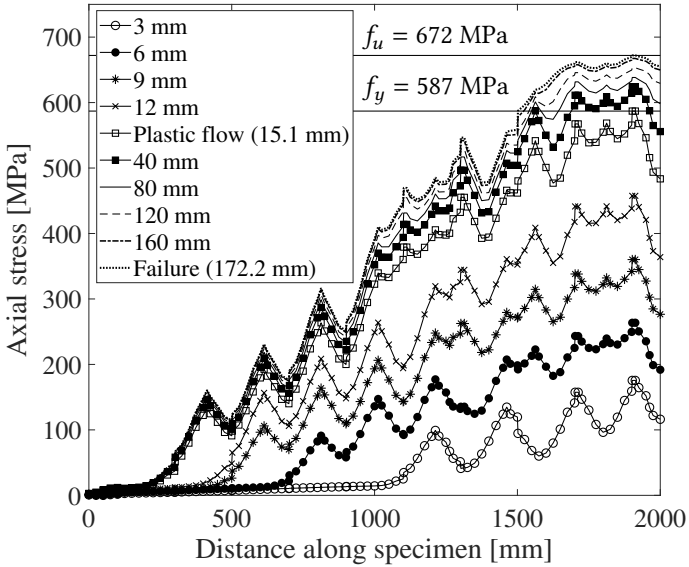

Figure 5.21.: Axial stress profile of the lower bar at different load stages (T5A1).

Figure 5.22 illustrates the evolution of the predicted crack opening of the two wider cracks (see Figure 5.19), measured at the concrete surface, as the load increases. The maximum crack widths reached are equal to 11.0 mm and 11.3 mm for the crack 1 and 2, respectively. It should be noted that the ultimate tensile strength in the bar is reached at the widest crack (crack 2).

Figure 5.23 shows the local slip and bond stress profiles along the lower bar at the time of failure, where the large slip values and the deterioration of the bond strength in the plastic zone are plain to see.

5.4.2. RC four-point bending beam

The following simulation corresponds to the simply supported beam performed by JASON et al. [62] under four point bending. Two identical specimens were tested. Therefore, the experimental results are taken from the

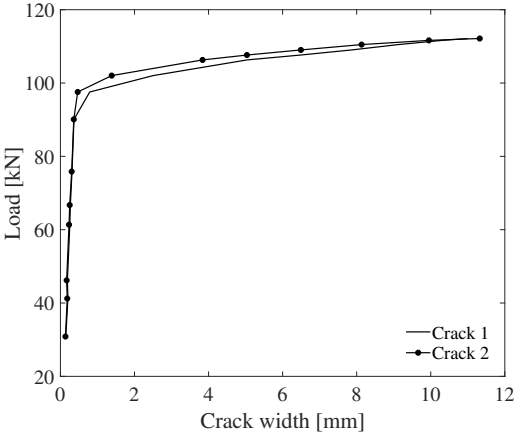

Figure 5.22.: Crack width history of the main cracks (T5A1).

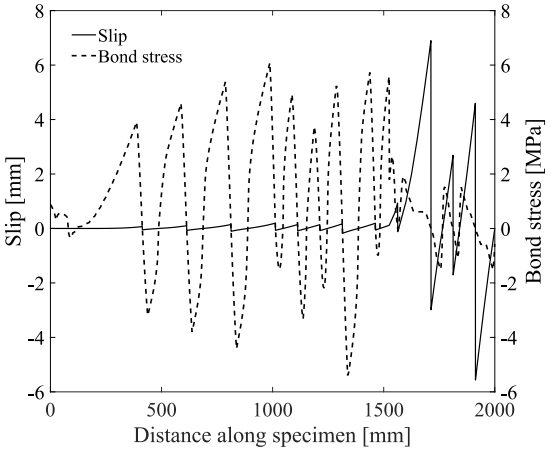

Figure 5.23.: Slip and bond stress profiles of the lower bar at the time of failure (T5A1).

mean values. Figure 5.25 illustrates the beam dimensions, reinforcing detailing and test setup. There are no stirrups in the pure bending zone in order to avoid any perturbation in the crack pattern.

The finite element model is built with 1080 4-nodes quadrilateral elements. Due to the symmetry conditions, only half of the test specimen is modelled.

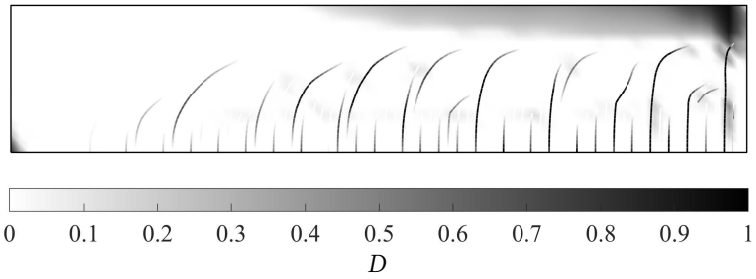

Figure 5.24.: Compressive failure pattern (T6A1).

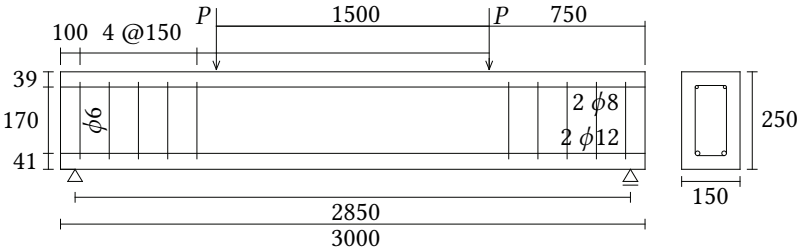

Figure 5.25.: Test setup of the RC four-point bending beam tested by JASON et al. [62]. All dimensions in millimetres.

The reinforcing steel and concrete properties according to the authors are given in Tables 5.13 and 5.14, while the parameters that define the bond stress-slip relationship are summarised in Table 5.15.

Table 5.13.: Mechanical properties of the concrete (4PBT).

E [GPa]	ν	f_c [MPa]	f_t [MPa]	G_f [N/mm]	ϵ_{c_3} [%]
29.8	0.2	39	2.5	0.1	-2.4^*

Table 5.14.: Mechanical properties of the reinforcement (4PBT).

E [GPa]	ν	f_y [MPa]	f_u [MPa]	H [MPa]
190	0.3	550	590	828

The global response of the beam is shown in Figure 5.26 in terms of the total applied load as function of the vertical displacement at the top mid-span. A

Table 5.15.: Parameters of the bond stress-slip relationship (4PBT).

	s_1 [mm]	s_2 [mm]	s_3 [mm]	τ_{max} [MPa]	τ_f [MPa]
$\phi 12$	0.47	0.47	0.57	11.58	0.12
$\phi 8$	0.87	0.87	1.05	14.8	0.15
$\phi 6$	1	2	2.4	15.61	6.24

good agreement between the numerical (present) and experimental results is observed, in both the elastic and post-cracking branch. The present model slightly overestimates the onset of cracking as well as the displacement at the ultimate load (plastic flow). By way of comparison, the numerical results obtained by JASON et al. [62] using a damaged plasticity model are also presented.

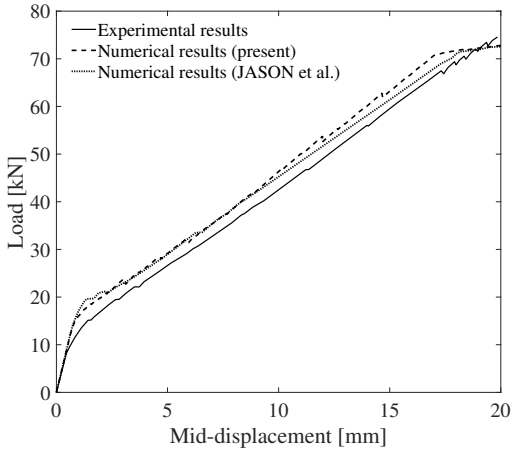

Figure 5.26.: Load-displacement response (4PBT).

Figure 5.27 compares the deformed shapes along the pure bending zone at the load of 36 kN. The vertical displacements were measured through twenty sensors located at 35 mm from the bottom. The predicted values are calculated at the same locations. Due to the fact that the numerical model behaves stiffer than the test specimen, the 36 kN are reached at a lower mid-displacement and, therefore, the numerical deformed shape is higher. At the same mid-displacement, the present model provides a closer agreement than the model used by JASON et al.

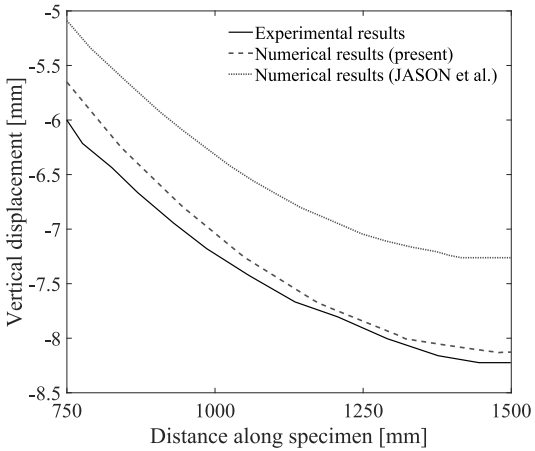

Figure 5.27.: Deformed shape at the load of 36 kN (4PBT).

Image correlation technique were used by JASON et al. within the pure bending zone to obtain precise information concerning the cracking properties. In this regard, Figure 5.28 depicts the computed crack pattern (at the load stage 36 kN), which agrees reasonably well with the experimental pattern. Note that the symmetry of the model is used to represent the predicted crack pattern. Due to the constant moment within this zone, the cracks follow a straight path as the load increases. 12 cracks are predicted compared with the 12.5 obtained in the test. The experimental value corresponds to the mean values measured on the two tested beams. For this reason a non integer number is obtained.

Table 5.16 summarises the computed and experimental crack widths (average and maximum values) as well the average spacing and the number of cracks at three characteristic load stages (20 kN, 25 kN and 36 kN). Cracking begins to occur early in the test and, at a load of 20 kN, the specimen has already 10 cracks compared with the 6 predicted by the model, which results in a big discrepancy between the data. However, the differences tend to decrease as the load increases and the present model provides a closer agreement in the last stages.

Figure 5.29 shows a comparison between the experiment and the simulation on the horizontal displacement along the specimen within the pure bending

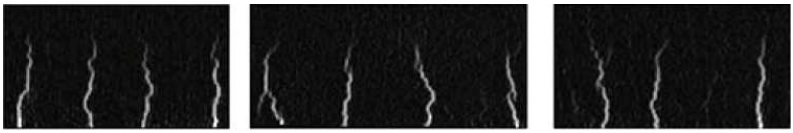

(a) Experimental crack pattern.

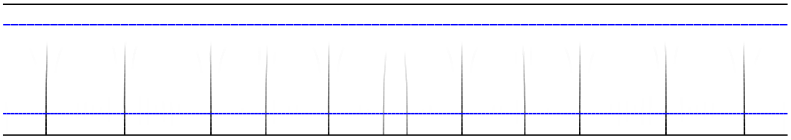

(b) Computed crack pattern.

Figure 5.28.: Crack pattern at the load of 36 kN (4PBT).

Table 5.16.: Crack properties (4PBT).

	No. of Cracks		Avg. value [mm]		Max. value [mm]		Avg. spacing [mm]	
Load stage	Exp.	Present	Exp.	Present	Exp.	Present	Exp.	Present
20 kN	10	6	0.054	0.106	0.114	0.115	160	265
25 kN	10.5	10	0.100	0.127	0.188	0.164	155	147
36 kN	12.5	12	0.186	0.197	0.298	0.249	110	120

zone. The jumps along the curve can be identified with the cracks opening. The computed curves agree well with the experimental results.

5.4.3. RC three-point bending beam VVBS3

Specimen VVBS3 was conducted by ZILCH et al. [132] as a three-point bending test. The test setup with the corresponding dimensions is shown in Figure 5.30. The beam was strengthened in flexure with a CFRP sheet, with a width and a thickness of 100 mm and 1.4 mm, respectively. The sheet was externally bonded to the concrete surface using an epoxy resin, 100 mm from the supports axis.

A summary of the mechanical properties for concrete and reinforcing steel according to the authors is given in Tables 5.17 and 5.18. The modulus of elasticity and the POISSON's ratio of the CFRP sheet are 170800 MPa and 0.3, respectively. The parameters for the bond-slip relationship (for both reinforcing bars and the sheet) are listed in Table 5.19. The finite element model

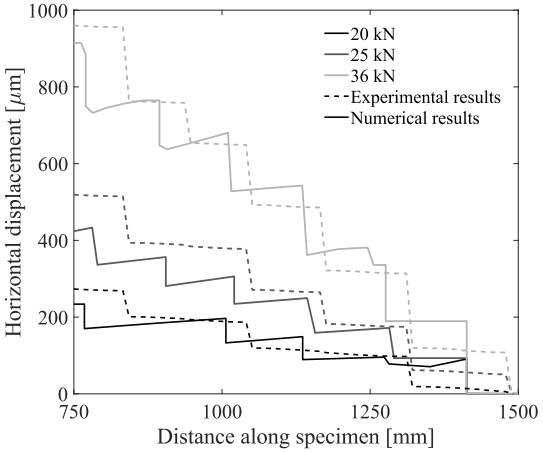

Figure 5.29.: Horizontal displacements along the pure bending zone (4PBT).

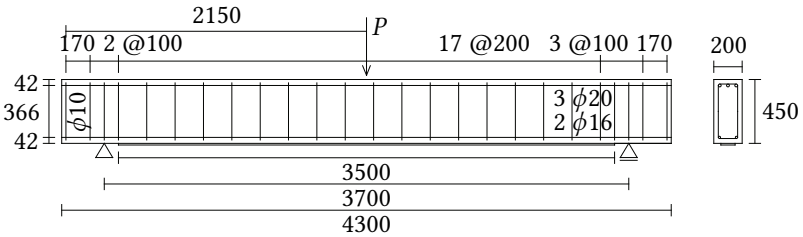

Figure 5.30.: Test setup of the RC beam VVBS3 tested by ZILCH et al. [132]. All dimensions in millimetres.

is built with 1551 4-nodes quadrilateral elements. Symmetry conditions are used.

Table 5.17.: Mechanical properties of the concrete (VVBS3).

E [GPa]	ν	f_c [MPa]	f_t [MPa]	G_f [N/mm]	ϵ_{c_3} [%]
24	0.2	28.2	2.9	0.052*	−2.3*

The ARAMIS measuring system of the GOM company was used to continuously measure both the deformed shape and the crack pattern over time. Furthermore, 20 strain gauges were attached along the sheet length in order

Table 5.18.: Mechanical properties of the reinforcement (VVBS3).

	E [GPa]	ν	f_y [MPa]	f_u [MPa]	H [MPa]
$\phi 16$	203.3	0.3	510	646.5	1085
$\phi 20$	204	0.3	513.3	616.2	810
$\phi 10$	196.6	0.3	445.6	572.6	1669

Table 5.19.: Parameters of the bond stress-slip relationship (VVBS3).

	s_1 [mm]	s_2 [mm]	s_3 [mm]	τ_{max} [MPa]	τ_f [MPa]
$\phi 16$	0.72	0.72	6.4	11.54	4.61
$\phi 20$	0.36	0.36	8	8.72	3.49
$\phi 10$	1	2	4	13.27	5.31
Sheet	0.02	0.25	–	6.47	–

to measure the strains. In this regard, Figure 5.31 shows the measured and the numerical load-deflection curves. The proposed model can predict quite well the global response of the structure. The response for the unstrengthened case is also depicted.

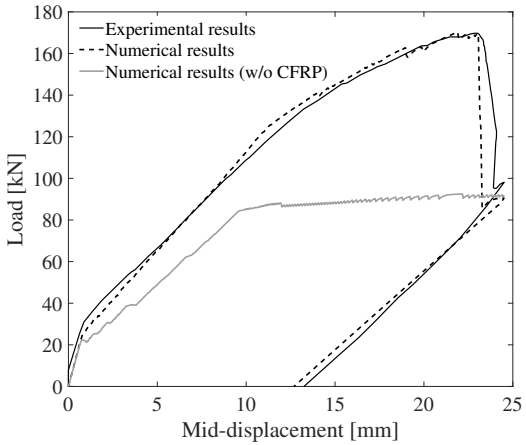

Figure 5.31.: Mid-displacement versus applied load curve (VVBS3).

A sudden debonding failure takes place in a range of approximately 200 ∼ 600 mm to the left of the centre of the beam at a load of 168.8 kN and a de-

flection of 23.0 mm. At this point, the maximum crack width reaches a value equal to 0.9 mm, while the elongation of the sheet takes a maximum of 6.2 mm/m. The debonding of the external reinforcement is followed by a drop in the load. The numerical model predicts likewise a debonding failure, which occurs in a range of approximately 200 ∼ 450 mm at a load of 169.4 kN and a deflection of 23.1 mm. Figure 5.36 shows the slip profile along the sheet at the time of failure (the straight black lines mark the the ultimate slip), where the debonding zone can be identified. The calculated maximum crack width and elongation are 0.8 mm and 7.1 mm/m, respectively, which match well with the observations. Furthermore, the model provides also good results regarding the descending branch as well as the unloading curve. Compared with the unstrengthened case, the presence of the sheet improves substantially the load-carrying capacity of the beam. Note that once full debonding occurs, the response curves overlap each other.

In Figure 5.32, the crack pattern obtained at the end of the test is compared with the numerical results. The distribution and orientation of the predicted cracks agree well with the experiments. The presence of the external reinforcement favours the formation of more cracks in comparison with the unstrengthened counterpart, see Figure 5.32 (c). It should also be mentioned that the cracks coalescence present on the measured crack pattern may be successfully reproduced by the junction enrichment exposed earlier in this work.

Figures 5.33 and 5.34 illustrate the deformed shapes and the axial strain distribution along the sheet for different load stages, respectively. A good agreement between both the numerical and the experimental results can be observed. The predicted strains are calculated in correspondence with the location of the 20 gauges.

The axial stress profiles of the lower reinforcing bar and the sheet are compared for different load stages in Figure 5.35. The straight black line indicates the elastic limit. The stresses increase gradually during loading and along the specimen by increasing deflection up to the point where the bar reaches the yield strength. It can be observed that beyond this point the increasing force across the section can only partially be taken by the bar and, therefore, the stress in the sheet increases considerably. Due to the lower cross area of the sheet compared to that of the bar (ratio of 2.87), the peaks observed at the cracks location are sharper in the sheet profile. Once debonding failure

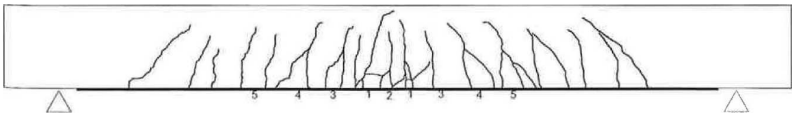

(a) Experimental crack pattern.

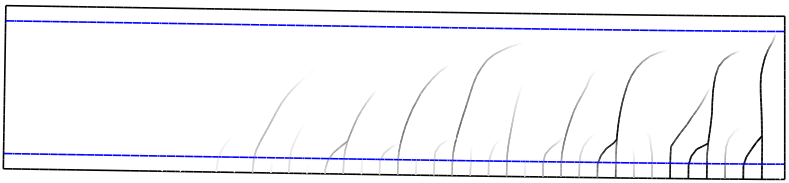

(b) Computed crack pattern (strengthened).

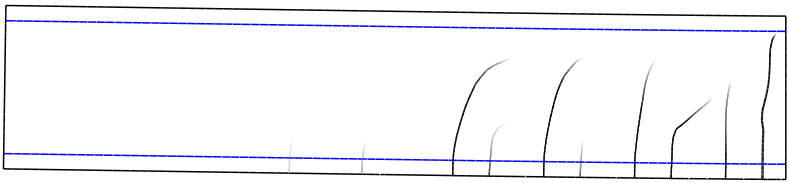

(c) Computed crack pattern (unstrengthened).

Figure 5.32.: Final crack pattern (VVBS3).

occurs, the stress in the bar is drastically reduced and reaches values similar to those of the unstrengthened beam profile. Note that the sheet stress remains constant along the section between the 1700 mm and 1950 mm, where debonding has already began (compare with Figure 5.36). Within this section the bond stress drops to zero and, consequently, no further force is transferred to the sheet from the adjacent concrete.

5.4.4. Fibre reinforced four-point bending beam

This simulation concerns one of the four point bending test performed by SORELLI et al. [112]. The specimen consists of a 100x320x40 mm^3 concrete beam with a span length of 300 mm and a distance between the load points of 100 mm as illustrated in Figure 5.37. The mechanical properties of the concrete and the fibres as well as the bond stress-slip relationship are the same used in the tensile test analysed earlier in this chapter, which were determined by means of a best fitting procedure. The strain ϵ_{c_3} takes the value

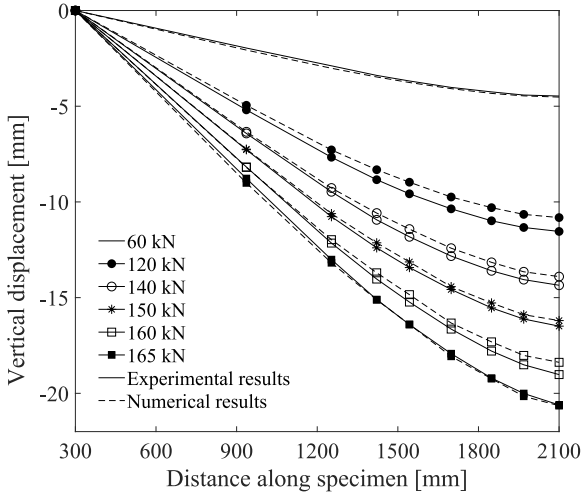

Figure 5.33.: Deformed shape at different load stages (VVBS3).

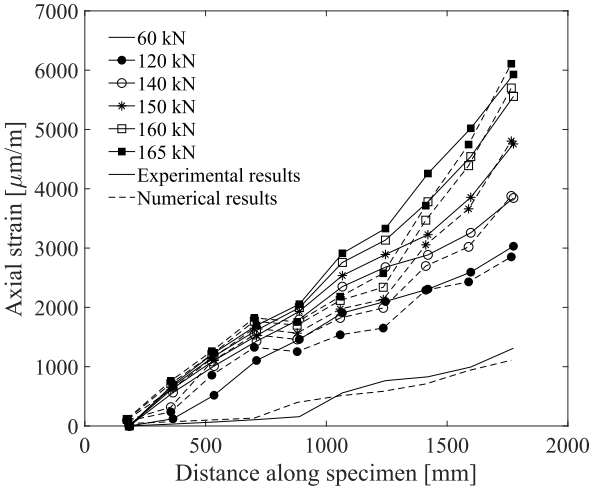

Figure 5.34.: Axial strain profile along the sheet at different load stages (VVBS3).

−2.3% according to the code. The model is built with 437 4-nodes quadrilateral elements. In this case, the fibre density measured in the cracked section

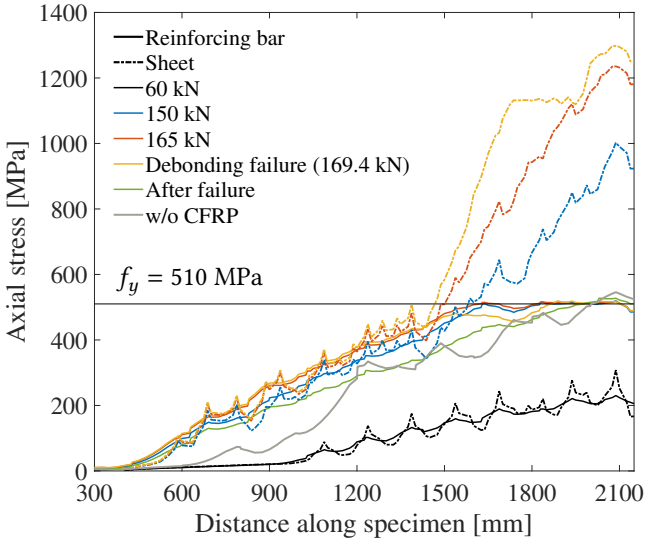

Figure 5.35.: Axial stress profile of the lower bar and the sheet at different load stages (VVBS3).

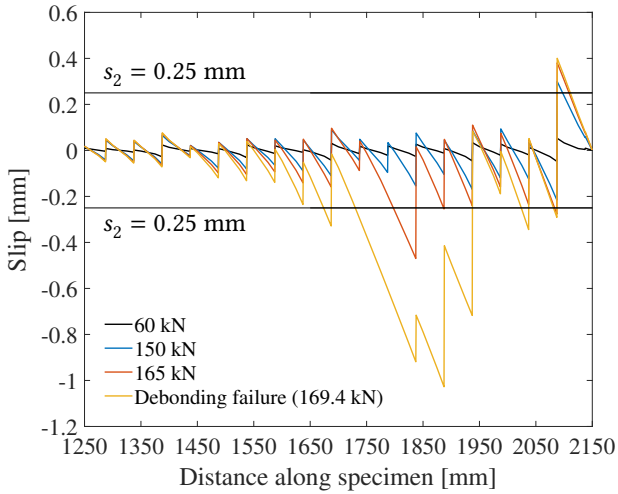

Figure 5.36.: Slip profile of the lower bar at different load stages (VVBS3).

amounts to 3.43 fibres/cm^2, corresponding to 116 fibres. As in the tensile test model, only half of the fibre are explicitly modelled.

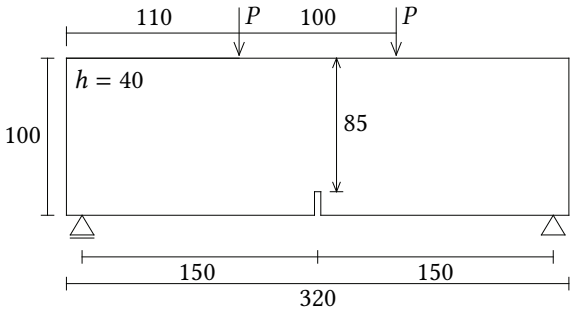

Figure 5.37.: Test setup of the fibre reinforced four point bending beam performed by SORELLI et al. [112]. All dimensions in millimetres.

The applied load as a function of the CTOD for both the strengthened and the unstrengthened beams are shown in Figure 5.38 and 5.39, respectively. The results measured in the tests are also depicted. The cohesive and bond laws determined from the tensile test provide a fairly good approximation between both the predicted and the experimental data.

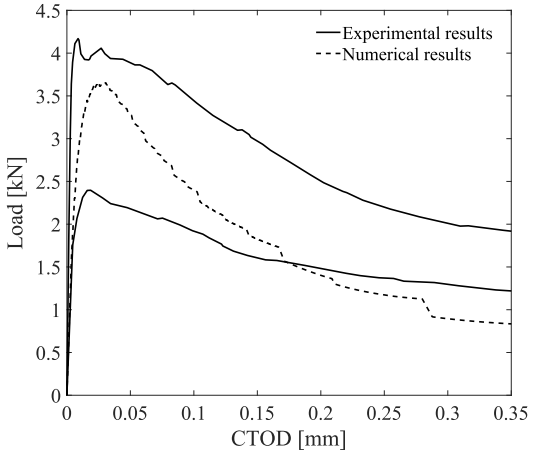

Figure 5.38.: Displacement versus applied load curve (strengthened 4PBT).

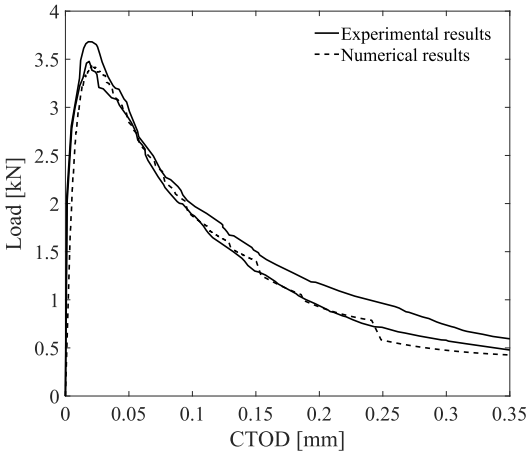

Figure 5.39.: Displacement versus applied load curve (unstrengthened 4PBT).

5.5. Walls

5.5.1. RC walls C1 and C2

This example deals with some of the tests conducted by LU et al. [79], which comprised six RC walls subjected to a pseudo-static cyclic loading. Only walls C1 and C2 are considered in this analysis. The wall specimens had all the same dimensions, but differ from one another in the loading conditions, specifically, in the shear span ratio (the ratio between the shear span height and the wall length). Figure 5.40 illustrates the test setup for the numerical simulation. Wall C1 presents a shear span ratio equal to 2, while wall C2, equal to 4. In order to achieve a shear span ratio of 4, an additional moment, calculated on the basis of the output of the lateral load, is applied to the wall. Both walls are subjected to a constant axial load of 290 kN, which is modelled as a distributed load q along the top of the wall as shown the figure. The magnitude of the distributed load q is then equal to 207.1 N/mm. A rigid body is used to model the steel loading beam. For the wall C1, having a span ratio of 2, the height of the loading beam is the same as that used in the test, i.e. $h = 170$ mm. For the wall C2, the additional moment is introduced by increasing the height of the beam in 2400 mm, i.e. $h = 170 + 2400 = 2570$

mm. The cyclic lateral loading sequence used in the test consists of a drift-controlled mode at the following drift increments: 0.2, 0.25, 0.35, 0.5, 0.75, 1.0, 1.5, 2.0, and 2.5%.

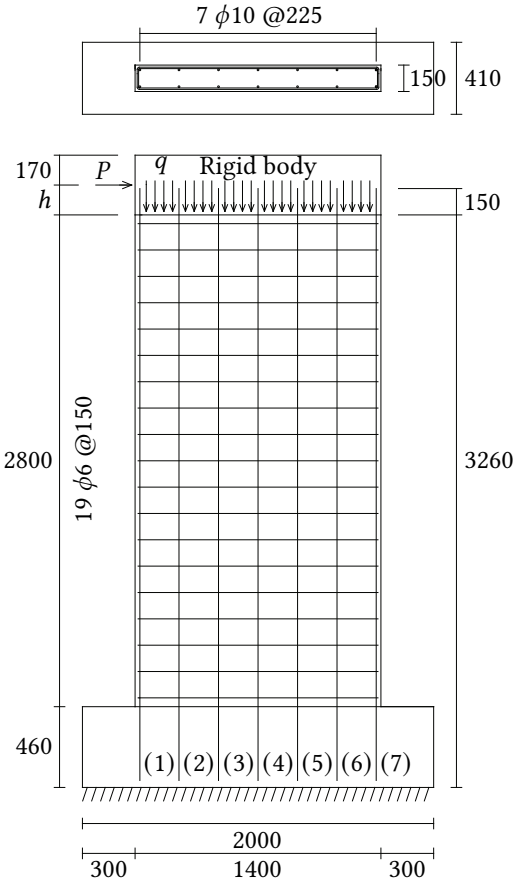

Figure 5.40.: Test setup of the RC walls C1 and C2 tested by LU et al. [79]. All dimensions in millimetres.

The mechanical properties of the concrete and the reinforcement according to the measured values are listed in Table 5.20 and 5.21 .

The model is built with 1580 4-nodes quadrilateral elements. The parameters that define the bond stress-slip relationship are summarised in Table 5.22. In

Table 5.20.: Mechanical properties of the concrete (walls C1 and C2).

Test wall	E [GPa]	ν	f_c [MPa]	f_t [MPa]	G_f [N/mm]	ϵ_{c_3} [%]
C1	26.0	0.18	38.5	2.88	0.077*	−2.4*
C2	27.5	0.18	34.5	2.53	0.071*	−2.3*

Table 5.21.: Mechanical properties of the reinforcement (walls C1 and C2).

	E [GPa]	ν	f_y [MPa]	f_u [MPa]	H [MPa]
$\phi 6$	200	0.30	300.6	461.8	0
$\phi 10$	200	0.30	300.0	409.0	0

the tests, the vertical reinforcement was extended out of the top of the walls and secured to the steel loading beam. Therefore, perfect bond is assumed in the model for those parts of the reinforcing bars within the loading beam.

Table 5.22.: Parameters of the bond stress-slip relationship (walls C1 and C2).

Test wall		s_1 [mm]	s_2 [mm]	s_3 [mm]	τ_{max} [MPa]	τ_f [MPa]
C1	$\phi 10$	0.89	0.89	2	14.79	5.91
	$\phi 6$	1	2	2.4	15.51	6.20
C2	$\phi 10$	0.95	0.95	2	14.38	5.75
	$\phi 6$	1	2	2.4	14.68	5.87

Figures 5.41 and 5.42 compare the computed base moment-displacement curves with the experimental data for the walls C1 and C2, respectively. The model can reproduce fairly well the measured response up to a lateral drift of ±1.5% prior to the degradation caused, mainly, by the buckling of the vertical reinforcement and, to a lesser extent, by the inherently wear due to the continuous load/unload cycles. These discrepancies presented in the last drift cycles (±2.0% and ±2.5%) are attributed to the limitations of the material models used in the simulations. As stated in Sections 3.2.1 and 3.5.2, the material models employed do not consider the stiffness degradation under cyclic loading. Furthermore, the constitutive model defined for the reinforcing steel under compression does not take into account the effect of buckling and its subsequent influence on the structure. Despite this, the cyclic response is captured with reasonable accuracy. The unloading stiffness and the residual drift due to plastic deformation of the bars are properly represented. It

should be noted that the predicted results are in agreement with the numerical results reported in [78].

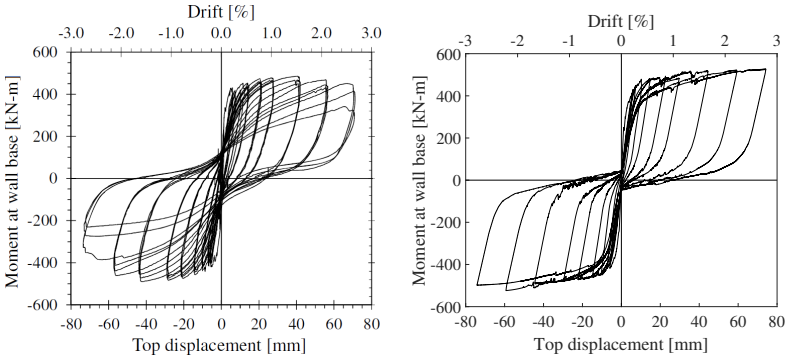

(a) Test. **(b)** Model.

Figure 5.41.: Moment-displacement responses (wall C1).

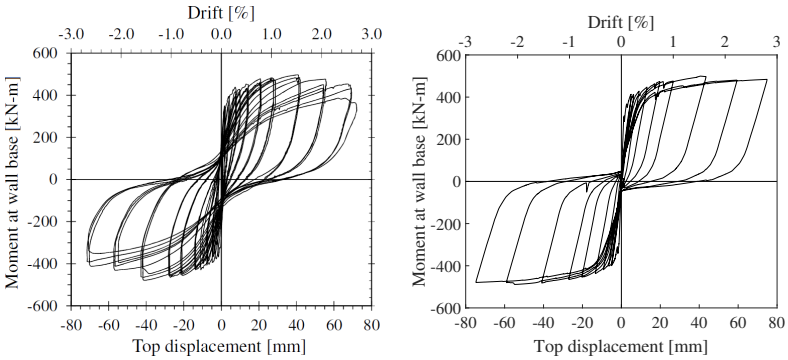

(a) Test. **(b)** Model.

Figure 5.42.: Moment-displacement responses (wall C2).

The measured and predicated reinforcement strains of the corner vertical reinforcements (west and east sides) at ±1.5% of the lateral drift are shown in Figure 5.43. The average strains were measured using 10 displacement gauges welded onto the vertical reinforcement over a 150 mm gauge length. Therefore, the computed strains are obtained at the same locations in a similar fashion. The measurement were significantly affected by the crack dis-

tribution and the gauge length, which may have affected the results. In spite of this, the numerical results can be considered to be in a good agreement with the measured results. The same tendency is to be observed along the bars, the strains remain low in the upper section and large strains occur at the wall base at the location of the main cracks.

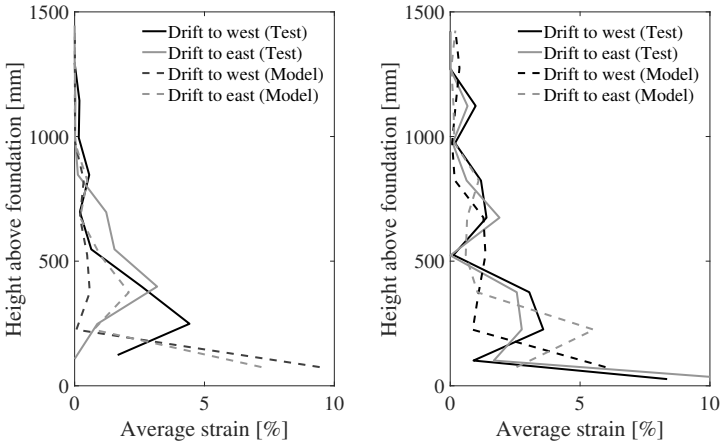

(a) Wall C1. **(b)** Wall C2.

Figure 5.43.: Reinforcement strain profiles at ±1.5% of the lateral drift (walls C1 and C2).

The final crack patterns documented during the tests are compared with the predicted crack patterns in Figures 5.44 and 5.45. A good agreement can be observed. The walls response was dominated by three or four main flexural cracks forming in the lower third of the walls on both sides, with the bottom crack opening the widest ($>$ 20 mm) as the lateral drift cycles increased. Moreover, due to the higher shear span ratio, the crack pattern of wall C2 extends up to the upper third. This behaviour is accurately captured by the model. The coalescence of cracks can be also nicely replicated.

The compressive failure pattern in the wall C2, characterised by the damage variable D, is depicted in Figure 5.46. The dark color corresponds to a high damage level, close to 1. The damage profile can be reasonably captured by the numerical model, at least with regard to the location of the damage. The damage variable reaches a maximum of 0.93 at the bottom right corner of the wall, which is equivalent to reduce the the elastic modulus by 93%. The

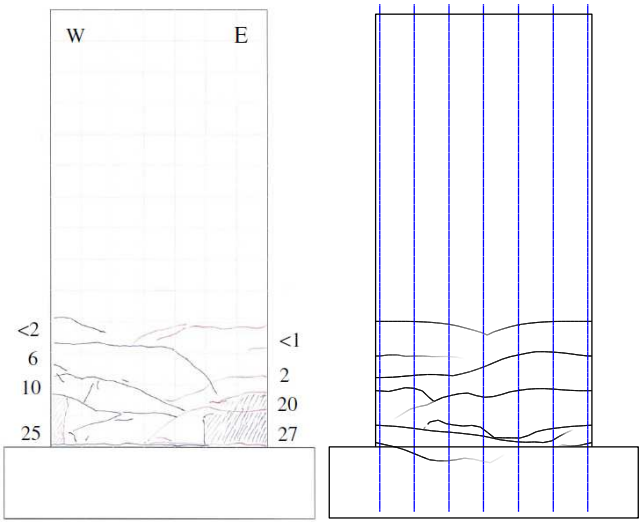

(a) Experimental crack pattern. **(b)** Computed crack pattern.

Figure 5.44.: Final crack pattern (wall C1).

degree of deterioration reached by the test is higher, to the point of detachment of the concrete cover as shown in Figure 5.44 (a) (hatched zone). This discrepancy is due to the choice of the stress-strain relationship presented in Section 3.3, which does not consider the softening behaviour experienced by the concrete once the compressive strength is exceeded.

5.6. Sensitivity analysis

A sensitivity analysis is performed in order to determinate how sensitive is the structure response and, particularly, the crack path to the element type, mesh size and density of candidate points with respect to the proposed finite element formulation. The four-point bending beam tested by JASON et al. and studied in Section 5.4.2 is used for the analysis.

Two different element types are considered in the analysis, namely, a three-node triangular element and a four-node quadrilateral element. For each

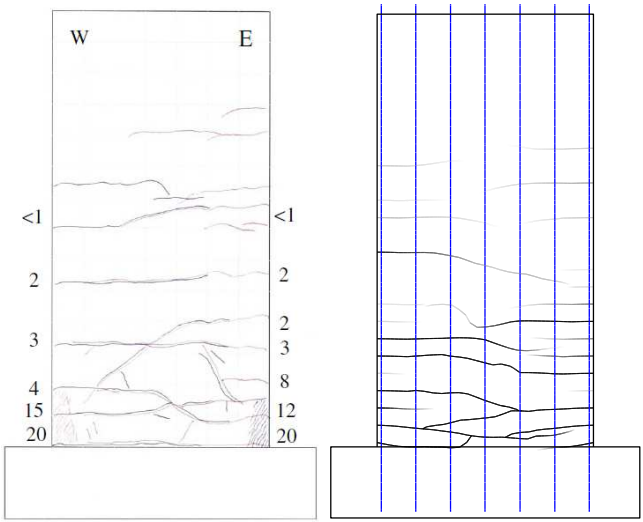

(a) Experimental crack pattern. **(b)** Computed crack pattern.

Figure 5.45.: Final crack pattern (wall C2).

type, a coarse and a fine mesh are generated. The fine mesh has two times as many elements as the course one. The triangular meshes are built so that they have approximately the same number of nodes than the quadrilateral ones. Thus, four different discretisations are analysed. The candidate points considered are depicted in Figures A.4-A.7. In addition, two more points distributions are studied in the quadrilateral fine mesh as shown in Figure A.5, corresponding to half and third of the original points.

The beam response is not significantly affected by the variables analysed as illustrates Figure 5.47. The curves agree fairly well with each other and with the experimental results. Slight differences are observed towards the end of the simulation, where the coarse meshes exhibit a stiffer behaviour.

The crack patterns at a load of 36 kN are illustrated in Figure 5.48. As can be observed, the cracks distribution is influenced by the discretisation and by the candidate points configuration. However, this does not affect the quality of results when compared with the experimental data. In general, all predicted crack patters are in good agreement with the measured crack pattern

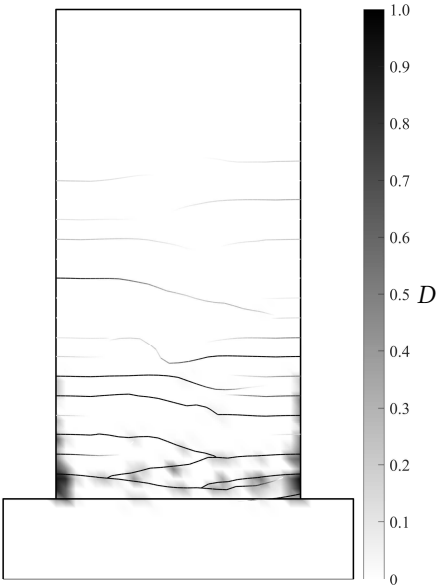

Figure 5.46.: Compressive failure pattern (wall C2).

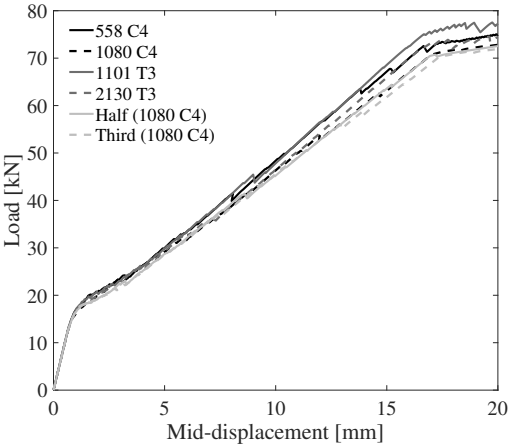

Figure 5.47.: Load-displacement response (sensitivity analysis).

(see Figure 5.28). All meshes provide a good performance, indicating that the computed response may be considered insensitive to the spatial discretisation.

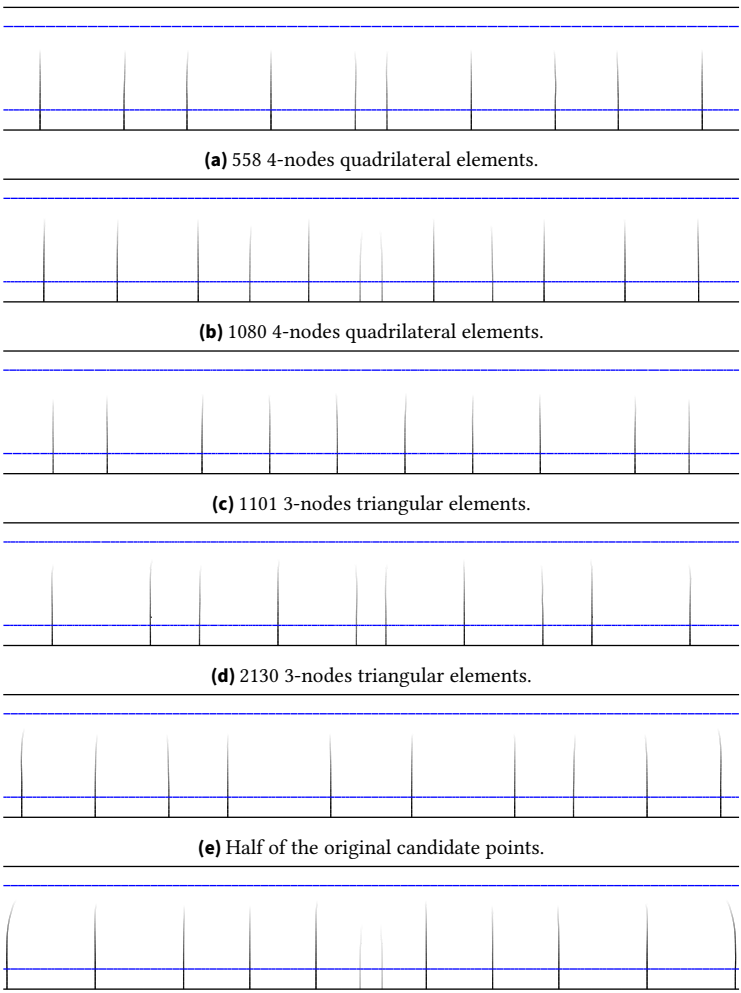

(a) 558 4-nodes quadrilateral elements.

(b) 1080 4-nodes quadrilateral elements.

(c) 1101 3-nodes triangular elements.

(d) 2130 3-nodes triangular elements.

(e) Half of the original candidate points.

(f) Third of the original candidate points.

Figure 5.48.: Crack pattern (sensitivity analysis).

6. Summary, conclusions and future work

6.1. Summary and conclusions

A two-dimensional extended finite element model was developed for the simulation of multiple crack growth in reinforced concrete structures under static loading conditions. X-FEM is particularly suitable for this task, since the mesh does not need to conform to the discontinuities geometry and, consequently, remeshing is completely avoided, leading to lower computational costs. The application of X-FEM for the modelling of multiple cracks, reinforcing steel, bonded reinforcement and fibres within the same framework, represents the great novelty of this work. The behaviour of the constituent materials, i.e. cracked concrete, reinforcement and interface between them, are explicitly represented.

A non-singular near-tip function is employed to represent the crack tip within an element, while a discontinuous step function is used to account for the displacement jump across the crack surfaces in fully cracked elements. In this way, the crack is allowed to propagate to any location inside an element without the need of redefining the underlying finite element mesh. The growth of multiple cracks requires the modelling of the possible interaction between them. In this regard, only crack coalescence is considered. This interaction is treated using a junction enrichment. Then, considering these enrichment functions, the cracks growth simulation can be run from early cracking towards complete failure in a mesh independent way. In this work, cracks are represented explicitly by the union of straight-line segments. These segments are fixed once they are initiated in an element.

A cohesive crack model is applied within the proposed finite element approach to represent the cohesive cracks and to describe the crack initiation process and the further propagation through the structure. Cracks propagate

by adding new straight-line segments. Stress-based criteria are considered to predict tensile failure. The maximum stress criterion (RANKINE criterion) is used to evaluate whether a crack initiates its propagation at a predefined point, denoted as candidate point, or not; while the stress condition is used as criterion for existing cracks. In this latter case, a non-local formulation is employed to evaluate the stress at the crack tip. In both cases, the propagation angle is determined according to the maximum principal stress criterion. Cracks are assumed to propagate until the equilibrium state of the current loading step is reached.

Reinforcing bars, including transverse reinforcement, as well as bonded reinforcement and fibres are described individually by means of a HEAVISIDE function. This function is considered to be discontinuous at the reinforcement domain and constant otherwise. This characteristic allows the reinforcement to be arbitrarily orientated and positioned within an element without meshing it. The cracked concrete bulk is then treated as a background on which discrete reinforcement is superimposed, being the transfer of bond forces their only interaction mechanisms. A bond model is used in each interface to mediate this interaction. A constitutive relation considering both bond-slip behaviour and dowel action are assumed for the reinforcing bars (transverse bars included), while only bond-slip is considered for bonded reinforcement and fibres.

An isotropic damage model is used to describe the behaviour of concrete in compression. The damage variable is computed using the secant stiffness. The equivalent strain, characterising the damage evolution, is taken to be equal to the minimum principal strain. In order to overcome the convergence difficulties presented in the simulations because of the softening behaviour exhibits by the concrete, a parabola-line curve without softening is assumed for the stress-strain relationship.

A general framework has been developed to describe the approximate fields, i.e. the displacement field, the relative displacement fields and the strain field, which considers the presence of multiple cracks (each characterised by a near-tip enrichment and a discontinuous step enrichment), multiple coalescence of cracks (each characterised by a junction enrichment) and multiple layer of reinforcement (each characterised by a HEAVISIDE enrichment). The discretisation is performed at an element scale in a matrix representation using the VOIGT notation. The weak formulation is flexibly formulated, allowing for any constitutive relations for the material models.

The proposed finite element model was applied to simulate representative tests reported in the literature on reinforced concrete structures. These tests cover a wide range of geometries and sizes as well as of reinforcement arrangements. In all tests, the numerical results are in very good agreement with the available data and, therefore, confirm the accuracy of the proposed approach. The model is able to describe strengthened structures, reproducing reasonably well their behaviour. This shows the versatility of the HEAVISIDE enrichment when modelling any type of reinforcement. The model predicts final crack patterns containing multiple cracks that resemble experimental results. Moreover, detailed information regarding the mechanical properties of each constituent part, such as stresses and strains, cohesive forces and cracks width, slips and bond stresses, among others, can be accurately obtained at every stage of the simulation. It was demonstrated that the model can also be performed with coarse meshes, showing that the predicted responses are mesh independent. The material models and, particularly, the constitute relations used prove to be quite effective when reproducing the material behaviour and, to a larger extent, the global response. Furthermore, the fracture criteria are able to predict crack patterns accurately when compared with experimental data.

Due to its versatility, simplicity and great accuracy, the extended finite element method may become the main numerical tool for the study of fracture in reinforced concrete structures and even of a wide range of engineering applications.

6.2. Future work

The finite element model needs to be validated further by evaluating its performance in the simulation of more complex structures such as frame corners, corbels, etc., in which the arrangement of the reinforcement and the failure mechanisms are more complicated. To this extent, it may be necessary to incorporate models that are able to reproduce splitting tensile failure.

Furthermore, more sensitivity analyses (length of the new straight-line segments, size of the influence radius, among others) are required to further verify the robustness of the proposed model and to establish a range of optimal operating parameters.

A straightforward extension to the work is to more complex cohesive models that include proper constitutive laws for mixed-mode fracture, and to cyclic material models that account for the damage accumulation due to cyclic loading. Moreover, the implementation of a proper material model for the modelling of concrete in compression is desirable. Concerning the damage model stated in this work, the use of a viscoplastic regularisation of the constitutive relations or a non-local approach could overcome the convergence difficulties.

An important area for further research is the modelling of dynamic fracture. In this regard, the proposed model can be extended by using the dynamic fracture criteria and time integration schemes presented in [16, 50, 131].

The finite element model developed in this thesis is limited to two-dimensional problems. Hence, an extension to three-dimensional models is a natural step. Regarding the modelling of the reinforcement, the use of the HEAVISIDE enrichment is straightforward. Since the reinforcement is assumed to be thin compared with its length and with the size of the matrix domain, it can be treated also as a 1D object in 3D models.

A. Appendix

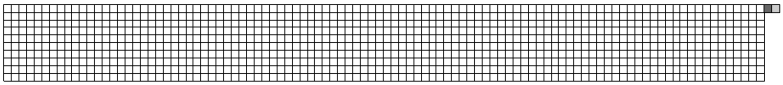

Figure A.1.: Finite element mesh of the single shear pull-out test (1002 4-nodes quadrilateral elements).

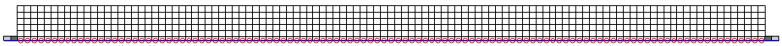

Figure A.2.: Finite element mesh of the RC tensile member STN12 (670 4-nodes quadrilateral elements).

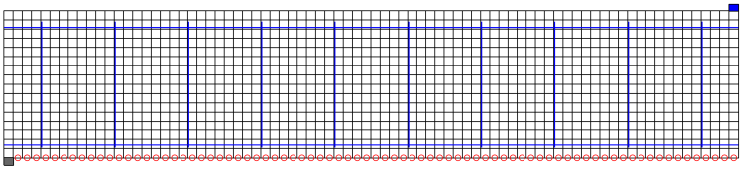

Figure A.3.: Finite element mesh of the of the RC beams T5A1 and T6A1 (1282 4-nodes quadrilateral elements).

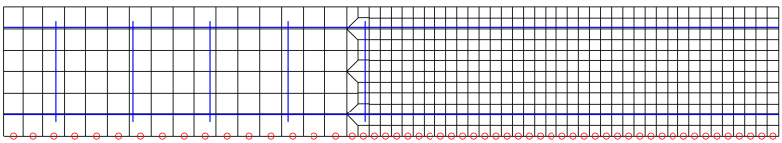

Figure A.4.: Finite element mesh of the RC four-point bending beam (558 4-nodes quadrilateral elements).

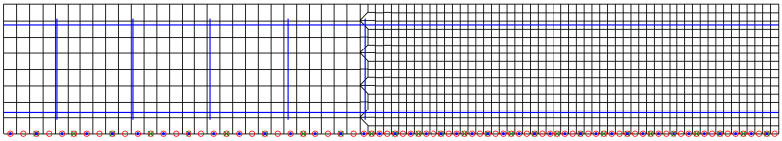

Figure A.5.: Finite element mesh of the RC four-point bending beam (1080 4-nodes quadrilateral elements).

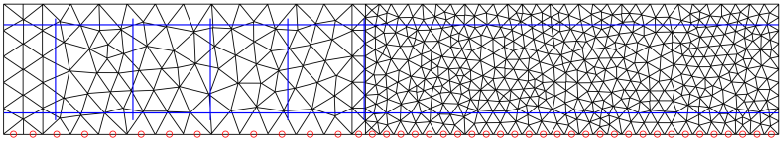

Figure A.6.: Finite element mesh of the RC four-point bending beam (1101 3-nodes triangular elements).

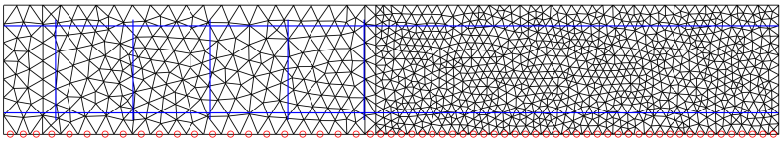

Figure A.7.: Finite element mesh of the RC four-point bending beam (2130 3-nodes triangular elements).

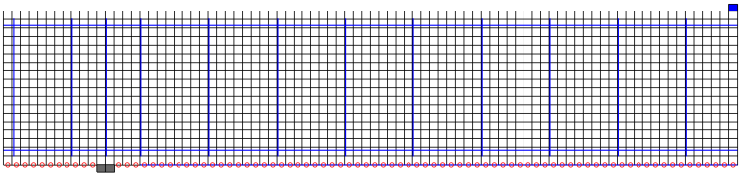

Figure A.8.: Finite element mesh of the RC beam VVBS3 (1551 4-nodes quadrilateral elements).

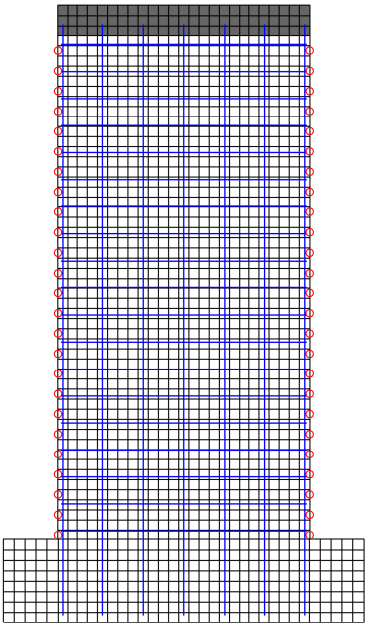

Figure A.9.: Finite element mesh of the RC walls C1 and C2 (1580 4-nodes quadrilateral elements).

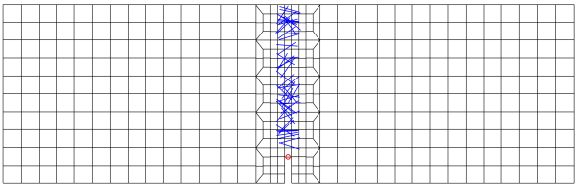

Figure A.10.: Finite element mesh of the fibre reinforced four point bending beam (437 4-nodes quadrilateral elements).

Bibliography

[1] ACI 544.4R-18. *Guide to Design with Fiber-Reinforced Concrete*. American Concrete Institute (ACI), 2018.

[2] Akkermann, J. *Rotationsverhalten von Stahlbeton-Rahmenecken*. PhD thesis, Universität Karlsruhe, 2000.

[3] Amidror, I. Scattered data interpolation methods for electronic imaging systems: a survey. *Journal of Electronic Imaging*, 11:157–176, 2002.

[4] Asferg, J. L., Poulsen, P. N., and Nielsen, L. O. A consistent partly cracked XFEM element for cohesive crack growth. *International Journal for Numerical Methods in Engineering*, 72:464–485, 2007.

[5] Auer, M. *Ein Verbundmodell für Stahlbeton unter Berücksichtigung der Betonschädigung*. PhD thesis, Karlsruher Institut für Technologie, 2007.

[6] Banholzer, B. and Brameshuber, W. Eine Methode zur Beschreibung des Verbundes zwischen Faser und zementgebundener Matrix. *Beton- und Stahlbetonbau*, 96:663–669, 2001.

[7] Barber, C. B., Dobkin, D. P., Dobkin, D. P., and Huhdanpaa, H. The Quickhull Algorithm for Convex Hulls. *ACM Trans. Math. Softw.*, 22:469–483, 1996.

[8] Barenblatt, G. I. The Mathematical Theory of Equilibrium Cracks in Brittle Fracture. *Advances in Applied Mechanics*, 7:55–129, 1962.

[9] Bažant, Z. P. and Oh, B. H. Crack band theory for fracture of concrete. *Matériaux et Construction*, 16:155–177, 1983.

[10] Bažant, Z. P. Instability ductility and size effect in strain - softening concrete. *Journal of Engineering Mechanics - ASCE*, 102:331–344, 1976.

[11] Bažant, Z. P. Concrete fracture models: Testing and practice. *Engineering Fracture Mechanics*, 69:165–205, 2002.

[12] Beaurepaire, P. and Schuëller, G. Modeling of the variability of fatigue crack growth using cohesive zone elements. *Engineering Fracture Mechanics*, 78:2399–2413, 2011.

[13] Béchet, E., Minnebo, H., Moës, N., and Burgardt, B. Improved implementation and robustness study of the X-FEM for stress analysis around cracks. *International Journal for Numerical Methods in Engineering*, 64:1033–1056, 2005.

[14] Belytschko, T. and Black, T. Elastic crack growth in finite elements with minimal remeshing. *International Journal for Numerical Methods in Engineering*, 45:601–620, 1999.

[15] Belytschko, T., Lu, Y. Y., and Gu, L. Element-free galerkin methods. *International Journal for Numerical Methods in Engineering*, 37:229–256, 1994.

[16] Belytschko, T., Chen, H., Xu, J., and Zi, G. Dynamic crack propagation based on loss of hyperbolicity and a new discontinuous enrichment. *International Journal for Numerical Methods in Engineering*, 58:1873–1905, 2003.

[17] Belytschko, T., Gracie, R., and Ventura, G. A review of extended/generalized finite element methods for material modeling. *Modelling and Simulation in Materials Science and Engineering*, 17:1–24, 2009.

[18] Bentur, A., Mindess, S., and Routledge. *Fibre Reinforced Cementitious Composites*. Modern Concrete Technology. CRC Press, 2006.

[19] Benvenuti, E. A regularized XFEM framework for embedded cohesive interfaces. *Computer Methods in Applied Mechanics and Engineering*, 197:4367–4378, 2008.

[20] Benvenuti, E., Orlando, N., Ferretti, D., and Tralli, A. A new 3D experimentally consistent XFEM to simulate delamination in FRP-reinforced concrete. *Composites Part B: Engineering*, 91:346–360, 2016.

[21] Benvenuti, E. and Tralli, A. Simulation of finite-width process zone in concrete-like materials by means of a regularized extended finite element model. *Computational Mechanics*, 50:479–497, 2012.

[22] Bosco, C., Debernardi, P., and di Torino. Dipartimento di Ingegneria Strutturale, P. *Experimental investigation on the ultimate rotational capacity of R.C. beams*. Atti del Dipartimento. Levrotto & Bella, 1992.

[23] Brenna, A., Dei Poli, S., and Di Prisco, M. Dowel Action: Some Experimental and Theoretical Results Regarding Special Concretes. *Studi e Ricerche, School for the design of R/C structures, Milan University of Technology*:321–380, 1990.

[24] Budyn, É., Zi, G., Moës, N., and Belytschko, T. A method for multiple crack growth in brittle materials without remeshing. *International Journal for Numerical Methods in Engineering*, 61:1741–1770, 2004.

[25] C. Becker S. Jox, G. M. 3D Higher-OrderX-FEM Model for the Simulation of Cohesive Cracks in Cementitious Materials Considering Hygro-Mechanical Couplings. *Computer Modeling in Engineering & Sciences*, 57:245–278, 2010.

[26] Camanho, P. P. and Dávila, C. G. Mixed-Mode Decohesion Finite Elements for the Simulation of Delamination in Composite Materials, 2002.

[27] Chahine, E., Laborde, P., and Renard, Y. A quasi-optimal convergence result for fracture mechanics with XFEM. *Comptes rendus de l'Académie des sciences. Série I, Mathématique*, 342:527–532, 2006.

[28] Chen, H. *Enriched finite element methods and its applications*. PhD thesis, Northwestern University, 2003.

[29] Chen, J. F. and Teng, J. G. Anchorage strength models for FRP and Steel Plates Bonded to Concrete. *Journal of Structural Engineering*, 127:784–791, 2001.

[30] Chen, X., Deng, X., Sutton, M. A., and Zavattieri, P. An inverse analysis of cohesive zone model parameter values for ductile crack growth simulations. *International Journal of Mechanical Sciences*, 79:206–215, 2014.

[31] Daux, C., Moës, N., Dolbow, J., Sukumar, N., and Belytschko, T. Arbitrary branched and intersecting cracks with the extended finite element method. *International Journal for Numerical Methods in Engineering*, 48:1741–1760, 2000.

[32] De Borst, R., Remmers, J. J. C., Needleman, A., and Abellan, M.-A. Discrete vs smeared crack models for concrete fracture: bridging the gap. *International Journal for Numerical and Analytical Methods in Geomechanics*, 28:583–607, 2004.

[33] De Lorenzis, L., Fernando, D., and Teng, J.-G. Coupled mixed-mode cohesive zone modeling of interfacial debonding in simply supported plated beams. *International Journal of Solids and Structures*, 50:2477–2494, 2013.

[34] De Morais, A. B. Mode I cohesive zone model for delamination in composite beams. *Engineering Fracture Mechanics*, 109:236–245, 2013.

[35] De Souza Neto, E. A., Perić, D., and Owen, D. R. J. *Computational Methods for Plasticity: Theory and Applications*. John Wiley & Sons, Ltd, 2008.

[36] Dolbow, J. *An Extended Finite Element Method with Discontinuous Enrichment for Applied Mechanics*. PhD thesis, Northwestern University, 1999.

[37] Dolbow, J., Moës, N., and Belytschko, T. An extended finite element method for modeling crack growth with frictional contact. *Computer Methods in Applied Mechanics and Engineering*, 190:6825–6846, 2001.

[38] Dolbow, J., Moës, N., and Belytschko, T. Discontinuous enrichment in finite elements with a partition of unity method. *Finite Elements in Analysis and Design*, 36:235–260, 2000.

[39] Dolbow, J., Moës, N., and Belytschko, T. Modeling fracture in mindlin-reissner plates with the extended finite element method. *International Journal of Solids and Structures*, 37:7161–7183, 2000.

[40] Dugdale, D. S. Yielding of steel sheets containing slits. *Journal of the Mechanics and Physics of Solids*, 8:100–104, 1960.

[41] Dumstorff, P. *Modellierung und numerische Simulation von Rissfortschritt in spröden und quasi-spröden Materialien auf Basis der Extended Finite Element Method*. PhD thesis, Ruhr-Universität Bochum, 2006.

[42] Eligehausen, R., P. Popov, E., and V. Bertero, V. *Local bond stress-slip relationships of deformed bars under generalized excitations*. Report Nr. UCB/EERC 83-23, Earthquake Engineering Research Center. Earthquake Engineering Research Center, College of Engineering, University of California, 1983.

[43] Ferté, G., Massin, P., and Moës, N. 3D crack propagation with cohesive elements in the extended finite element method. *Computer Methods in Applied Mechanics and Engineering*, 300:347–374, 2016.

[44] Fib Bulletin 10. *Bond of Reinforcement in Concrete: State-of-the-art report*. fib - Fédération internationale du béton, Lausanne, Switzerland, 2000.

[45] Fib Bulletin 213. *Model Code 1990: Final Draft*, volume 1. fib - Fédération internationale du béton, Lausanne, Switzerland, 1990.

[46] Fib Bulletin 40. *FRP reinforcement in RC structures*. fib - Fédération internationale du béton, Lausanne, Switzerland, 2007.

[47] Fib Bulletin 55. *Model Code 2010: Final Draft*, volume 1. fib - Fédération internationale du béton, Lausanne, Switzerland, 2012.

[48] Fib Bulletin 79. *Fibre-reinforced concrete: From design to structural applications - FRC 2014: ACI-fib International Workshop*. fib - Fédération internationale du béton, 2016.

[49] Fleming, M., Chu, Y. A., Moran, B., and Belytschko, T. Enriched element-free galerkin methods for crack tip fields. *International Journal for Numerical Methods in Engineering*, 40:1483–1504, 1997.

[50] Fleming, W. *Quasi Static and Dynamic Crack Propagation in Brittle Materials with XFEM*. PhD thesis, Universität Kassel, 2011.

[51] Fries, T.-P. A corrected XFEM approximation without problems in blending elements. *International Journal for Numerical Methods in Engineering*, 75:503–532, 2008.

[52] Géniaut, S., Massin, P., and Moës, N. A stable 3D contact formulation using X-fem. *European Journal of Computational Mechanics/Revue Européenne de Mécanique Numérique*, 16:259–275, 2007.

[53] Gravouil, A., Moës, N., and Belytschko, T. Non-planar 3D crack growth by the extended finite element and level sets—Part II: Level set update. *International Journal for Numerical Methods in Engineering*, 53:2569–2586, 2002.

[54] Gutiérrez, R., Stempniewski, L., and Fleming, W. Modelling steel-concrete interaction using the extended finite element method. *Obras y proyectos*, 24:6–12, 2018.

[55] Hettich, T. and Ramm, E. Interface material failure modeled by the extended finite-element method and level sets. *Computer Methods in Applied Mechanics and Engineering*, 195:4753–4767, 2006.

[56] Hettich, T. M. *Diskontinuierliche Modellierung zur Versagensanalyse von Verbundmaterialien*. PhD thesis, Universität Stuttgart, 2007.

[57] Hillerborg, A., Modéer, M., and Petersson, P.-E. Analysis of crack formation and crack growth in concrete by means of fracture mechanics and finite elements. *Cement and Concrete Research*, 6:773–781, 1976.

[58] Hofstetter, G. and Mang, H. *Computational Mechanics of Reinforced Concrete Structures*. Grundlagen und Fortschritte der Ingenieurwissenschaften. Vieweg+Teubner Verlag, 1995.

[59] Ibrahimbegovic, A., Boulkertous, A., Davenne, L., and Brancherie, D. Modelling of reinforced-concrete structures providing crack-spacing based on X-FEM, ED-FEM and novel operator split solution procedure. *International Journal for Numerical Methods in Engineering*, 83:452–481, 2010.

[60] Ingraffea, A. R. and Saouma, V. *Numerical modeling of discrete crack propagation in reinforced and plain concrete*. In *Fracture mechanics of concrete: Structural application and numerical calculation*. Springer Netherlands, Dordrecht, 1985, pages 171–225.

[61] Jaékowiec, J. and van der Meer, F. P. A consistent iterative scheme for 2D and 3D cohesive crack analysis in XFEM. *Computers & Structures*, 136:98–107, 2014.

[62] Jason, L., Torre-Casanova, A., Davenne, L., and Pinelli, X. Cracking behavior of reinforced concrete beams: experiment and simulations on the numerical influence of the steel-concrete bond. *International Journal of Fracture*, 180:243–260, 2013.

[63] Jiang, L., Nath, C., Samuel, J., and Kapoor, S. Estimating the Cohesive Zone Model Parameters of Carbon Nanotube–Polymer Interface for Machining Simulations. *Journal of Manufacturing Science and Engineering*, 136:031004, 2014.

[64] Jin, Z.-H and Sun, C. Cohesive zone modeling of interface fracture in elastic bi-materials. *Engineering Fracture Mechanics*, 72:1805–1817, 2005.

[65] Karihaloo, B. *Fracture Mechanics and Structural Concrete*. Concrete design and construction series. Longman Scientific & Technical, 1995.

[66] Kobarg, J. Verankerung axialbeanspruchter Bewehrungsstäbe im Beton unter Querbeanspruchung. Technical report, Karlsruher Institut für Technologie, 1984.

[67] Laborde, P., Pommier, J., Renard, Y., and Salaün, M. High-order extended finite element method for cracked domains. *International Journal for Numerical Methods in Engineering*, 64:354–381, 2005.

[68] Ladevéze, P. *Nonlinear Computational Structural Mechanics*. Springer: New York, 1998.

[69] Leonhardt, F. On the Need to Consider the Influence of Lateral Stresses on Bond. In *RILEM Symposium on Bond and Crack Formation in Reinforced Concrete*. Volume 1, pages 29–34. Stockholm, 1957.

[70] Lettow, S. *Ein Verbundelement für nichtlineare Finite Elemente Analysen - Anwendung auf Übergreifungsstöße*. PhD thesis, Universität Stuttgart, 2006.

[71] Li, H. and Chandra, N. Analysis of crack growth and crack-tip plasticity in ductile materials using cohesive zone models. *International Journal of Plasticity*, 19:849–882, 2003.

[72] Li, H., Yuan, H., and Li, X. Assessment of low cycle fatigue crack growth under mixed-mode loading conditions by using a cohesive zone model. *International Journal of Fatigue*, 75:39–50, 2015.

[73] Liao, F. and Huang, Z. An extended finite element model for modelling localised fracture of reinforced concrete beams in fire. *Computers & Structures*, 152:11–26, 2015.

[74] Liu, F. and Borja, R. I. A contact algorithm for frictional crack propagation with the extended finite element method. *International Journal for Numerical Methods in Engineering*, 76:1489–1512, 2008.

[75] Löhnert, S. A stabilization technique for the regularization of nearly singular extended finite elements. *Computational Mechanics*, 54:523–533, 2014.

[76] Löhnert, S., Müller-Hoeppe, D. S., and Wriggers, P. 3d corrected XFEM approach and extension to finite deformation theory. *International Journal for Numerical Methods in Engineering*, 86:431–452, 2011.

[77] Löhnert, S. Stabilizing the XFEM for static and dynamic crack simulations. *Proceedings in Applied Mathematics and Mechanics*, 15:137–138, 2015.

[78] Lu, Y. and Henry, R. S. Numerical modelling of reinforced concrete walls with minimum vertical reinforcement. *Engineering Structures*, 143:330–345, 2017.

[79] Lu, Y., Henry, R. S., Gultom, R., and Ma, Q. T. Cyclic Testing of Reinforced Concrete Walls with Distributed Minimum Vertical Reinforcement. *Journal of Structural Engineering*, 143:04016225, 2017.

[80] Mariani, S. and Perego, U. Extended finite element method for quasi-brittle fracture. *International Journal for Numerical Methods in Engineering*, 58:103–126, 2003.

[81] Melenk, J. M. and Babuška, I. The partition of unity finite element method: Basic theory and applications. *Computer Methods in Applied Mechanics and Engineering*, 139:289–314, 1996.

[82] Mergheim, J., Kuhl, E., and Steinmann, P. A finite element method for the computational modelling of cohesive cracks. *International Journal for Numerical Methods in Engineering*, 63:276–289, 2005.

[83] Meschke, G. and Dumstorff, P. Energy-based modeling of cohesive and cohesionless cracks via X-FEM. *Computer Methods in Applied Mechanics and Engineering*, 196:2338 –2357, 2007.

[84] Moës, N. and Belytschko, T. Extended finite element method for cohesive crack growth. *Engineering Fracture Mechanics*, 69:813–833, 2002.

[85] Moës, N., Dolbow, J., and Belytschko, T. A finite element method for crack growth without remeshing. *International Journal for Numerical Methods in Engineering*, 46:131–150, 1999.

[86] Mohammadi, S. *Extended Finite Element Method: for Fracture Analysis of Structures*. Wiley-Blackwel, 2008.

[87] Müller-Hoeppe, D., Wriggers, P., and Löhnert, S. Crack face contact for a hexahedral-based XFEM formulation. *Computational Mechanics*, 49:725–734, 2012.

[88] Nakaba, K., Kanakubo, T., Furuta, T., and Yoshizawa, H. Bond Behavior between Fiber-Reinforced Polymer Laminates and Concrete. *Aci Structural Journal*, 98:359–367, 2001.

[89] Needleman, A. An analysis of tensile decohesion along an interface. *Journal of the Mechanics and Physics of Solids*, 38:289–324, 1990.

[90] Ngo, D. and Scordelis, A. C. Finite Element Analysis of Reinforced Concrete Beams. *Journal Proceedings*, 64:152–163, 1967.

[91] Orlando, N. and Benvenuti, E. Advanced XFEM Simulation of Pull-out and Debonding of Steel Bars and FRP-Reinforcements in Concrete Beams. *American Journal of Engineering and Applied Sciences*, 9:746–754, 2016.

[92] Ortiz, M. and Suresh, S. Statistical Properties of Residual Stresses and Intergranular Fracture in Ceramic Materials. *Journal of Applied Mechanics*, 60:77–84, 1993.

[93] Osher, S. and Sethian, J. A. Fronts propagating with curvature-dependent speed: algorithms based on hamilton-jacobi formulations. *Journal of Computational Physics*, 79:12–49, 1988.

[94] Patzák, B. and Jirásek, M. Process zone resolution by extended finite elements. *Engineering Fracture Mechanics*, 70:957–977, 2003.

[95] Petersson, P.-E. *Crack growth and development of fracture zones in plain concrete and similar materials*. PhD thesis, Lund University, 1981.

[96] Pezeshki, M., Löhnert, S., Wriggers, P., Guidault, P. A., and Baranger, E. *3D Dynamic Crack Propagation by the Extended Finite Element Method and a Gradient-Enhanced Damage Model*. In *Multiscale Modeling of Heterogeneous Structures*. 2018, pages 277–299.

[97] Planas, J., Elices, M., and Guinea, G. V. Cohesive cracks versus nonlocal models: Closing the gap. *International Journal of Fracture*, 63:173–187, 1993.

[98] R. Khoei, A. *Extended Finite Element Method: Theory and Applications*. John Wiley & Sons, Ltd., 2015.

[99] Rabczuk, T. and Belytschko, T. Application of Particle Methods to Static Fracture of Reinforced Concrete Structures. *International Journal of Fracture*, 137:19–49, 2006.

[100] Radtke, F. K. F., Simone, A., and Sluys, L. J. A partition of unity finite element method for obtaining elastic properties of continua with embedded thin fibres. *International Journal for Numerical Methods in Engineering*, 84:708–732, 2010.

[101] Rahulkumar, P., Jagota, A., Bennison, S., and Saigal, S. Cohesive element modeling of viscoelastic fracture: application to peel testing of polymers. *International Journal of Solids and Structures*, 37:1873–1897, 2000.

[102] Rashid, Y. R. Ultimate strength analysis of prestressed concrete pressure vessels. *Nuclear Engineering and Design*, 7:334–344, 1968.

[103] Rehm, G. *Über die Grundlagen des Verbundes zwischen Stahl und Beton.* Deutscher Ausschuss für Stahlbeton, heft 138. Ernst, Berlin, 1961.

[104] Reinhardt, H. W., Cornelissen, H. A. W., and Hordijk, D. A. Tensile Tests and Failure Analysis of Concrete. *Journal of Structural Engineering*, 112:2462–2477, 1986.

[105] Remmers, J. J. C., de Borst, R., and Needleman, A. A cohesive segments method for the simulation of crack growth. *Computational Mechanics*, 31:69–77, 2003.

[106] Remmers, J. J., de Borst, R., and Needleman, A. The simulation of dynamic crack propagation using the cohesive segments method. *Journal of the Mechanics and Physics of Solids*, 56:70–92, 2008.

[107] Roth, S.-N., Léger, P., and Soulaïmani, A. A combined XFEM–damage mechanics approach for concrete crack propagation. *Computer Methods in Applied Mechanics and Engineering*, 283:923–955, 2015.

[108] Rots, J. G. *Computational modeling of concrete fracture.* PhD thesis, Delft University of Technology, 1988.

[109] Savoia, M., Ferracuti, B., and Mazzotti, C. *Non-linear bond-slip law for FRP concrete interface.* In *Fibre-Reinforced Polymer Reinforcement for Concrete Structures.* 2003, pages 163–172.

[110] Schellekens, J. C. J. and De Borst, R. On the numerical integration of interface elements. *International Journal for Numerical Methods in Engineering*, 36:43–66, 1993.

[111] Schober, H. *Ein Modell zur Berechnung des Verbundes und der Risse im Stahl- und Spannbeton.* PhD thesis, Universität Stuttgart, 1984.

[112] Sorelli, L. G., Meda, A., and Plizzari, G. A. Bending and Uniaxial Tensile Tests on Concrete Reinforced with Hybrid Steel Fibers. *Journal of Materials in Civil Engineering*, 17:519–527, 2005.

[113] Stolarska, M., Chopp, D. L., Moës, N., and Belytschko, T. Modelling crack growth by level sets in the extended finite element method. *International Journal for Numerical Methods in Engineering*, 51:943–960, 2001.

[114] Sukumar, N., Chopp, D. L., Moës, N., and Belytschko, T. Modeling holes and inclusions by level sets in the extended finite-element method. *Computer Methods in Applied Mechanics and Engineering*, 190:6183–6200, 2001.

[115] Sukumar, N., Dolbow, J. E., and Moës, N. Extended finite element method in computational fracture mechanics: a retrospective examination. *International Journal of Fracture*, 196:189–206, 2015.

[116] Sukumar, N., Huang, Z. Y., Prévost, J.-H., and Suo, Z. Partition of unity enrichment for bimaterial interface cracks. *International Journal for Numerical Methods in Engineering*, 59:1075–1102, 2004.

[117] Sukumar, N., Moës, N., Moran, B., and Belytschko, T. Extended finite element method for three-dimensional crack modelling. *International Journal for Numerical Methods in Engineering*, 48:1549–1570, 2000.

[118] Van den Bosch, M. J., Schreurs, P. J. G., and Geers, M. G. D. An improved description of the exponential Xu and Needleman cohesive zone law for mixed-mode decohesion. *Engineering Fracture Mechanics*, 73:1220–1234, 2006.

[119] Wang, J. Cohesive zone model of FRP-concrete interface debonding under mixed-mode loading. *International Journal of Solids and Structures*, 44:6551–6568, 2007.

[120] Wang, Y. and Waisman, H. Progressive delamination analysis of composite materials using XFEM and a discrete damage zone model. *Computational Mechanics*, 55:1–26, 2015.

[121] Wells, G. N., de Borst, R., and Sluys, L. J. A consistent geometrically non-linear approach for delamination. *International Journal for Numerical Methods in Engineering*, 54:1333–1355, 2002.

[122] Wells, G. N. and Sluys, L. J. A new method for modelling cohesive cracks using finite elements. *International Journal for Numerical Methods in Engineering*, 50:2667–2682, 2001.

[123] Wittmann, F. H., Rokugo, K., Brühwiler, E., Mihashi, H., and Simonin, P. Fracture energy and strain softening of concrete as determined by means of compact tension specimens. *Materials and Structures*, 21:21–32, 1988.

[124] Wu, H. Q., Gilbert, R. I., of New South Wales. School of Civil, U., and Engineering, E. *An Experimental Study of Tension Stiffening in Reinforced Concrete Tension Members Under Short-term and Long-term Service Loads*. University of New South Wales, 2008.

[125] Wu, J.-Y. and Li, F.-B. An improved stable XFEM (Is-XFEM) with a novel enrichment function for the computational modeling of cohesive cracks. *Computer Methods in Applied Mechanics and Engineering*, 295:77–107, 2015.

[126] Xu, X. P. and Needleman, A. Numerical simulations of fast crack growth in brittle solids. *Journal of the Mechanics and Physics of Solids*, 42:1397–1434, 1994.

[127] Xu, Y. and Yuan, H. Applications of normal stress dominated cohesive zone models for mixed-mode crack simulation based on extended finite element methods. *Engineering Fracture Mechanics*, 78:544–558, 2011.

[128] Yang, B., Mall, S., and Ravi-Chandar, K. A cohesive zone model for fatigue crack growth in quasibrittle materials. *International Journal of Solids and Structures*, 38:3927–3944, 2001.

[129] Zamani, A., Gracie, R., and Reza Eslami, M. Cohesive and non-cohesive fracture by higher-order enrichment of XFEM. *International Journal for Numerical Methods in Engineering*, 90:452–483, 2012.

[130] Zi, G. and Belytschko, T. New crack-tip elements for XFEM and applications to cohesive cracks. *International Journal for Numerical Methods in Engineering*, 57:2221–2240, 2003.

[131] Zi, G., Chen, H., Xu, J., and Belytschko, T. The Extended Finite Element Method for Dynamic Fractures. *Shock and Vibration*, 12:9–23, 2005.

[132] Zilch, K., Niedermeier, R., and Finckh, W. *Praxisgerechte Bemessungsansätze für das wirtschaftliche Verstärken von Betonbauteilen mit geklebter Bewehrung - Verbundtragfähigkeit unter statischer Belastung*. Deutscher Ausschuss für Stahlbeton, heft 592. Beuth, Berlin, 2012.